

Comparison of grain properties in
interplanetary dust from different types of
parent bodies by mid-infrared spectroscopic
observations with AKARI

高橋 葵

博士（理学）

総合研究大学院大学

物理科学研究科

宇宙科学専攻

平成30（2018）年度

学位論文

Comparison of grain properties in interplanetary dust
from different types of parent bodies
by mid-infrared spectroscopic observations with AKARI
「あかり」中間赤外線分光観測による
異なる母天体起源の惑星間塵の性質比較

Aoi Takahashi

高橋 葵

2019年3月22日 博士（理学）

Abstract

Interplanetary dust (IPD) is a population of dust particles distributing diffusely in the interplanetary space of the Solar System. The spatial distribution of the IPD is concentrated to the inner region within a few astronomical units (au) from the Sun, and the latitudinal profile has a peak at the ecliptic plane. One of the main constituent materials is silicate and the particle size has a range from a few tens of nanometer to millimeter order.

From dynamical simulations of orbital evolutions of the IPD particles, they are thought to be blown out of the Solar System or to accrete to the Sun owing to the interaction with the solar radiation and the lifetime is significantly shorter than the age of the Solar System. Therefore, they are thought not to have survived from the formation era in the Solar System, but to be continuously supplied from asteroids and comets. Asteroids repeat to collide with each other and break into fragments, reducing sizes of themselves. As the result of this collisional cascade, asteroids provide dust particles to the interplanetary space. Comets also eject dust particles into the interplanetary space owing to the sublimation of ice and spontaneous disruptions. Since such parent bodies are primordial planetesimals formed in the proto-solar disk, it means that the IPD particles have been incorporated into the parent body in the proto-solar disk, kept inside the body during the evolution of the Solar System, and recently returned to the interplanetary space again. Therefore, IPD particles are thought to suffer from the space weathering effect much less than the surface of their parent bodies and their grain properties can give us the information about the environment in the proto-solar system.

As a tracer of such properties, I focused on the spectral features around $10\ \mu\text{m}$ originating from Si-O vibration modes of silicates included in the IPD grains. The shape of the features depends on the grain properties such as mineral and chemical composition, crystallinity and crystal morphology, for examples. IPD particles scatter and absorb the sunlight in the ultraviolet–near-infrared wavelength region and the absorbed energy is re-emitted as the thermal emission in the mid-infrared wavelength region. It is the dominant diffuse source in the mid-infrared sky brightness, called the zodiacal emission. Past infrared space telescopes detected emission features in zodiacal emission spectra. However, such observations did not have high signal-to-noise ratio sufficient to identify properties of the IPD grains accurately. Moreover, differences in the grain properties of the IPD from different types of parent bodies were not discussed in these previous works, although the result in laboratory

measurements of the IPD particles collected near/on the Earth suggested that the asteroidal IPD and the cometary IPD have different grain properties.

The aim of this thesis is to compare the grain properties of the IPD from different types of parent bodies in terms of spectral features seen in the zodiacal emission. I compared the zodiacal emission spectra among various directions of the sky, because the IPD has different distributions in ecliptic latitudes depending on the types of the parent bodies. According to some dynamical simulations, the asteroidal IPD locally distributes at low specific ecliptic latitudes and observed as band structures near the ecliptic plane. On the other hand, because of the variety of comets inclinations, the cometary IPD distributes more globally than the asteroidal IPD does. Jupiter Family Comets (JFCs), which have an elliptical orbit with an inclination less than 30° and an aphelion around the Jupiter, can form the dust cloud with a broad distribution in ecliptic latitudes around the ecliptic plane. Oort Cloud Comets (OCCs), which come flying from the Oort cloud, have an isotropic distribution in inclinations and therefore, the IPD from the OCCs has an isotropic spatial distribution all over the sky. Although a substantial fraction of the total amount of the IPD is thought to be from the JFCs, it may be possible to detect any signs of the IPD from asteroids or the OCCs if observations cover the various ecliptic latitudes with a high sensitivity.

In this thesis, I analyzed mid-infrared spectroscopic data of the zodiacal emission at 74 different directions over the entire sky. The data was obtained with MIR-S channel of AKARI/IRC. This channel covers the wavelength range of 5–12 μm using two grisms. With a conventional reduction pipeline, the resultant spectra of two grisms were not smoothly connected owing to the inconsistency in the intensity level of their overlapping wavelength range. The cause of the inconsistency was three types of instrumental artifacts: the light scattered into pixels in the same row and column of a detector pixel array, the light scattered at the edge of a detector after going through a small window in the aperture mask, and the ghost of the small window aperture. I have empirically examined their brightness at each position on each image and subtracted them. As the result, I successfully obtained zodiacal emission spectra with high signal-to-noise ratio. Their intensity levels at 12 μm were found to be $\sim 10\%$ higher than those calculated by a zodiacal emission model based on observations of COBE/DIRBE (hereafter DIRBE zodi-model), while they were lower than those calculated by a similar model based on imaging observations using AKARI/IRC. Those inconsistencies may be caused by the inappropriate color correction factor used in the construction of both models.

I estimated a continuum spectrum at each direction of the sky on the basis of the DIRBE zodi-model. By dividing the zodiacal emission spectrum obtained at each direction by the corresponding continuum, I derived observed/continuum spectra at all 74 pointing directions. I detected excess

emission at 9–12 μm in all the observed/continuum spectra. They exhibit some sharp peaks significantly beyond the error range. Such detailed shapes have been revealed for the first time thanks to the high sensitivity of the IRC and the accurate subtractions of instrumental artifacts. I discussed the shapes of the emission features at all directions from a mineralogical point of view. First, I averaged the observed/continuum spectra in all observed directions and compared with absorption coefficients of candidate minerals. This enables us to understand grain properties typical for all over the sky. These typical properties represent the grain properties of the IPD from the JFCs, because the IPD from the JFCs (i.e., the smooth cloud) accounts for the significantly largest fraction of the total IPD. In the averaged spectra, I found main peaks around 9.60 and 10.65 μm caused by small grains of enstatite, and sub-peaks around 10.15 and 11.85 μm which are mainly contributed by small grains of forsterite, in addition to a composite peak from enstatite and forsterite at 11.30 μm . It indicates that the IPD from the JFCs includes small crystalline grains and is enstatite-rich. In order to reproduce the wavelength position of the enstatite peak shifted from 9.2 μm to 9.6 μm and the suppressed enstatite peak at 11.6 μm , enstatite grains included in the IPD from the JFCs may have extreme crystal morphologies like whisker- or platelet-shapes.

Secondly, I compared the feature shapes among different pointing directions, in order to compare grain properties among the IPD originating from different types of parent bodies. To investigate the influence of the asteroidal IPD on feature shapes, I compared feature shapes among directions with different brightness contribution levels of the asteroidal dust bands. The contribution was denoted by A and calculated on the basis of the IPD density distribution in the DIRBE zodi-model. On the other hand, the contribution of the IPD from the OCCs could not be calculated quantitatively because of the lack of an accurate model prediction of the density distribution including the isotropic component composed of the IPD from the OCCs. Instead, I compared feature shapes among directions with different absolute values of ecliptic latitudes, $|\beta_{\oplus}|$, in order to investigate the influence of the IPD from the OCCs. I averaged the observed/continuum spectra in A - or $|\beta_{\oplus}|$ - bins and compared the feature shapes.

As the most simple parameter of the feature shape, I calculated the equivalent width of the whole excess emission (EW_{whole}), which means the strength of excess above the continuum integrated in the 8–12 μm . EW_{whole} showed a clear positive correlation with $|\beta_{\oplus}|$. It indicates the increase in the fraction of small grains at the higher ecliptic latitudes, because absorption coefficients of small grains ($\sim 1 \mu\text{m}$) show more significant peaks than those of larger grains ($> 10 \mu\text{m}$). This result is consistent with previous works and can be explained by the collisional cascade during the accretion of IPD particles. On the other hand, a weak negative correlation between EW_{whole} and A was

found. It means that the size distribution of the asteroidal IPD is biased to relatively larger grains owing to grains in the middle of the collisional cascade from asteroids.

The high signal-to-noise ratio of AKARI spectra enabled us to investigate more detailed feature shape for the first time. I defined 3 parameters for the quantitative investigation: the equivalent width ratio in 10.0–10.5 μm and 9.0–9.5 μm ($EW_{10.0-10.5}/EW_{9.0-9.5}$), a wavelength shift of a peak excess due to crystalline silicates ($\Delta\lambda_{\text{peak}}$) and the equivalent width ratio of peak excess due to crystalline silicates ($EW_{\text{fo}}/EW_{\text{en}}$). $EW_{10.0-10.5}/EW_{9.0-9.5}$ and $EW_{\text{fo}}/EW_{\text{en}}$ were found to show a weak positive and negative correlation with A , respectively. A possible qualitative interpretation is the contribution of a smooth excess around 10 μm due to phyllosilicate minerals in the asteroidal IPD. Since phyllosilicate is a hydrated mineral, this implies the evidence of the aqueous alteration in the asteroidal IPD. From the negative $|\beta_{\oplus}|$ -dependence of $EW_{10.0-10.5}/EW_{9.0-9.5}$, the IPD from the OCCs was found to have a lower olivine/(olivine+pyroxene) ratio in amorphous grains than that of the IPD from the JFCs. In addition, the negative correlation between $|\beta_{\oplus}|$ and $\Delta\lambda_{\text{peak}}$ in the peak around 11.34 μm can be interpreted as evidence that the enstatite sub-peak at 11.1 μm is enhanced relative to the forsterite main peak around 11.25 μm at higher $|\beta_{\oplus}|$. This enhancement indicates a lower forsterite/(forsterite+enstatite) ratio of the IPD from the OCCs compared with that of the IPD from the JFCs. It was consistent with the result of the negative correlation of $EW_{\text{fo}}/EW_{\text{en}}$ with $|\beta_{\oplus}|$.

I assumed that the JFCs were formed only in an outer region like > 15 au in the proto-solar disk while the OCCs could be formed also in a more inner region like 4–15 au, as predicted by the Nice model. Since the grain properties of the IPD reflect the dust properties in the forming region of the parent bodies, obtained grain properties of the IPD from the JFCs show the dust properties in the outer region of the proto-solar disk. It means crystalline silicates were included in the dust particles in such cold region, although the interstellar dust is known as amorphous and silicate crystals can be formed only in a hot region like < 1 au from the Sun. This indicates any radial mixing process has occurred and annealed or re-condensed dust has been transported outward. Three hypotheses have been proposed to explain the radial mixing: turbulence mixing model, X-wind model, and the transportation by radiation pressure. I also found the differences of the mineral composition between the IPD from the JFCs and the OCCs, which imply the differences of the mineral composition among dust at different radial distances in the proto-solar disk. My findings may become useful to identify which radial mixing model is more reliable, if radial dependence of the mineral composition will be available in each model.

Contents

1	Introduction	6
1.1	Interplanetary dust	6
1.1.1	Orbital evolution and origins	6
1.1.2	Spatial distribution	9
1.1.3	Size distribution	11
1.2	Investigation of grain properties	13
1.2.1	Laboratory measurements of collected dust particles	14
1.2.2	Mineralogy in particles	15
1.2.3	Studies on zodiacal emission spectra	16
1.3	The organization of this thesis	19
2	Observation	20
2.1	AKARI satellite	20
2.2	Infrared Camera (IRC)	21
2.3	Spectroscopic observations of the zodiacal emission	21
3	Data reduction	27
3.1	Instrumental artifacts	27
3.1.1	The light scattered in detector pixels	27
3.1.2	The light scattered at the edge of a detector	29
3.1.3	The ghost of a small window aperture	31
3.2	Reduction flow	39
3.3	Obtained spectra	40
4	Grain properties	45
4.1	Detection of emission features	45

4.1.1	Continuum estimation based on a diluted blackbody function	45
4.1.2	Continuum estimation based on the DIRBE zodi-model	46
4.1.3	Comparison with previous works	47
4.2	Absorption coefficients of candidate minerals	48
4.3	Interpretation of the averaged observed/continuum spectrum	51
4.4	Variations due to the origin difference	54
4.4.1	Equivalent width of the whole excess emission : EW_{whole}	58
4.4.2	Equivalent width ratio in 10.0–10.5 μm and 9.0–9.5 μm : $EW_{10.0-10.5}/EW_{9.0-9.5}$	59
4.4.3	Wavelength shift of a peak excess due to crystalline silicates : $\Delta\lambda_{\text{peak}}$	62
4.4.4	Equivalent width ratio of peak excesses due to crystalline silicates : $EW_{\text{fo}}/EW_{\text{en}}$	63
4.5	Summary of the grain properties	65
5	Implications for the proto-solar system	69
5.1	Comet forming region	69
5.2	Dust mixing process	71
5.3	Future works	73
5.3.1	Quantitative evaluation of the mineral composition	73
5.3.2	Further observations	73
6	Conclusion	75

List of Figures

1.1	Dynamical evolution of the IPD supplied by the asteroid collision.	10
1.2	Density contour of each IPD components.	12
1.3	Secondary electron images in scanning electron microscopy of the IPD samples. . . .	15
1.4	Examples of extreme crystal morphologies found in the enstatite grains included in the collected IPD.	16
1.5	Transmission electron micrographs of GEMS within the collected IPD.	17
2.1	Bird's-eye view of the IRC.	22
2.2	Schematic view of an aperture on the telescope focal plane and the corresponding detector sensitive area in the NIR or MIR-S channel.	23
2.3	Map of the pointing directions I observed.	24
3.1	Schematic view of artificial components.	28
3.2	Brightness profile of the light scattered in detector pixels.	30
3.3	Example of the datasets used for the estimation of the brightness profile of the light scattered at the detector edge.	31
3.4	Brightness profile of the light scattered at the edge of a detector.	32
3.5	Two-dimensional images before and after subtractions of the scattered lights.	33
3.6	Example of the datasets indicating the clear ghost of a small window aperture. . . .	35
3.7	The schematic drawing of steps to estimate the brightness profile of the ghost. . . .	36
3.8	Brightness profile of the ghost of the small window aperture.	37
3.9	Brightness profiles in the slit-spectroscopic region before and after the subtractions of artifacts.	38
3.10	The data-reduction flow I performed.	40
3.11	The response curve used in this work.	41

3.12 Spectra obtained with the SG1 and the SG2 before and after the subtraction of three types of artifacts.	42
3.13 The correlation of the 12 μm intensity between spectra obtained in this work and prediction by the DIRBE zodi-model.	44
3.14 The correlation of the 9 μm intensity between spectra obtained in this work and prediction by the IRC zodi-model.	44
4.1 Best-fit parameters for continuum fitting by a diluted blackbody function.	46
4.2 Comparison of the observed/continuum spectrum with IRTS/MIRS observations. . .	48
4.3 Comparison with the absorption coefficients of candidate minerals.	50
4.4 The wavelength shift in a peak around 9.2 μm	53
4.5 Dielectric function of orthorhombic-enstatite.	54
4.6 The two-dimensional histogram of the brightness contribution from the dust bands and absolute values of ecliptic latitudes at the pointing directions.	56
4.7 The observed/continuum spectra averaged in each A -bin.	57
4.8 The observed/continuum spectra averaged in each $ \beta_{\oplus} $ -bin.	57
4.9 The dependence of the equivalent width of the whole excess emission on the brightness contribution from the dust bands and the ecliptic latitude.	59
4.10 Relation between the equivalent width of the whole excess emission and the grain size.	60
4.11 The dependence of the equivalent width ratio in 10.0–10.5 μm and 9.0–9.5 μm on the brightness contribution from the dust bands and the ecliptic latitude.	61
4.12 The histogram of peak wavelengths.	63
4.13 The dependence of a wavelength shift of a peak excess due to crystalline silicates on the brightness contribution from the dust bands and the ecliptic latitude.	64
4.14 The dependence of the equivalent width ratio of peak excesses due to crystalline silicates on the brightness contribution from the dust bands and the ecliptic latitude.	66
6.1 Relation between the brightness of the ghost component and the median value of the brightness at the center of the main field of view for the SG1.	99
6.2 Relation between the excess of the c value above the linear relationship and the mid-infrared brightness of the ULIRG in the small window aperture.	100

List of Tables

1.1	Names of main types of crystalline silicate.	16
2.1	Log for the 74 pointing observations.	24
4.1	The slopes of the linear functions of A or $ \beta_{\oplus} $ that best fit EW_{whole} , $EW_{10.0-10.5}/EW_{9.0-9.5}$, $\Delta\lambda_{\text{peak}}$, and $EW_{\text{fo}}/EW_{\text{en}}$	68

Chapter 1

Introduction

1.1 Interplanetary dust

In the interplanetary space of the Solar system, dust distributes diffusely and we call it interplanetary dust (IPD). The particle size of the IPD has a range from a few tens of nanometer to millimeter order (see section 1.1.3 for details). It distributes mainly at the ecliptic plane in a few astronomical units (au) from the Sun (see section 1.1.2 for details) and, therefore, the Earth exists inside the dust cloud. It means that some of these dust particles accrete to the Earth and can be collected in the stratosphere or on the ground. In addition, the IPD scatters and absorbs the sunlight in the ultraviolet–near-infrared wavelength region. While the scattered light can be seen as the zodiacal light in such wavelength region, the absorbed energy is re-emitted as the thermal emission in the mid-infrared wavelength region, which is called the zodiacal emission. We can observe the zodiacal light and emission as the dominant diffuse source in almost all over the sky, except the galactic plane, where the radiation from the interstellar dust becomes a main contributor to the sky brightness.

In this chapter, I will present the summary of the previous studies on the IPD based on laboratory measurements of collected dust particles, in-situ measurements using space probes, and remote observations of the zodiacal light and the zodiacal emission.

1.1.1 Orbital evolution and origins

Basically, the IPD particles have a Keplerian orbit with the gravitational attraction to the Sun in the motion equation of

$$\mathbf{F}_{\text{grav}} = -\frac{GM_{\odot}m}{r^2}\hat{\mathbf{r}}, \quad (1.1)$$

where G is the gravitational constant, M_\odot is the solar mass, m is the mass of a particle, and r is the distance from the Sun. However, some other forces disturb the orbit. The particles dynamically interact with the solar radiation and exchange the momentum during absorption, scattering and re-emission of the incident photons. It results in a disturbance of the particle orbits due to the radiation force. As seen from the frame fixed to a particle with a geometrical cross section of A , the radiation force can be written by the following (Burns et al. 1979; Gustafson 1994; Klacka 1992):

$$\mathbf{F}_{\text{rad}} = \frac{S_0 A Q_{\text{pr}}}{r^2 c} \left[\left(1 - \frac{2}{c} \frac{dr}{dt} \right) \hat{\mathbf{r}} - \left(\frac{r}{c} \frac{d\theta}{dt} \right) \hat{\boldsymbol{\theta}} \right], \quad (1.2)$$

where c is the speed of light, S_0 means the flux density of the solar radiation at 1 au, and Q_{pr} is an efficiency factor for radiation forces defined by $Q_{\text{pr}} \equiv Q_{\text{abs}} + Q_{\text{sca}} \langle \cos \alpha \rangle$ using a scattering angle, α . Q_{abs} and Q_{sca} are efficiency factors for absorption and scattering by the particle, respectively, and $\langle \cos \alpha \rangle$ accounts for asymmetry of the scattered radiation. $\hat{\mathbf{r}}$ and $\hat{\boldsymbol{\theta}}$ are unit vectors in the radial and tangential direction of the particle orbit, respectively. Since θ represents the rotation angle, $d\theta/dt$ indicates the particle angular velocity. Force written by the velocity-independent radial term is called radiation pressure and it points particles radially away from the Sun. Force written by the velocity-dependent tangential term is called Poynting-Robertson (PR) drag. Particles receiving the effective PR drag lose their angular momentum and gradually reduce their orbital radius.

Orbital evolution of the IPD particles is determined by the ratio of $F_{\text{rad}}/F_{\text{grav}}$. The ratio is often represented by β and approximated as

$$\beta \equiv \frac{|F_{\text{rad}}|}{|F_{\text{grav}}|} \sim \frac{(S_0/r^2 c)}{GM_\odot/r^2} \times Q_{\text{pr}} \times \frac{A}{m} = C_r Q_{\text{pr}} \frac{A}{m}, \quad (1.3)$$

where $C_r = 7.6 \times 10^{-5} \text{ g cm}^{-2}$ (Burns et al. 1979; Gustafson 1994; Wyatt et al. 1999). Since A has the dimension of area and m is proportional to the volume of a particle, A/m is inversely proportional to the radius of a particle, a . Therefore, $\beta \propto a^{-1}$ for large particles, in which Q_{pr} does not depend on a . In the limit of small particles ($a \ll 1$), where Rayleigh scattering can be assumed, Q_{sca} decreases more drastically than Q_{abs} because $Q_{\text{sca}} \propto a^4$ and $Q_{\text{abs}} \propto a$. Then we can think $Q_{\text{pr}} \sim Q_{\text{abs}} \propto a$ and β is size-independent. According to calculations of β for homogeneous sphere particles with various sizes and materials using Mie theory (Bohren & Huffman 1983; Kerker 1969), β has a peak at $a \sim 0.1 \mu\text{m}$ and decrease with $\beta \propto a^{-1}$ at the larger side of the peak (Gustafson 1994; Mukai et al. 1992).

If $\beta > 0.5$, a particle is blown out along a hyperbolic orbit owing to the solar radiation pressure and it is called “ β -meteoroids.” Assuming the size-dependence of β , small particles with $a \sim 0.1 \mu\text{m}$

can be blown out of the Solar System. Much smaller particles are also difficult to keep existing in the Solar System owing to pressure caused by collisions with solar wind particles and the Lorentz force, which is the interaction between charged particles and electromagnetic fields in the interplanetary space (Gustafson 1994; Mukai & Giese 1984). On the other hand, particles larger than $0.1 \mu\text{m}$, which satisfy $\beta < 0.5$, are affected by PR drag and gradually accrete to the sun following a spiral orbit as the result of the momentum loss (Wyatt et al. 1999). After they approach the Sun, they evaporate and vanish. The lifetime of such particles is calculated by

$$t_{\text{PR}} \sim \frac{400 r^2}{\beta} \quad [\text{year}] , \quad (1.4)$$

where r means the original distance from the Sun in au. It corresponds to 10^5 – 10^6 years, assuming a typical size and spatial distribution of the IPD (Burns et al. 1979; Wyatt et al. 1999). This time scale is significantly shorter than the age of the Solar System, $\sim 4.5 \times 10^9$ years. Therefore, the IPD is thought not to be survived particles from the planetary formation era, but to be supplied recently.

If we suppose the bounds of large objects, β becomes infinitesimal and t_{PR} becomes sufficiently long, i.e., radiation forces do not affect. Instead, they collide with each other and break into fragments smaller than themselves. Their typical lifetimes are determined by the time scale of this collisional cascade, $t_{\text{coll}} \sim 10^9 \sqrt{a}$ (Wyatt et al. 1999). If objects have the size of ~ 20 km, their lifetimes become similar to the age of the Solar System. It implies that asteroids larger than ~ 20 km should be primordial asteroids. Collisional cascade from such asteroids can continuously supply the IPD even today. This is thought to be one of the main sources of the IPD.

Another possible source of the IPD is the sublimation and/or spontaneous disruptions of comets. Comets are also survived planetesimals as well as asteroids. Comets sublimate near their perihelion (\leq a few au) and eject the dust particles that have been buried in the icy mantle. The size distribution of ejected particles is investigated by observations of cometary dust coma and found that it has a peak around sub-micron (Hanner 1983; Shinnaka et al. 2018). Although most of such small particles may be blown out owing to the solar radiation pressure, larger particles can make a dust trail as observed (Davies et al. 1984; Ishiguro et al. 2002) and gradually accrete to the Sun owing to the PR drag. Nesvorný et al. (2010) said more than 90% of the zodiacal emission flux originate from the cometary IPD on the basis of imaging observations with a space-borne infrared telescope, IRAS, and dynamical simulations of supplied particles.

1.1.2 Spatial distribution

According to some dynamical simulations, the IPD originating from different types of parent bodies has different spatial distributions.

The asteroidal IPD distributes in local band structures at specific ecliptic latitudes same as their parent asteroid families. Sykes & Greenberg (1986) simulated the dynamical evolutions of the asteroidal IPD after the release from asteroids. Just after it is released near the main belt at a few au, the IPD particles follow the orbit of the parent bodies, as seen in the first phase of Figure 1.1. The orbits experience differential precession caused by gravitational perturbations from the Jupiter and the longitudes of nodes are gradually dispersed (see the middle phase of Figure 1.1). In the time scale of 10^5 to 10^6 years, the nodes have been distributed uniformly in all ecliptic longitudes, like the last phase of Figure 1.1. These processes result in a pair of dust distribution peaks with ring structures which are symmetrical across the ecliptic plane. As they are spiraling into the Sun owing to the PR drag, they are seen as a pair of dust bands approaching to us if we observe them from the Earth. Imaging observations performed by past infrared space telescopes found such structures near the ecliptic plane (Ootsubo et al. 2016; Low et al. 1984). For some of them, the parent asteroid family has already been identified (Nesvorný et al. 2003). For example, a pair of dust bands at the ecliptic latitudes of $\pm 9^\circ.3$ originates from the collision at 8.3 Myr ago in Veritas asteroid family at 3.17 au, which is mainly composed of C-type asteroids. A band pair seen in $\pm 2^\circ.1$ is thought to be formed 5.75 Myr ago through the collisional disruption in Koronis asteroid family at 2.87 au, whose main bodies are S-type asteroids.

On the other hand, because of the variety of comets inclinations, the IPD from comets distribute more globally than that from asteroids. Comets are divided into some groups depending on their orbit. One group is called Jupiter Family Comets (JFCs). They have an elliptical orbit with an inclination less than 30° and an aphelion distance close to the mean distance of the Jupiter from the Sun (Dones et al. 2015). Another group is Oort Cloud Comets (OCCs), which come flying from the Oort cloud at 10^4 – 10^5 au along the orbit with an isotropic distribution of inclinations. The JFCs can form the dust cloud with a broad distribution of ecliptic latitudes around the ecliptic plane and it extends even to the ecliptic poles (Nesvorný et al. 2010; Liou et al. 1995), while the IPD from the OCCs has an isotropic distribution all over the sky (Poppe 2016).

Kelsall et al. (1998) modeled the spatial distribution of the zodiacal emission brightness on the basis of the data obtained with COBE/DIRBE. In the model, they assumed three types of IPD components: smooth cloud, dust bands, and circumsolar ring with trailing blob. Figure 1.2 shows the density contour of each component. The smooth cloud is a mass of the IPD distributing globally

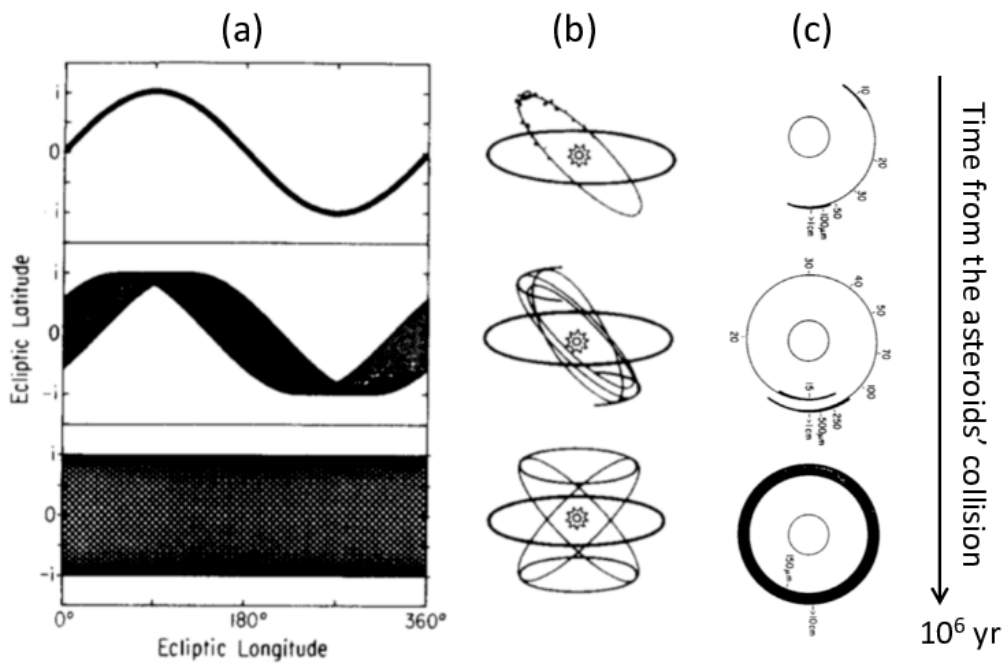


Figure 1.1: Dynamical evolution of the IPD supplied by the asteroid collision (Sykes & Greenberg 1986): (a) distribution observed from the Earth in a geocentric ecliptic latitude, (b) bird's-eye view of the orbit of the IPD particles, and (c) the IPD orbit seen from a ecliptic pole.

within a few au from the Sun. In combination with the result of the dynamical simulations of the ejected IPD, more than 90% of this component is the IPD from the JFCs (Nesvorný et al. 2010). Dust band structures are composed of the asteroidal IPD and this model included three dust bands at the ecliptic latitudes of $\pm 1^\circ.4$, $\pm 10^\circ$ and $\pm 15^\circ$, which recently have been formed by the Themis & Koronis families, the Veritas & Eos family and the Maria & Io family, respectively. The circumsolar ring is a component of the IPD trapped by the Earth gravity into a resonant orbit near 1 au during the accretion to the Sun (Jackson & Zook 1989). The asteroidal IPD can be trapped more easily than the cometary IPD because of the low-eccentricity orbits (Marzari & Vanzani 1994). In addition to the ring structure, the IPD trapped in mean motion resonances with the Earth follows behind the Earth along the same orbit. It was considered as a trailing blob in the model. They estimated the spatial distribution of the cross section for each component in conjunction with the spatial distribution of the particle temperature.

Kondo et al. (2016) presented a modified model based on the data from all sky imaging survey using AKARI/IRC (hereafter IRC zodi-model). They assumed basically the same IPD components described by the same functions of density distributions as the DIRBE zodi-model. However, this model additionally considered the component which has an isotropic distribution (i.e., mainly the IPD from the OCCs) for the first time.

Commonly in the result of both models, the smooth cloud component formed with the IPD from the JFCs accounts for the largest percentage of the total amount of the IPD, although the resultant absolute value of the density distribution was larger in the IRC zodi-model than that of the DIRBE zodi-model (Kondo et al. 2016). The fraction of the asteroidal IPD becomes relatively large in lines of sight toward the asteroidal dust bands. Since the amount of the IPD from the JFCs becomes smaller as going apart from the ecliptic plane in spite of the constant amount of the IPD from the OCCs all over the sky, the fraction of the IPD from the OCCs may become relatively larger at higher ecliptic latitudes.

1.1.3 Size distribution

The size distribution of the IPD was revealed by some types of measurements and observations: measurements of lunar craters, radar observations of meteors, imaging observations of the zodiacal light and in-situ measurements of dust mass flux using space probes.

The first model, called “the lunar flux model,” has been constructed from the lunar crater size distribution of Morrison & Clanton (1979) with the absolute flux calibration from the Pegasus satellite experiment (Naumann 1966).

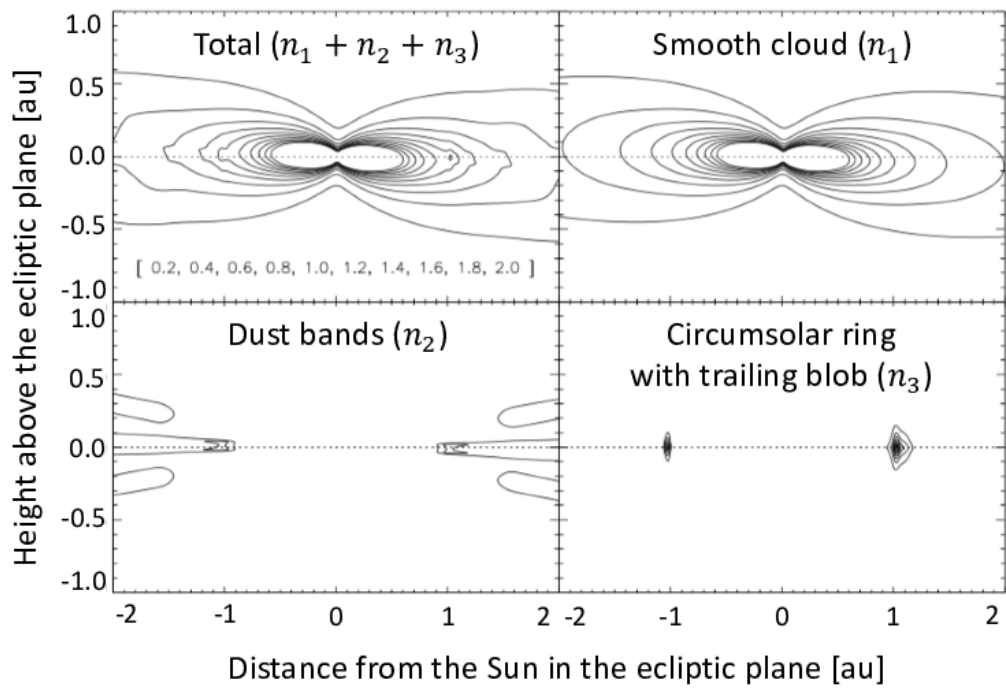


Figure 1.2: Density contour of each IPD components: smooth cloud, dust bands, and circumsolar ring with trailing blob (Kelsall et al. 1998).

Grün et al. (1985) re-evaluated it to explain the results of in-situ flux measurements using the HEOS-2 satellite and a quantitative analysis of collisional effects for β -meteoroids. This model is called “the interplanetary flux model.” The interplanetary flux model deviates from the lunar flux model only for small particles ($m \simeq 10^{-9}$ g, corresponding to $d \simeq 10 \mu\text{m}$ in diameter if the density is 2.5 g/cm^3). The modeled function of the size distribution is expressed by a smoothly broken power-law with negative indices and covers the size range from $0.01 \mu\text{m}$ to 1 cm assuming the density of 2.5 g/cm^3 . It fits accurately the mass fluxes measured at 1 au .

A much more extended flux model was developed by Divine (1993) totally including the result of many types of measurements in $0.1\text{--}20 \text{ au}$. Jehn (2000) used the data and considered the dependence of the size distribution on the distance from the Sun. They found that the size distribution at a few au was more biased to large particles than that at other distances, which is expected to be due to the asteroidal IPD recently supplied in the main belt.

It is also known that the fraction of small particles becomes greater as decreasing the radial distance. This can be caused by the collisional cascade during the accretion of the IPD particles due to the PR drag (Grün et al. 1985). Renard et al. (1995) found that albedo of the IPD decrease as the radial distance becomes far away from the Sun, in proportion to $R^{-0.32}$. Since small particles have lower absorption coefficients (i.e., higher albedo) in optical wavelength, this is supportive of the enhanced fraction of small particles in the inner region.

1.2 Investigation of grain properties

As shown in 1.1.1, the IPD originates from asteroids and comets. Those parent bodies are primordial planetesimals formed in the proto-solar disk. It means that the parent bodies may include information about the environment in the proto-solar system. However, surfaces of asteroids are well affected by two types of space weathering effect (Vernazza et al. 2009; Noguchi et al. 2011): that by micrometeoroid bombardment with the time scale of $10^8\text{--}10^9$ years (Schramm et al. 1989) and that by the solar wind irradiation with the time scale of $10^4\text{--}10^6$ years (Strazzulla et al. 2005). In addition, the opportunity for observations of cometary sublimation is very limited.

On the other hand, after an IPD particle was incorporated into the parent body in the proto-solar disk, it has been kept inside the body during the evolution of the Solar System without any significant metamorphosis, except for local aqueous alteration inside the asteroids (Germani et al. 1990). Once it has been recently returned back to the interplanetary space, the lifetime ($10^5\text{--}10^6$ years, see section 1.1.1) is relatively short to be affected by space weathering compared with the

surface of the parent bodies. It means that the grain properties of the IPD currently existing, such as the mineral or chemical composition, crystallinity, and crystal morphology, represents the grain properties of dust in the forming region of the parent planetesimals and can help us to understand the environment in the proto-solar system. Therefore, the investigation of the IPD grain properties is important for the study on the formation process of planetary systems.

1.2.1 Laboratory measurements of collected dust particles

According to an examination of hyper-velocity impact craters on the space-facing end of the Long Duration Exposure Facility satellite (Love & Brownlee 1993), the IPD particles close to 1 au are accreting to the Earth with the rate of $\sim 4.0 \times 10^7$ kg per year for particles smaller than $300 \mu\text{m}$ in diameter. Some of such accreting particles have been collected in clean locations on the ground (the polar site, for example), in the stratosphere, and by instruments on the international space station or satellites in low-Earth orbit. In some cases, their parent bodies can be estimated by the direction from which the particle come flying.

Properties of the collected samples have been measured in laboratories. Figure 1.3 shows the scanning electron microscopy images of the samples of the cometary IPD and the asteroidal IPD. The cometary IPD looks like a chondritic-porous (CP) and fluffy particle. Studies using transmission electron microscope (Messenger et al. 2013) revealed that the CP dust is anhydrous and consists of sub- μm grains of Mg-rich crystalline silicates, Fe-Ni sulfides, and amorphous silicates bound together by abundant carbonaceous materials. Keller & Messenger (2005) says crystalline silicates in CP dust are dominated by enstatite (MgSiO_3) and forsterite (Mg_2SiO_4), with minor fractions of diopside ($\text{MgCaSi}_2\text{O}_6$) and anorthite ($\text{CaAl}_2\text{Si}_2\text{O}_8$). Single crystals are typically included as grains with the size of 0.1–a few μm , while 0.1–2.0 μm sized polycrystalline silicate grains composed of 50–200 μm sized crystals are also common. Many enstatite grains exhibit extreme crystal morphologies such as whisker- and platelet-shape, as shown in Figure 1.4. According to Bradley et al. (1983), such morphologies can be caused by growth defects of the crystal lattice structure, which indicates they have condensed directly from vapor phase in non-equilibrium. Glass with embedded metal and sulfides (GEMS; Bradley et al. 1999), which is mainly composed of amorphous silicate as shown in Figure 1.5, also have commonly found in the collected IPD seemed to be cometary.

On the other hand, samples of the asteroidal IPD are known as chondritic-smooth (CS) and compact particles (i.e., low porosity; see Figure 1.3) and mainly composed of hydrated silicates and carbon. Germani et al. (1990) and Schramm et al. (1989) reported they show compositional heterogeneities and include aqueous alteration products only at localized part.

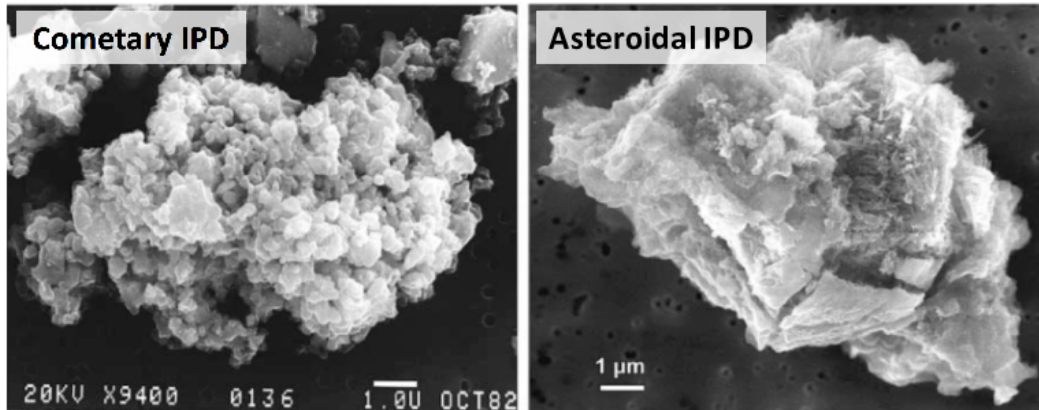


Figure 1.3: Secondary electron images in scanning electron microscopy of the IPD samples (Bradley 2003). Left: chondritic-porous (CP) dust frequently found in the cometary IPD. Right: chondritic-smooth (CS) dust frequently found in the asteroidal IPD.

Thus, grain properties were found to be quietly different between samples of the asteroidal IPD and the cometary IPD. It is necessary to distinguish grain properties between the IPD from different types of parent bodies.

1.2.2 Mineralogy in particles

As described in section 1.2.1, the IPD particles consist of some types of silicate minerals. Silicate means an assembly of tetrahedron structure of SiO_4 (i.e., an oxygen atom surrounded by 4 silicon atoms). Silicate in which tetrahedra do not share any atoms (i.e., isolated silicate) is called olivine, and silicate composed of tetrahedra sharing one oxygen with each other (i.e., chain silicate) is named pyroxene. The tetrahedra are arranged periodically in crystalline silicates, although amorphous silicates include random arrangement of the tetrahedra.

Silicate is one of solid solutions, which means metal ions get in between the SiO_4 tetrahedra or sometimes replace the silicon ions keeping the balance of electric charge. Assuming the solar composition (Lodders 2003), magnesium and iron ions can mainly occupy the site between the SiO_4 tetrahedra. Particularly, crystalline silicates included in the IPD seem to be Mg-rich according to the laboratory measurement of the collected IPD (see section 1.2.1).

Mg-Fe olivine and pyroxene are expressed by chemical formula: $\text{Mg}_{2x}\text{Fe}_{2(1-x)}\text{SiO}_4$ and $\text{Mg}_x\text{Fe}_{1-x}\text{SiO}_3$ ($0 \leq x \leq 1$), respectively. Crystalline silicate has a name depending on the molecular structure and the metal composition (x). I summarized such mineral names in Table 1.1.

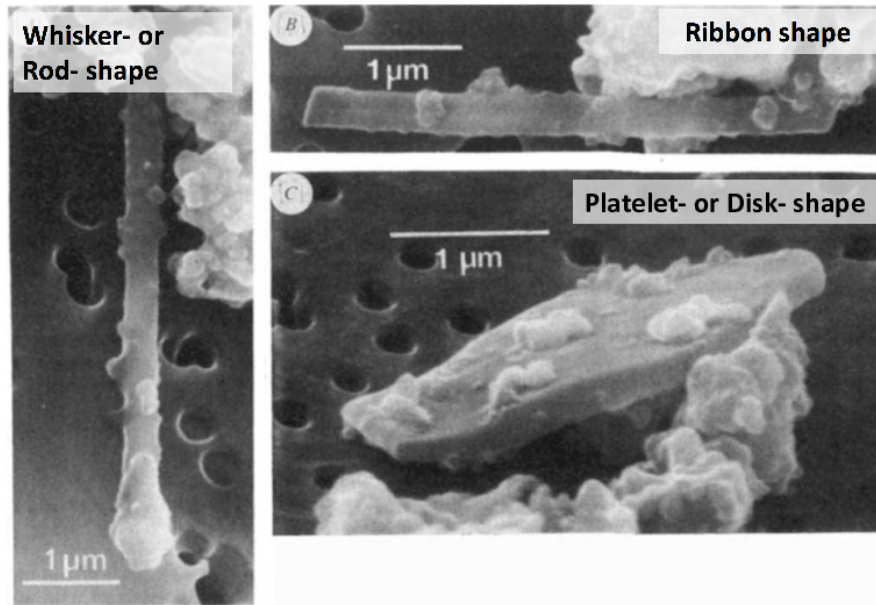


Figure 1.4: Examples of extreme crystal morphologies found in the enstatite grains included in the collected IPD (Bradley et al. 1983).

I have to note that there are several enstatite polymorphs: ortho-, proto-, and clino-enstatite. They have different stacking structure of layer of tetrahedra chains. According to the calculation in Choudhury & Chaplot (2000), ortho-enstatite is the most stable at ambient conditions, although it transforms to the proto-enstatite at high temperatures. Clino-enstatite can be stable at high pressures and experiments presents the existence of clino-enstatite also at low temperatures even at low pressures (Gasparik 1990).

Table 1.1: Names of main types of crystalline silicate.

	Mg-end ($x = 1$)	Fe-end ($x = 0$)
Olivine ($\text{Mg}_{2x}\text{Fe}_{2(1-x)}\text{SiO}_4$)	Forsterite	Fayalite
Pyroxene ($\text{Mg}_x\text{Fe}_{1-x}\text{SiO}_3$)	Enstatite	Ferrosilite

1.2.3 Studies on zodiacal emission spectra

Silicates have vibration modes between their constituent atoms, in the energy range corresponding to the mid-infrared wavelength region. For example, they have some stretching modes between Si-O atoms around $10 \mu\text{m}$, while some bending modes between O-Si-O atoms are exist around $20 \mu\text{m}$. Each vibration mode causes a spectral peak in the absorption coefficient at the corresponding

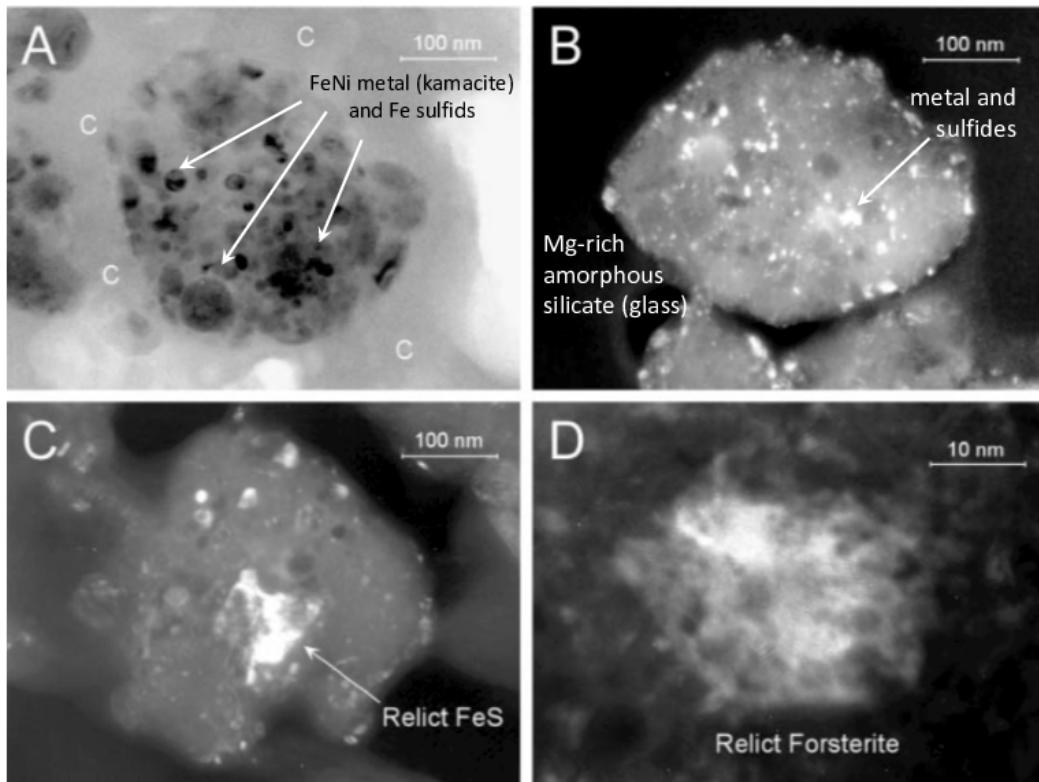


Figure 1.5: Transmission electron micrographs of GEMS within the collected IPD (Bradley et al. 1999). (A) Bright-field image of GEMS embedded in amorphous carbonaceous material (labeled “C”). Inclusions seen as black regions are FeNi metal (kamacite) and FeS. (B) Dark-field image of GEMS. The main constituent seen as the uniform gray region is Mg-rich amorphous silicate (glass), and it includes the grains of metal and sulfides. (C) Dark-field image to show the FeS inclusions. (D) Dark-field image to show the forsterite inclusions.

wavelength and it results in spectral features seen in the zodiacal emission.

Since the grain properties like mineral and metal composition or crystal morphology affect the vibration modes, the resultant feature shape depends on such properties. It means that we can trace the grain properties of the IPD from the shape of spectral features. Therefore, spectroscopic observations of the zodiacal emission is another effective approach to investigate the grain properties of the IPD. This approach has an advantage of comprehensive investigations into the properties of all the IPD grains included in the line of sight without any sample bias, compared with the laboratory measurements of the collected IPD samples which is biased to the particles easy to reach to the Earth.

In this thesis, I focused on the features around $10\ \mu\text{m}$ in the zodiacal emission. According to the previous spectroscopic observations of the zodiacal emission, some spectral features are detected as excess emission. Mid-infrared camera on board the Infrared Space Observatory (ISOCAM) measured the sky spectra over the wavelength range of $5\text{--}16\ \mu\text{m}$ and reported excess emission in the $9\text{--}11\ \mu\text{m}$ range with the amplitude of 6% of the continuum (Reach et al. 1996, 2003), although Leinert et al. (2002) concluded zodiacal emission spectra obtained with the spectrophotometric sub-instrument of ISO photometer, ISOPHOT, are smooth and featureless. Mid-infrared Spectrometer (MIRS) on board the Infrared Telescope in Space (IRTS), the first Japanese infrared space telescope, obtained the zodiacal emission spectra in $4.5\text{--}11.7\ \mu\text{m}$ and the $9\text{--}12\ \mu\text{m}$ excess was seen, although the conclusion depends on the spectral range where the continuum fitting is attempted (Ootsubo et al. 1998).

Such observations, however, did not have high signal-to-noise ratio sufficient to identify detailed properties of the IPD grains. In addition, grain properties of the IPD from different types of parent bodies were not separately discussed in those previous works, although the result in laboratory measurements of the collected IPD suggested that the grain properties depend on the types of the parent bodies, as described in section 1.2.1.

In order to compare the grain properties of the IPD from different types of parent bodies, therefore, I compared the shape of features in the zodiacal emission spectra among different directions of the sky, because the IPD has a different spatial distribution depending on the types of the parent bodies as shown in section 1.1.2.

1.3 The organization of this thesis

In this thesis, I derived the zodiacal emission spectra at 74 pointing directions and carefully compared the shape of emission features among different directions for the first time. In the following two chapters, I will explain about the observational data obtained by AKARI/IRC and the reduction process. I will show the results of the feature shape and discuss the grain properties of the IPD originating from various types of parent bodies in chapter 4. In chapter 5, I will describe the implications for the environment in the proto-solar system and future works.

Chapter 2

Observation

2.1 AKARI satellite

AKARI (Murakami et al. 2007) is a Japanese infrared astronomy satellite. It was launched by a M-V rocket in February 2006, and the science operation has finished in May 2011. The satellite loaded a telescope with the effective aperture diameter of 68.5 cm and two focal plane instruments, the Infrared Camera (IRC; Onaka et al. 2007) and the Far-Infrared Surveyor (FIS; Kawada et al. 2007). These instruments cover the wavelength range of 2–27 μm and 50–180 μm , respectively. In infrared observations from space, thermal radiation from the optical system itself becomes a dominant source of the background noise. Therefore, the total optical system was cooled down to 5.8 K by a pair of two-stage Stirling cycle mechanical coolers as well as liquid helium.

AKARI satellite was brought into a circular Sun-synchronous polar orbit at an altitude of ~ 700 km and an inclination of $98^\circ.2$. It was flying along the day-night border with the orbital period of ~ 100 min. This orbit enables us to observe the all sky region in a half year, although its solar elongation angle was limited to $90^\circ \pm 1^\circ$.

After a performance-verification phase on orbit, all sky imaging survey was performed for a half year (Phase 1) and pointing observations were carried out in combination with the observations for supplement of the all-sky survey (Phase 2). Phase 2 continued for ten months until the liquid helium has been boiled off in August 2007. Only near-infrared (2–5 μm) observations were performed also in the following phase, in which the temperature of the telescope was kept at ~ 40 K by using the mechanical coolers (Phase 3).

2.2 Infrared Camera (IRC)

AKARI/IRC consists of three channels with different wavelength coverage: the NIR channel for 2–5 μm , the MIR-S channel for 5–13 μm , and the MIR-L channel for 12–27 μm (although spectroscopy was limited to the region longer than 17.5 μm in actual use, owing to an instrumental trouble). A bird’s-eye view of the IRC is shown in Figure 2.1.

Each channel has three band filters and two dispersion elements: one prism and one grism in the NIR channel, two gratings in each of the MIR-S and MIR-L channels, although one of gratings in the MIR-L channel is out of work. They are installed on a filter wheel along with a blank window as a shutter, which is necessary for the subtraction of dark currents. By rotating the filter wheel, we can switch from imaging to spectroscopy, or change the wavelength coverage.

All three channels were operated simultaneously. The NIR and MIR-S channels share the same field of view using a beam splitter, although the MIR-L channel looked a different sky region at 25' away from that of the NIR/MIR-S channel. On the telescope focal plane, an aperture mask with two main apertures (approximately 10' \times 10' for each) is set. One of the main apertures fixes the main field of view common to the NIR and MIR-S channel, and the other determines that of the MIR-L channel. Both main apertures are accompanied by a slit aperture in their neighbor, and therefore, all three channels have a capability for spectroscopic observations of diffuse sources, like the zodiacal emission and extended nearby galaxies. One small window aperture is also equipped next to the slit aperture common to the NIR and MIR-S channel, for spectroscopic observations of point sources in the NIR channel. The upper panel of Figure 2.2 shows a schematic view of the aperture common to the NIR and MIR-S channel.

A Si:As detector with 256 \times 256 pixels is installed in the MIR-S channel. I should note that the detector sensitive area is designed to be smaller than that of the NIR channel. Moreover, the detector position in the MIR-S channel was found to be slightly shifted and tilted. Therefore, the detector image of the MIR-S channel can not cover the entire field of view of the aperture, as shown in the bottom panel of Figure 2.2.

2.3 Spectroscopic observations of the zodiacal emission

AKARI/IRC accomplished near- and mid-infrared spectroscopic observations of the zodiacal emission during the Phase 2 (November 2006–August 2007), as part of the mission program “SOSOS.” Taking advantage of the AKARI orbit, the zodiacal emission was observed at 74 pointing directions. I summarized the log for the observations in Table 2.1. Figure 2.3 indicates the map of the observed

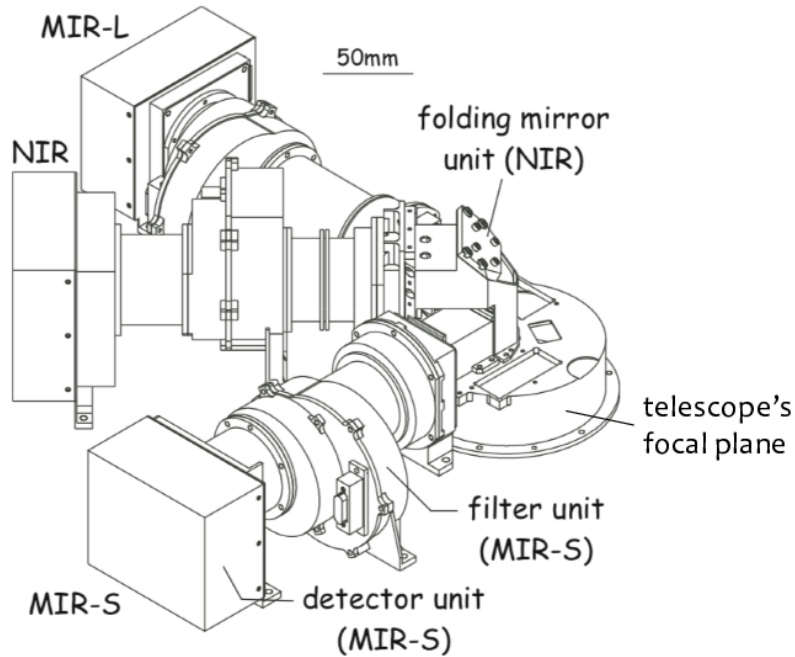


Figure 2.1: Bird's-eye view of the IRC (Onaka et al. 2007).

directions in the geocentric ecliptic coordinate, $(\lambda_{\oplus}, \beta_{\oplus})$. They cover the entire sky except the galactic plane, in which the thermal emission from the interstellar dust in our galaxy dominates the sky brightness in the mid-infrared.

In this study, I used the spectra obtained with the MIR-S channel, which covered $5.4\text{--}12.9\ \mu\text{m}$ with the spectral resolution of $R \sim 50$, which is optimum to investigate the silicate features around $10\ \mu\text{m}$. These data were taken with two gratings, SG1 ($5.4\text{--}8.4\ \mu\text{m}$) and SG2 ($7.5\text{--}12.9\ \mu\text{m}$), in the spectroscopic observation mode (IRC04 in terms of the astronomical observation template). In this mode, the IRC takes four spectroscopic frames with the SG1 grism, then takes an imaging frame, and finally takes four spectroscopic frames with the SG2 grism. The imaging frame is used to determine the wavelength reference point for slit-less spectroscopy in the main field of view. Each frame consists of 1 short exposure (0.5844 sec) and 3 long exposures (16.3632 sec). For each pointing observation, I analyzed the data of the long exposures in the spectroscopic frames: 12 long exposures in total ($3\ \text{long exposures} \times 4\ \text{spectroscopic frames}$) for each of the SG1 and the SG2.

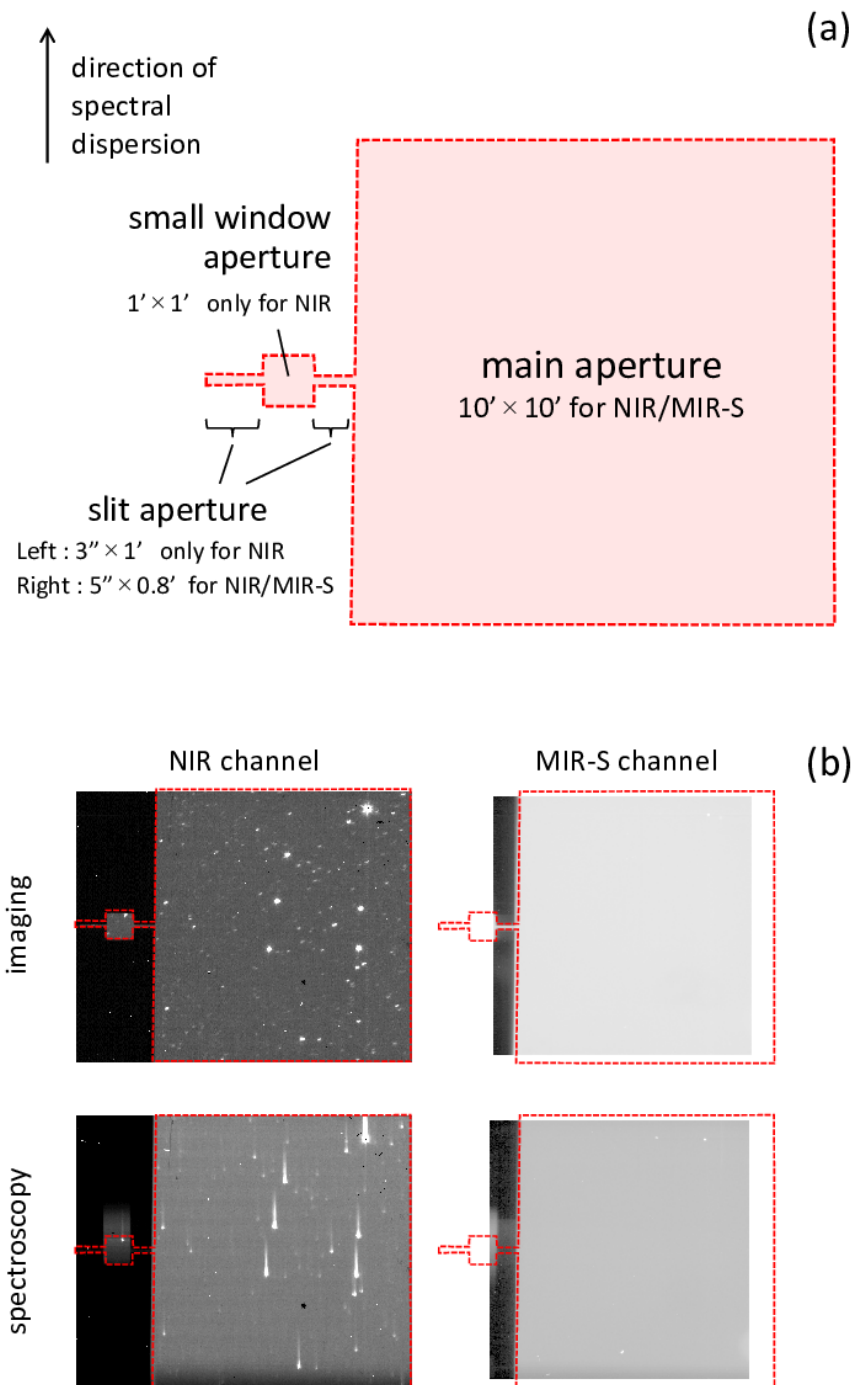


Figure 2.2: (a) Schematic view of an aperture on the telescope focal plane. This aperture is common to the NIR and MIR-S channels. (b) Correspondence between the aperture area on the telescope focal plane (surrounded by a red dashed line) and the detector sensitive area in the NIR or MIR-S channel (background image). Detector image do not cover the entire field of view of the aperture in the MIR-S channel. I demonstrated examples of detector images obtained in imaging and spectroscopic observations at $(\lambda_{\oplus}, \beta_{\oplus}) = (174^{\circ}.13, -1^{\circ}.00)$. Their brightnesses is individually scaled to show the images clearly.

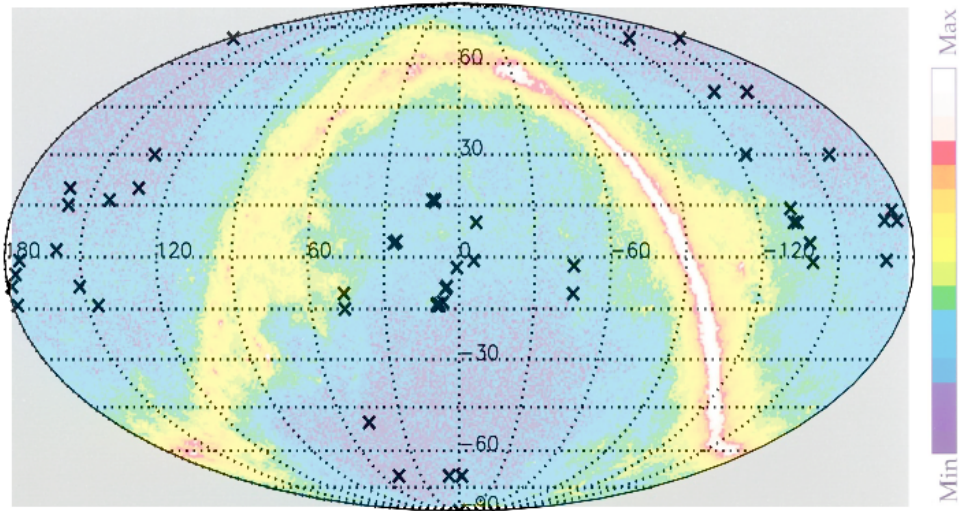


Figure 2.3: Map of the pointing directions I observed. This is a Mollweide projection in geocentric ecliptic coordinates. The background image is the brightness map at $140 \mu\text{m}$ obtained with COBE/DIRBE (Kelsall et al. 1998), which is dominated by thermal emission from the interstellar dust in our Galaxy. The bright arc corresponds to the galactic plane.

Table 2.1: Log for the 74 pointing observations. Pointing directions were written in 3 types of celestial coordinates: equatorial coordinates (α, δ) , geocentric ecliptic coordinates $(\lambda_{\oplus}, \beta_{\oplus})$, galactic coordinates (l, b) . Solar elongations in all observations were in the range of 90 ± 1 degree.

Observation ID	Date(UT)	α [deg]	δ [deg]	λ_{\oplus} [deg]	β_{\oplus} [deg]	l [deg]	b [deg]
1500701	2006/12/16 18:35:01	174.22	1.41	174.13	-1.00	264.99	58.68
1500703	2006/12/20 16:55:29	175.02	-7.11	178.27	-8.50	273.59	51.65
1500704	2006/11/22 18:56:11	150.22	3.09	151.20	-8.50	235.92	42.71
1500705	2007/02/04 16:40:21	226.81	-7.14	226.40	10.00	351.68	42.52
1500706	2007/02/05 19:08:19	228.04	-3.33	226.53	14.00	356.54	44.40
1500707	2007/02/05 13:21:40	46.69	6.59	46.13	-10.50	172.07	-43.01
1500708	2007/02/05 10:01:47	48.07	2.30	46.27	-15.00	177.62	-45.09
1500709	2006/12/15 05:23:58	349.86	6.51	353.27	10.00	86.08	-49.66
1500711	2007/02/05 14:00:26	239.22	31.05	227.00	50.00	49.93	49.59
1500712	2007/02/04 19:47:57	239.31	31.03	227.13	50.00	49.90	49.50
1500713	2006/12/16 09:28:29	355.14	-3.19	354.27	-1.00	84.58	-60.67
1500715	2006/12/15 07:03:14	349.86	6.51	353.27	10.00	86.08	-49.66
1500717	2006/12/17 05:50:18	226.05	60.54	176.40	70.00	98.30	49.76
1500718	2006/12/17 07:29:34	226.05	60.54	176.40	70.00	98.30	49.76
1500719	2006/11/10 11:15:25	90.00	-66.56	90.00	-90.00	276.38	-29.81

(Continued)

Observation ID	Date(UT)	α [deg]	δ [deg]	λ_{\oplus} [deg]	β_{\oplus} [deg]	l [deg]	b [deg]
1500720	2006/11/10 19:31:34	90.00	-66.56	90.00	-90.00	276.38	-29.81
1500721	2007/02/04 21:21:44	248.99	49.66	227.27	70.00	76.65	41.96
1500722	2007/02/03 17:13:21	249.05	49.64	227.40	70.00	76.61	41.92
1500723	2006/12/28 13:11:21	230.95	57.48	188.00	70.00	92.19	49.56
1500724	2006/12/28 14:50:38	230.95	57.48	188.00	70.00	92.19	49.56
1500725	2007/02/05 14:50:05	59.22	-31.05	47.00	-50.00	229.93	-49.59
1500726	2007/02/05 06:27:59	68.92	-49.68	47.13	-70.00	256.68	-42.00
1500727	2006/12/19 04:59:29	46.71	-60.10	358.00	-70.00	277.46	-49.79
1500728	2006/12/19 06:38:46	46.71	-60.10	358.00	-70.00	277.46	-49.79
1500729	2006/12/20 07:27:51	46.76	-60.06	358.13	-70.00	277.39	-49.80
1500730	2006/12/20 09:07:08	46.76	-60.06	358.13	-70.00	277.39	-49.80
1500731	2006/12/28 14:01:00	50.95	-57.48	8.00	-70.00	272.19	-49.56
1500732	2006/12/28 15:40:16	50.95	-57.48	8.00	-70.00	272.19	-49.56
1500748	2007/05/02 14:28:54	141.03	36.33	131.80	20.00	187.57	45.50
1500751	2007/05/02 17:50:27	145.57	45.73	131.67	30.00	173.52	48.41
1500759	2007/05/05 21:07:43	320.39	-26.49	314.53	-10.50	21.13	-43.53
1500760	2007/05/05 19:26:06	317.83	-18.84	314.60	-2.50	29.97	-39.06
1501603	2007/06/17 08:56:51	174.34	-3.00	176.00	-5.00	269.39	54.98
1501607	2007/06/19 12:17:06	172.52	-12.03	178.00	-14.00	273.55	46.15
1501608	2007/06/19 13:56:33	172.52	-12.03	178.00	-14.00	273.55	46.15
1501609	2007/05/30 10:09:52	165.66	22.42	158.00	15.00	217.73	64.91
1501614	2007/05/31 15:55:55	161.83	9.86	159.50	2.00	237.54	56.04
1501615	2007/07/13 10:01:20	210.04	19.93	200.00	30.00	12.02	72.70
1501617	2007/06/01 10:14:34	169.80	26.21	160.00	20.00	210.22	69.40
1501618	2007/06/01 13:33:25	169.80	26.21	160.00	20.00	210.22	69.40
1501619	2007/08/09 17:03:30	239.22	31.05	227.00	50.00	49.93	49.59
1501620	2007/08/10 11:18:01	239.22	31.05	227.00	50.00	49.93	49.59
1501623	2007/06/23 11:39:56	2.11	-2.35	1.00	-3.00	98.55	-63.17
1501625	2007/07/02 13:40:07	193.31	5.70	190.00	10.50	304.17	68.57
1501627	2007/07/03 12:49:22	189.72	-5.27	191.00	-1.00	297.11	57.46
1501628	2007/07/03 14:28:50	189.72	-5.27	191.00	-1.00	297.11	57.46
1501629	2007/06/27 11:49:36	7.97	-5.82	5.00	-8.50	109.73	-68.18
1501631	2007/06/27 13:29:03	7.97	-5.82	5.00	-8.50	109.73	-68.18
1501633	2007/06/27 15:58:47	188.77	7.65	185.00	10.50	290.92	70.14
1501635	2007/06/28 10:13:36	190.89	10.01	186.00	13.50	296.38	72.78
1501639	2007/07/23 17:08:43	227.13	35.10	210.00	50.00	56.76	59.76
1501640	2007/07/23 23:46:38	227.13	35.10	210.00	50.00	56.76	59.76
1501645	2007/06/27 18:27:33	8.62	-6.08	5.50	-9.00	111.33	-68.57
1501646	2007/06/27 20:07:00	8.62	-6.08	5.50	-9.00	111.33	-68.57
1501647	2007/06/28 17:41:00	11.14	-9.35	6.50	-13.00	117.40	-72.15
1501648	2007/06/28 19:20:27	11.14	-9.35	6.50	-13.00	117.40	-72.15
1501649	2007/05/13 17:11:43	150.43	29.70	142.00	16.50	198.71	52.80
1501653	2007/07/02 12:42:56	2.41	19.08	10.00	16.50	109.45	-42.70
1501654	2007/07/02 14:22:32	2.63	18.62	10.00	16.00	109.59	-43.19
1501655	2007/07/03 18:33:12	3.34	19.47	11.00	16.50	110.72	-42.49

(Continued)

Observation ID	Date(UT)	α [deg]	δ [deg]	λ_{\oplus} [deg]	β_{\oplus} [deg]	l [deg]	b [deg]
1501660	2007/05/16 16:17:52	143.10	-0.19	145.50	-14.00	234.23	34.98
1501661	2007/07/01 18:37:11	13.60	-8.84	9.00	-13.50	125.28	-71.70
1501662	2007/07/01 20:16:47	13.81	-9.30	9.00	-14.00	125.98	-72.15
1501663	2007/06/30 17:45:20	12.70	-9.23	8.00	-13.50	122.42	-72.10
1501664	2007/06/30 12:47:06	12.90	-9.69	8.00	-14.00	123.08	-72.56
1501669	2007/07/18 11:43:02	21.47	13.86	25.00	4.50	135.52	-48.17
1501670	2007/07/18 13:22:31	21.47	13.86	25.00	4.50	135.52	-48.17
1501671	2007/07/19 00:58:59	22.61	13.77	26.00	4.00	137.18	-48.02
1501672	2007/07/19 10:55:51	22.61	13.77	26.00	4.00	137.18	-48.02
1501673	2007/08/02 23:58:04	217.10	-16.24	220.00	-1.50	334.24	40.67
1501675	2007/08/04 00:51:59	219.84	-11.32	221.00	4.00	340.75	43.48
1501679	2007/08/19 12:27:54	240.55	9.97	236.00	30.00	21.43	41.99
1501680	2007/08/19 14:07:25	240.55	9.97	236.00	30.00	21.43	41.99
1501685	2007/08/08 11:01:27	225.47	-6.76	225.00	10.00	350.68	43.69

Chapter 3

Data reduction

3.1 Instrumental artifacts

With a conventional reduction toolkit (Ohyama et al. 2007), the resultant SG1 and SG2 spectra were not smoothly connected owing to the inconsistency in the intensity level of the overlapping wavelength range (i.e., 7.5–8.4 μm). I have carefully examined the contribution of the possible artifacts due to the instrument and identified three types of artifacts that affect the slit-spectroscopic data: (1) the light scattered in detector pixels, (2) the light scattered at the edge of a detector, and (3) the ghost of the small window aperture. They are schematically shown in Figure 3.1 and their details are described in this section.

3.1.1 The light scattered in detector pixels

A small fraction of incident light into a detector pixel are scattered into other pixels in the same row and column of the pixel array, even if they do not saturate.

The brightness profile of this component was empirically estimated in Appendix 2 in Sakon et al. (2007). In imaging data obtained in the MIR-S channel, bright point sources in the main field of view cause the cross lines vertically and horizontally. According to careful investigations of the brightness of such cross lines, it is derived that the light with the intensity S_{10} [ADU] incident at the pixel position (X_0, Y_0) is scattered into the pixel position (X, Y_0) with the fraction of

$$G_1(X - X_0) = \frac{C}{1 + \left(\frac{X - X_0}{22.6}\right)^2} \quad [\text{ADU}], \quad (3.1)$$

where $C = 7.73 \times 10^{-4}$ and 6.23×10^{-4} for S7 and S11, respectively. The S7 and the S11 are the

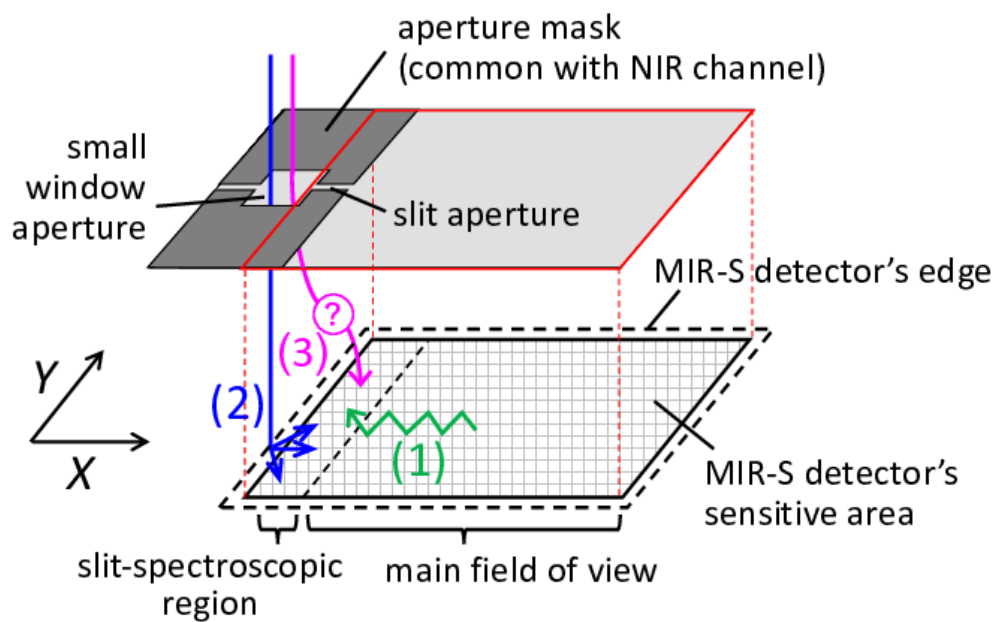


Figure 3.1: Schematic view of artificial components: (1) the light scattered in detector pixels, (2) the light scattered at the edge of a detector, and (3) the ghost of the small window aperture. Actually, optical elements like a beam splitter, two lens and a grism were included between the aperture mask and the detector. The rectangular coordinate is defined with the origin at the left bottom edge of the detector pixel array and the Y-axis along the direction of spectral dispersion.

filters used for the imaging observations and the wavelength coverages correspond to that of the SG1 and the SG2, respectively. The profiles described in equation (3.1) are plotted in Figure 3.2. This formula can be used also for the scattering along the Y -axis. The actual brightness of this component at each position is determined by the convolution of the light scattered from all pixels in the same row and column:

$$S_1(X, Y) = \int_1^{256} S_{10}(X_0, Y) \times G_1(X - X_0) dX_0 + \int_1^{256} S_{10}(X, Y_0) \times G_1(Y - Y_0) dY_0 \quad [\text{ADU}]. \quad (3.2)$$

If we care about their effect on the slit-spectroscopic region, the light leaking from the main field of view along the X -axis is dominant (see (1) in Figure 3.1). I calculated the two-dimensional brightness distribution of the leaking light for each pointing data. After initial processing of observed image, I approximately assumed the brightness distribution in the processed image itself as the distribution of S_{10} , because the fraction of the included scattered light is as small as 10^{-4} (the order of C in equation (3.1)) of the incident light. Using the value of S_{10} at each pixel position, I calculated S_1 from equation (3.2). The panel (a) in Figure 3.5 shows an example of the estimated brightness distribution of this component. I subtracted it from the processed image.

3.1.2 The light scattered at the edge of a detector

As mentioned in section 2.2, the detector sensitive area in the MIR-S channel do not completely cover the field of view of the aperture which is shared with the NIR channel. Therefore, some of light which go through the small window aperture could be scattered by the edge of the detector in the MIR-S channel and contaminate the slit-spectroscopic region (see (2) in Figure 3.1).

The brightness profile of this component was also empirically estimated in Appendix 1 in Sakon et al. (2007). Some datasets of two images were picked up from the imaging data in the MIR-S channel; one image of each dataset accidentally showed a clear line of this scattered light caused by a bright point source illuminating the detector edge (see the image (a) in Figure 3.3), and in the counterpart, the pointing direction was slightly dithered and the point source was properly imaged in the main field of view (see the image (b) in Figure 3.3). The counterpart image was subtracted from the image with the scattered light after the correction of the position shift. This subtraction extracted the brightness due to the scattered light. The brightness profile was estimated as the function of the distance from the edge of the detector. The intrinsic brightness, S_{20} , of the point source can be measured in the counterpart image. Figure 3.4 shows the brightness profile, $S_2(X)$, of the scattered light normalized by S_{20} .

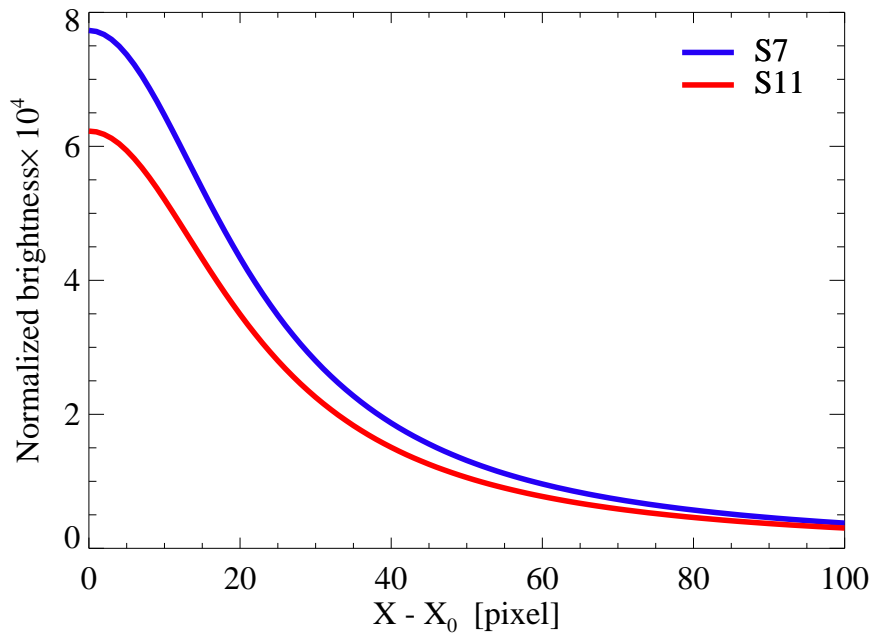


Figure 3.2: Brightness profile, $G_1(X - X_0)$, of the light scattered in detector pixels. The absolute value is normalized by the brightness, S_{10} , of the source causing the scattered light. S7 and S11 are the filters used for the imaging observations and the wavelength coverages correspond to that of the SG1 and the SG2, respectively. I used the profile obtained with the S7 for the SG1 and the S11 for the SG2.

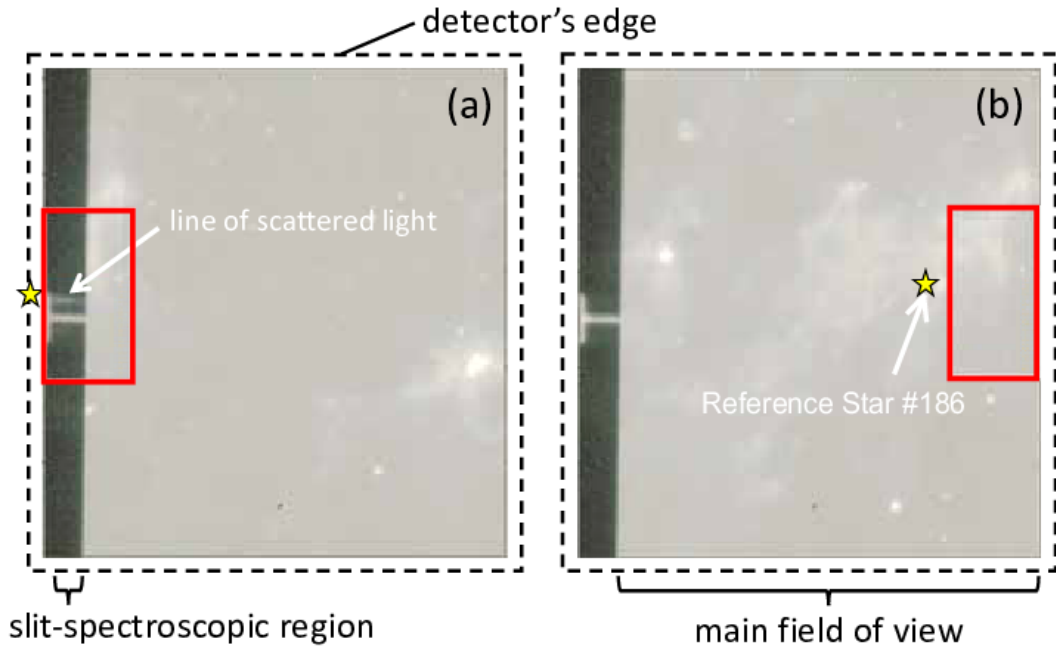


Figure 3.3: Example of the datasets used for the estimation of the brightness profile of the light scattered at the detector edge. The pointing directions of two images was slightly dithered. Image (a) shows a line of the scattered light in the slit-spectroscopic region, and image (b) captures the point source which illuminates the detector edge and causes the scattered light in image (a), in the main field of view. The point source is marked by yellow stars. The red rectangles indicate the same field of view in these two dispersed images. I got the original image from Dr. I. Sakon at the University of Tokyo.

According to data obtained in the NIR channel, no bright point source contaminated the field of view of the small window aperture in all data I used. Therefore, I assumed that the brightness is uniform in the field of view of the small window. As seen in the right bottom image in the panel (b) of Figure 2.2, the spectrum of the incident light going through the edge of the small window aperture illuminates a few pixel columns at the edge of the detector sensitive area. I replaced the brightness in such pixel columns as the brightness illuminating the detector edge, S_{20} , and calculated the brightness distribution of S_2 as the panel (b) in Figure 3.5. Note that I optimized some parameters of the profile $S_2(X)/S_{20}$ described in Figure 3.4 for the diffuse source of the scattered light.

3.1.3 The ghost of a small window aperture

Even after the subtraction of two types of scattered light mentioned above, I still found the inconsistency in spectra obtained with the SG1 and the SG2. It seems to be due to the ghost of the light going through the small window aperture. In the NIR channel of AKARI/IRC, a lot of point source

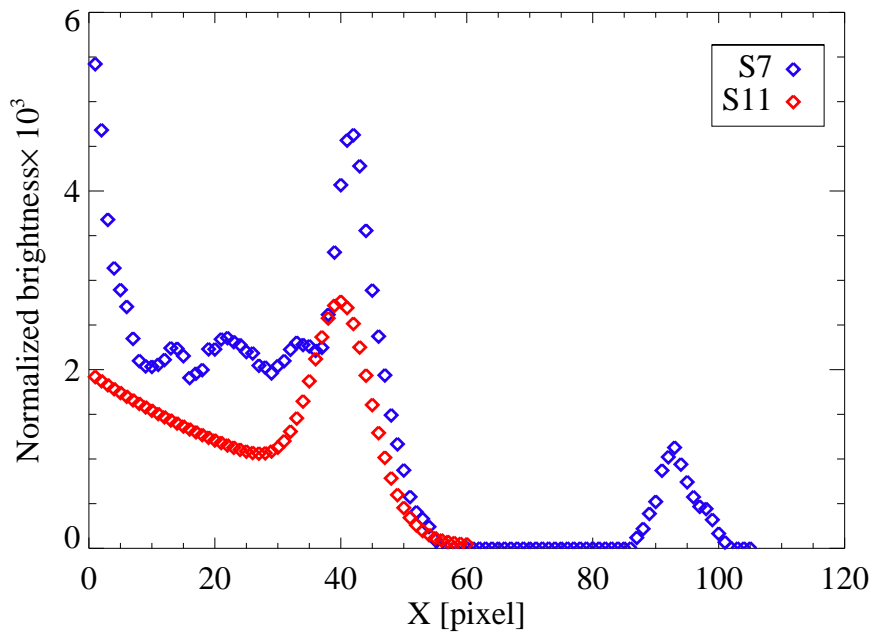


Figure 3.4: Brightness profile, $S_2(X)$, of the light scattered at the edge of a detector. The absolute value is normalized by the brightness, S_{20} , of the source causing the scattered light. S7 and S11 are the filters used for the imaging observations and the wavelength coverages correspond to that of the SG1 and the SG2, respectively. I used the profile obtained with the S7 for the SG1 and the S11 for the SG2.

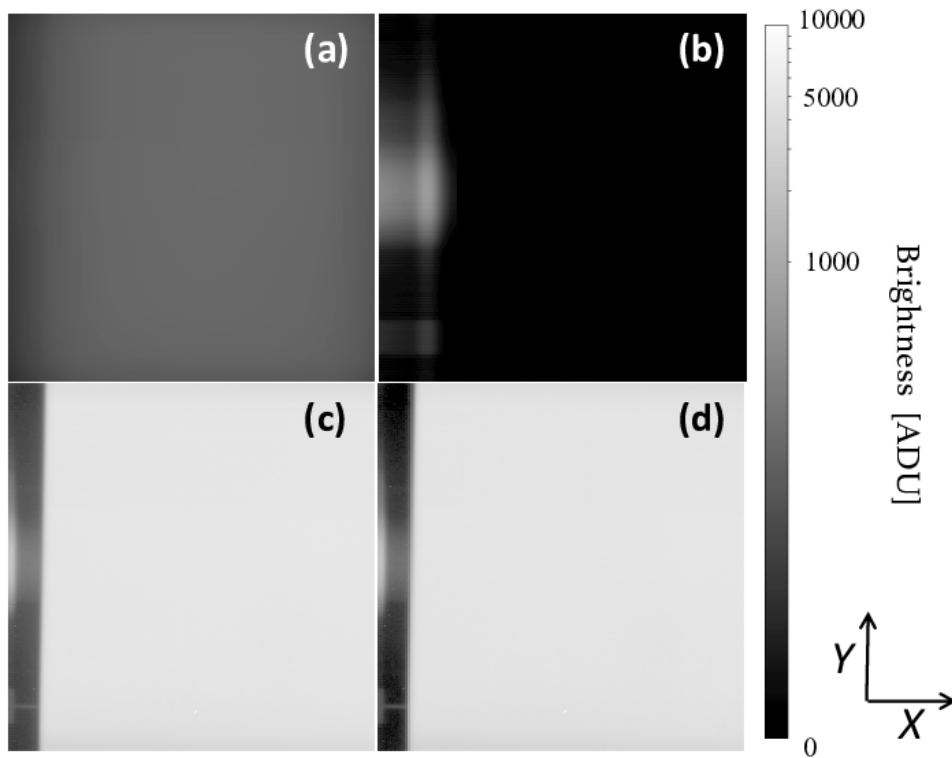


Figure 3.5: Two-dimensional images of (a) the light scattered in detector pixels from the main field of view scaled by a factor of 20, (b) the light scattered at the edge of a detector after going through the small window aperture scaled by a factor of 100, and before and after the subtraction of these scattered light, (c) and (d), respectively. This is an example in the case of data pointed at $(\lambda_{\oplus}, \beta_{\oplus}) = (174^{\circ}.13, -1^{\circ}.00)$ in observation-ID of 1500701.1 and obtained with the SG2.

objects have been pointed in the small window aperture in order to obtain the near-infrared spectra. Although the brightness of stars and typical galaxies are reduced in the mid-infrared, some of the objects, ultra luminous infrared galaxy (ULIRG) for example, are bright also in the mid-infrared. I carefully checked the imaging data obtained with the MIR-S channel in which a bright ULIRG was pointed in the small window aperture for the NIR channel. As the result, I found a clear ghost component in the slit-spectroscopic region of such images like Figure 3.6.

For the estimation of the brightness profile of the ghost in spectroscopic images, I assumed that the ghost do not contaminate the spectroscopic region of the small window aperture itself, i.e., the edge columns of the detector pixel array (see the upper half of Figure 3.7). From the combination of the spectra of the small window aperture and the slit without any point sources, the brightness profile of the ghost was estimated by the following steps. These steps were performed by I. Sakon and summarized in the lower half of Figure 3.7.

1. After one-dimensional spectra of the slit (slit spectra) were extracted from two-dimensional images, they were convolved with the width of the small window aperture (corresponding to 25 pixel, while the slit width is ~ 2 pixel). Since the zodiacal emission is an uniform background in such spatial scale, this convolved spectra can be considered as a model spectra of the small window aperture including the convolved ghost.
2. One-dimensional spectra of the small window aperture (window spectra) were extracted using the data at the edge columns of the pixel array and subtracted from their model spectra derived in the previous step. Since the extracted window spectra are assumed not to include the ghost, this subtraction produces the brightness profiles of the ghost convolved with the width of the small window aperture.
3. The profiles were de-convolved with the width of the small window aperture.

The shape of the derived profiles seemed to be common in all data, and the absolute value was roughly proportional to the typical value of the mid-infrared brightness incident into the small window aperture (see Appendix 3 for details). If no bright source is seen and the zodiacal emission is the dominant source in the small window aperture, the mid-infrared brightness in the small window aperture is proportional to the median value of the brightness at the center of the main field of view, i.e., the integrated brightness of the 0th, the 1st, and the 2nd order light of the zodiacal emission spectrum. Figure 3.8 shows the obtained ghost profile normalized by the median value of the brightness at the center of the main field of view.

I used the normalized profile in Figure 3.8 and determined the absolute value appropriate for each

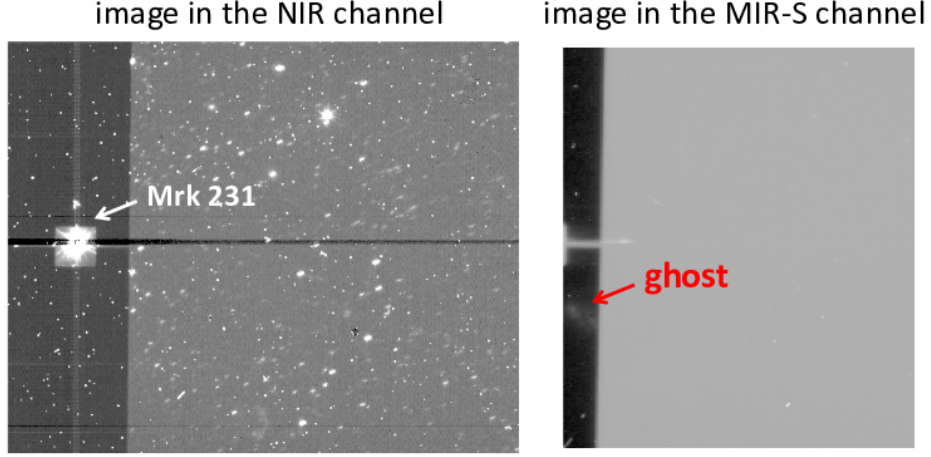


Figure 3.6: Example of the datasets indicating the clear ghost of a small window aperture: the image obtained with the NIR channel shows a bright ULIRG, Mrk 231, in the small window aperture (left) and it causes the ghost image in the slit-spectroscopic region of the image obtained with the MIR-S channel (right). The observation-ID of this dataset is 1100271.

pointing data by the fitting to the observed brightness profile. If artifacts are completely removed, brightness in the regions where the optical system has no response should be zero. However, the brightness in such regions was actually non-zero even after the subtraction of the scattered light (1) and (2). I considered the non-zero brightness to originate from the ghost of the small window aperture. Therefore, I fitted the following function $S_3(Y)$ to the non-zero brightness seen in the regions without the system response.

$$S_3(Y) = a + b Y + c G_3(Y) \quad [\text{ADU}] , \quad (3.3)$$

where $G_3(Y)$ is the brightness profile in Figure 3.8. The linear terms $a + b Y$ indicate the linear offset needed to correct the residual. This offset may correspond to the ghost component of the main field of view, although I could not conclude. Constant a , b , and c were free parameters and optimized in each pointing data individually so that $S_3(Y)$ becomes identical to the non-zero brightness in the regions without the system response. As the regions without the system response, I selected the pixel range of $25 \leq Y \leq 80$ or $180 \leq Y \leq 240$ for the SG1, and $45 \leq Y \leq 90$ or $200 \leq Y \leq 240$ for the SG2, in order to avoid the contribution of the target brightness in all dispersion orders, the 0th, 1st and 2nd order. I present an example of the brightness profiles before and after the subtraction of the ghost component and the profiles of this ghost component itself in Figure 3.9.

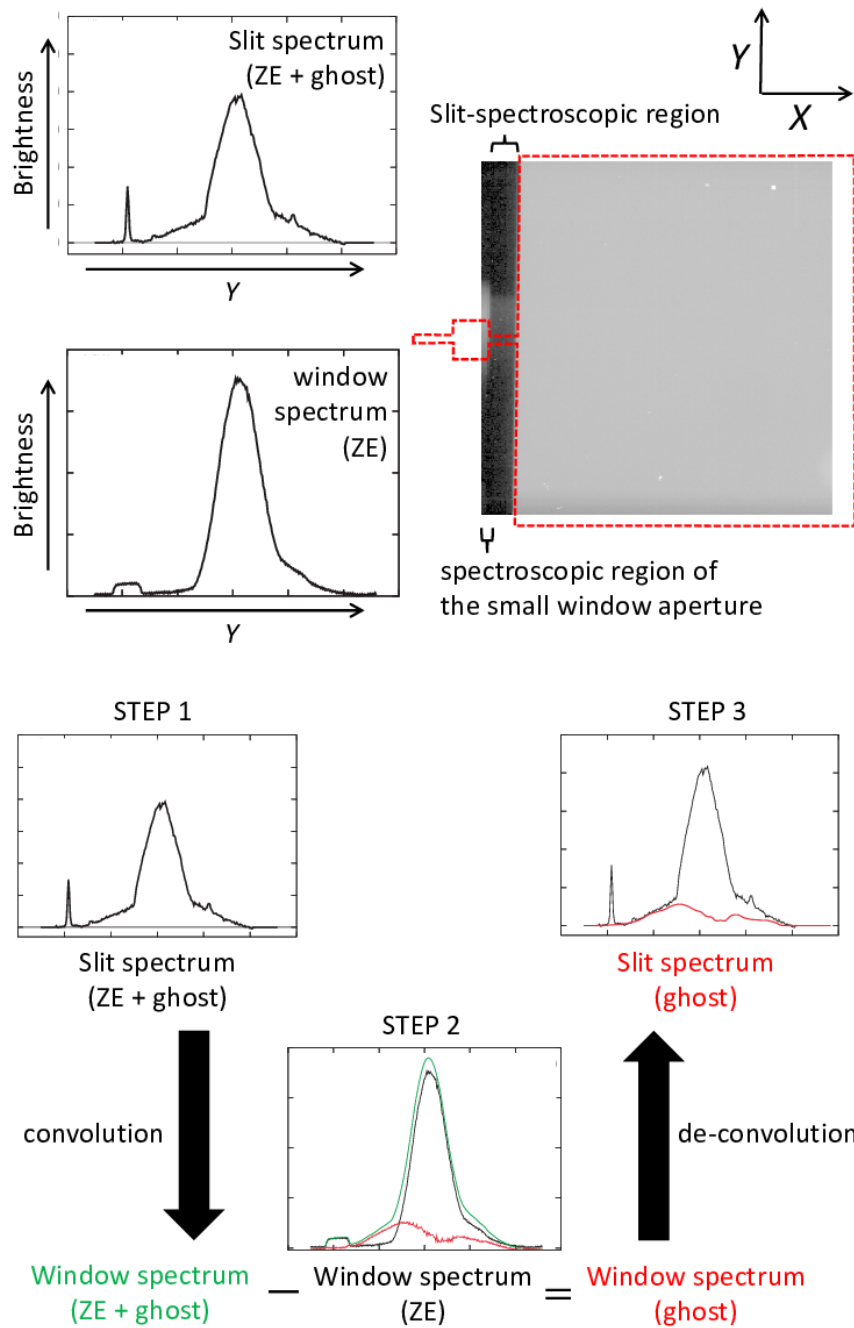


Figure 3.7: The upper half: an example dataset of slit spectra including ghost and window spectra assumed not to include ghost. The lower half: The schematic drawing of three steps to estimate the brightness profile of the ghost. The text colors correspond to the line colors in each panel.

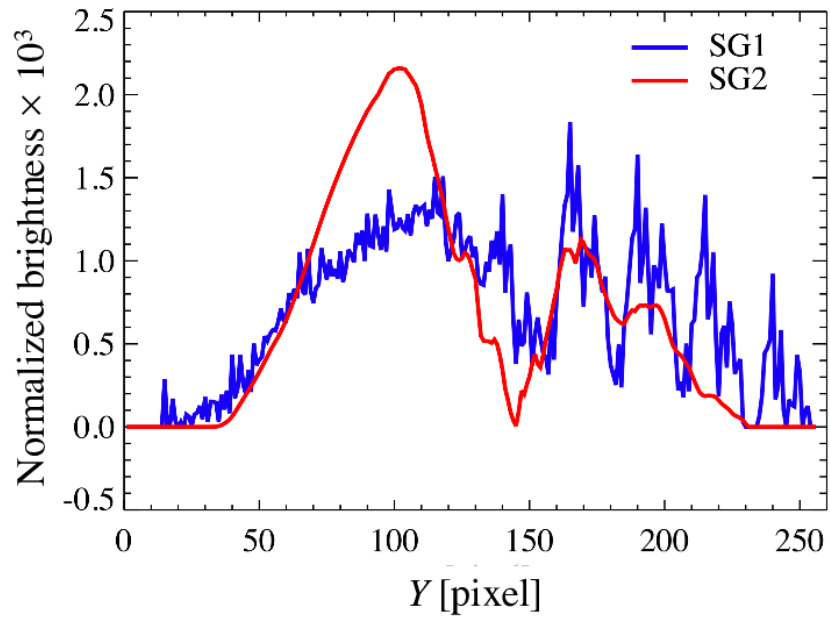


Figure 3.8: Brightness profile of the ghost of the small window aperture normalized by the typical brightness incident into the small window aperture. Y means the pixel position along the direction of spectral dispersion as defined in Figure 3.1. These curves correspond to the $G_3(Y)$ in equation (3.3).

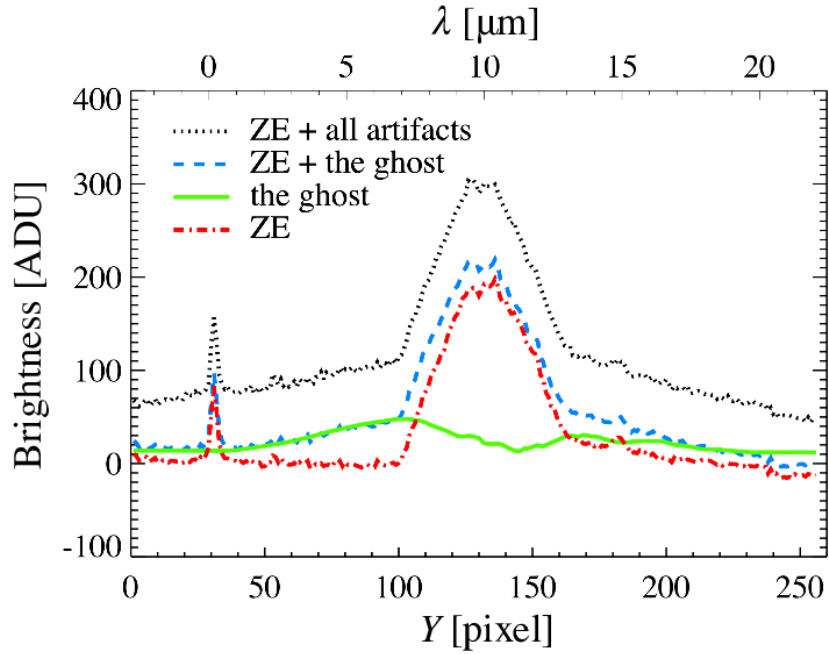


Figure 3.9: Brightness profiles in the slit-spectroscopic region. The brightness originates from the zodiacal emission, denoted by ZE, with all artifacts (black), only with the ghost component after other two artificial components of scattered lights were subtracted (blue), and with no artifacts after the subtraction of all artifacts (red). The green line indicates the brightness profile of the ghost component and corresponds to the difference between blue one and red one. Y means the pixel position along the direction of spectral dispersion as defined in Figure 3.1. At the top side, I show the corresponding wavelength calculated in our wavelength calibration method. The 0th and 2nd order light was seen in $Y \sim 30$ and $160 \leq Y \leq 200$, respectively. This is an example in the case of data pointed at $(\lambda_{\oplus}, \beta_{\oplus}) = (174^{\circ}.13, -1^{\circ}.00)$ in observation-ID of 1500701.1 and obtained with the SG2.

3.2 Reduction flow

The flow of our data reduction procedures including the subtraction of those artifacts is described in the following summarized in Figure 3.10.

For each pointing, I started from the raw data of 12 two-dimensional images taken with each grism: 3 exposures \times 4 frames. First, I subtracted a dark image from each images. The dark image was obtained at the first of all observations and scaled by the typical value of the dark image taken just before each pointing observation in order to correct a long-term variation of hot pixels. After the correction of detector linearity, I made a median image from these 12 images. This procedure removed the contamination of cosmic ray events. Then, artificial images of two scattered light components, artifact (1) and (2), were subtracted from the median image.

I extracted a one-dimensional profile from the two-dimensional image of the slit-spectroscopic region by calculating the median values of 10 pixels along the spacial direction ($13 \leq X \leq 22$ for SG1, $10 \leq X \leq 19$ for SG1). The spatial variation was treated as a statistical error. Assuming they followed the gaussian distribution, the error was calculated as the median absolute deviation (MAD) scaled by a factor of 1.4826 (Mosteller & Tukey 1977; Tukey 1977). From the extracted one-dimensional profile with errors, I subtracted an estimated profile of the artifact (3).

The final procedure was a spectrum calibration. I converted the pixel position and the signal to the corresponding wavelength and intensity, respectively. For the conversion, I used the parameters presented in Appendix 4 of Sakon et al. (2007). The pixel-to-wavelength relation was derived using significant gas emission lines ([ArIII], [SIV], and [NeII]; Bernard-Salas et al. 2003) seen in the slit-spectroscopic data of NGC6543, one of the well-known planetary nebula. I used the following relation:

$$\lambda = 0.057 \times (Y - 12) + 0.016 \quad \text{for SG1,} \quad (3.4)$$

$$\lambda = 0.099 \times (Y - 31) + 0.141 \quad \text{for SG2,} \quad (3.5)$$

where λ means the corresponding wavelength in unit of μm and Y indicates the pixel position along the direction of spectral dispersion as defined in Figure 3.1. To calibrate the intensity at each wavelength, I derived a response curve by referring to the spectroscopic data of two standard stars, KT09T1 and HD42525, and the model spectra provided by Dr. M. Cohen and coworkers (Cohen et al. 1995, 1996, 1999, 2003). Since the AKARI spectra were taken in the main field of view, the uncertainty in the detections of the reference source position ($< \pm 0.5$ pixel), which resulted in the wavelength shift of the reference spectra ($< \pm 0.0285 \mu\text{m}$, $\pm 0.0496 \mu\text{m}$ in the SG1 and the

SG2, respectively), was taken into account as a cause of statistical errors in the response curve. I propagated this error to the resultant spectra. I presented the used response curve in Figure 3.11.

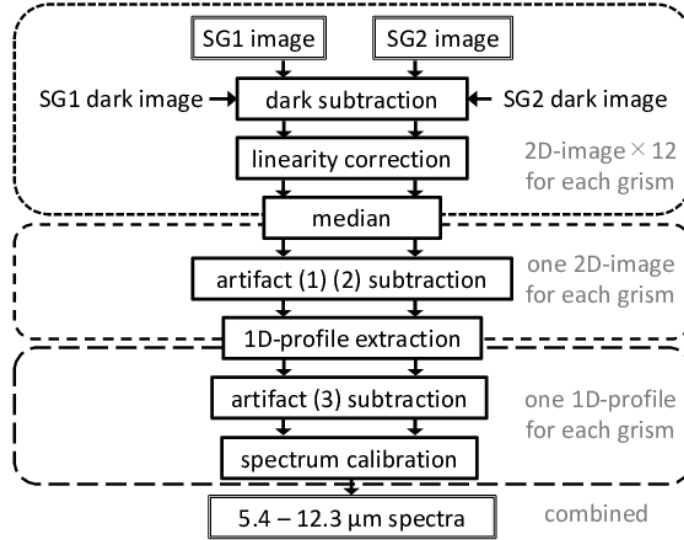


Figure 3.10: The data-reduction flow I performed.

3.3 Obtained spectra

Finally, I succeeded in subtracting three types of artificial components and deriving reasonable spectra smoothly connected between data in the SG1 and the SG2 for all pointing data. Figure 3.12 shows an example of obtained spectra before and after the subtraction. It is clear that the subtraction of artifacts contradict the inconsistency in the intensity level of the overlapping wavelength range between the SG1 and the SG2. They included two types of statistical errors: the spatial dispersion during the extraction of the one-dimensional profiles and the uncertainty of the response curve I used. Those errors were much smaller than any other spectra obtained in past observations for the zodiacal emission. In all obtained spectra, I found bumps around $10 \mu\text{m}$, which correspond to excess emission above the blackbody continuum.

Obtained intensity levels are consistent in $\sim 10\%$ accuracy with those calculated on the basis of the DIRBE zodi-model introduced in section 1.1.2. Figure 3.13 shows the correlation of intensities at $12 \mu\text{m}$ between this work and the DIRBE zodi-model. The 10% inconsistency may be caused by the inappropriate color correction factor used in the DIRBE model construction. In Kelsall et al. (1998), they assumed the color correction factor appropriate for the blackbody of a single temperature in

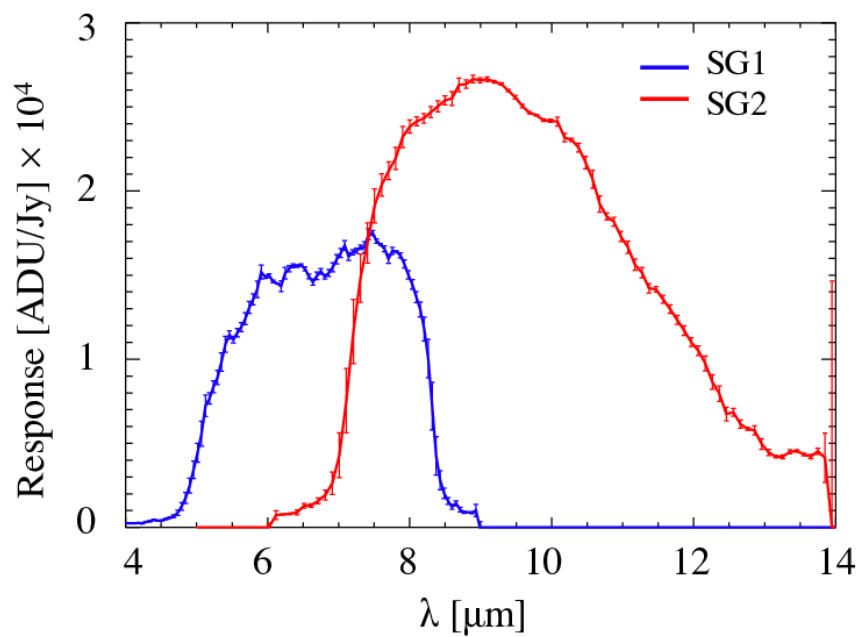


Figure 3.11: The response curve used in this work. The blue and red line indicate that for the SG1 and the SG2, respectively. Although flatness is seen at the edge of longer side in each curve ($> 8.5 \mu\text{m}$ for the SG1 and $> 13.0 \mu\text{m}$ for the SG2), which is due to contamination of the light in the second order dispersion, I did not use the data in such edge regions of effective wavelength ranges. I used the data in the wavelength range where response is more than half of the max value.

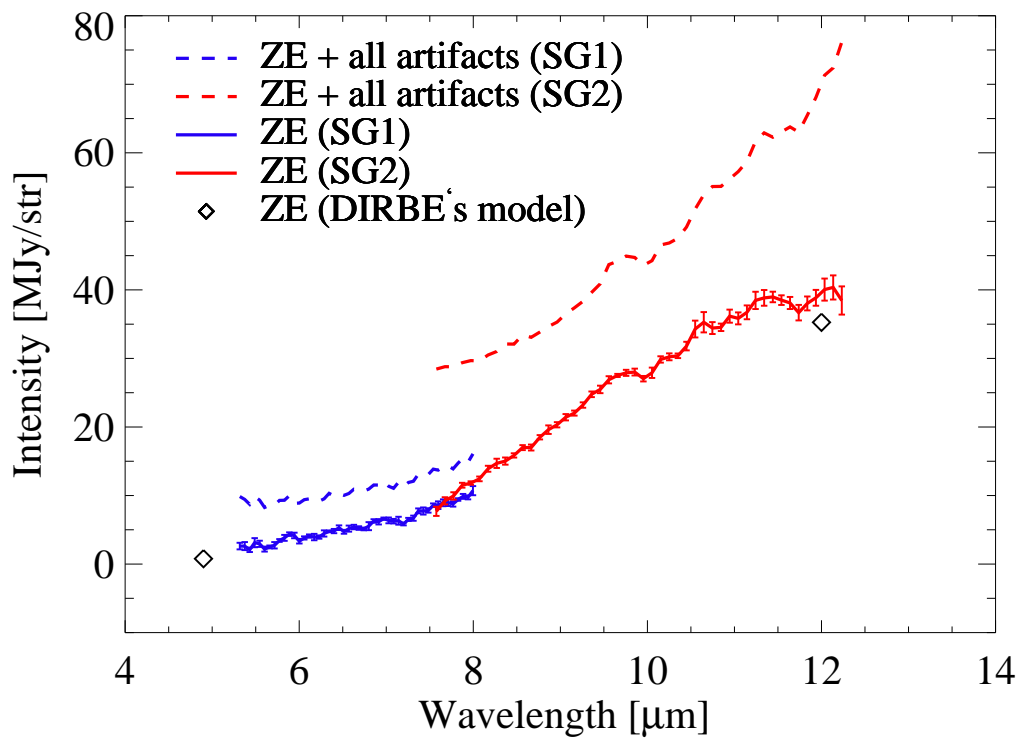


Figure 3.12: Spectra obtained with the SG1 and the SG2 before and after the subtraction of three types of artifacts. This is an example in the case of data pointed at $(\lambda_{\oplus}, \beta_{\oplus}) = (174^{\circ}.13, -1^{\circ}.00)$ in observation-ID of 1500701.1.

the band width of 8.8–15.2 μm . However, in this work, I found that there were deviations of the actual intensity from the blackbody due to silicate features. Actual spectra may have an intensity level lower than the blackbody at the longer side of the band width, while the 12 μm intensity level is the same as, or even above, the blackbody because it corresponds to the longer edge of emission features. In such situation, color correction appropriate for the blackbody presents the lower 12 μm intensity level than actual.

I also confirmed the consistency with the IRC zodi-model. Figure 3.14 shows the correlation of intensities at 9 μm between this work and the IRC zodi-model. In this case, the intensity levels obtained in this work were lower than the model prediction. This may be due to the overestimation of the 9 μm intensity levels in the IRC zodi-model. In this model, as well as the DIRBE zodi-model, the color correction factor was appropriated for the blackbody of a single temperature in the band width of 6.7–11.6 μm . This wavelength range includes almost whole emission features from silicates. In addition, the thermal emission from high temperature particles (i.e., carbonaceous or other strongly absorbing materials and/or stochastically-heated small particles) is added to the blackbody of the typical temperature in the IPD and it causes significant excess at the shorter side of the wavelength range (Reach et al. 2003). As the result, the 9 μm intensity levels can be overestimated owing to the strong excess above a blackbody at neighbor wavelengths, if color correction is appropriated for the simple blackbody.

It was confirmed that the intensity levels in the obtained spectra were consistent with that predicted by the DIRBE zodi-model and the IRC zodi-model at least within 10% accuracy. This indicates that artificial components have been accurately subtracted. Since I focused on the relative dependence of intensities on wavelengths in this work, I did not consider the roughly 10% errors in absolute intensities.

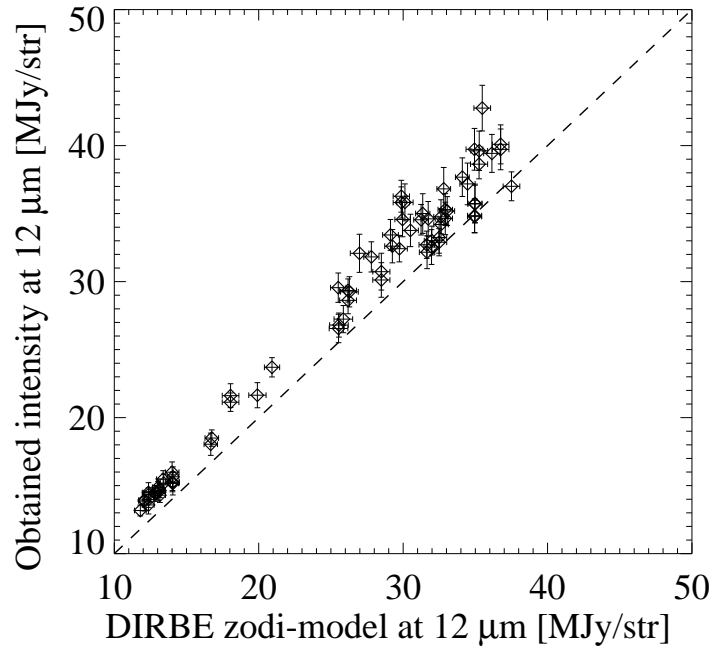


Figure 3.13: The correlation of the 12 μm intensity between spectra obtained in this work and prediction by the DIRBE zodi-model.

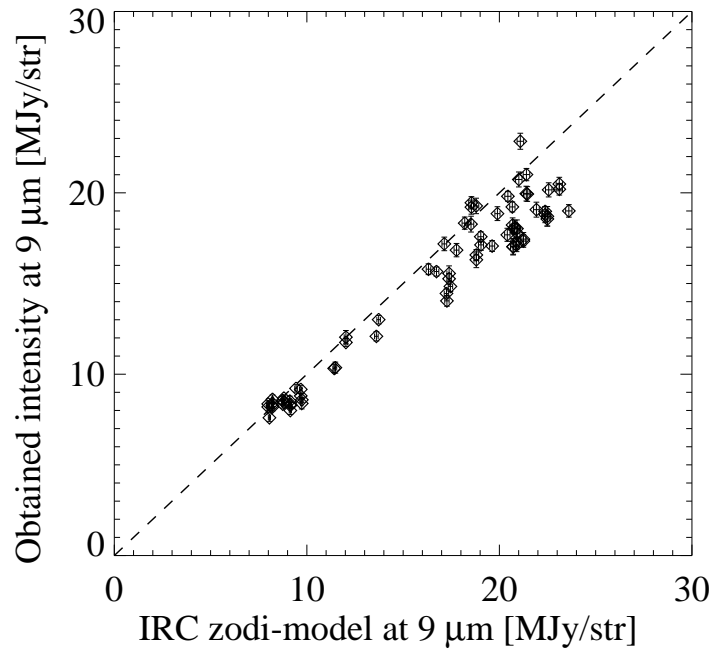


Figure 3.14: The correlation of the 9 μm intensity between spectra obtained in this work and prediction by the IRC zodi-model.

Chapter 4

Grain properties

4.1 Detection of emission features

I found the presence of the emission features around $10 \mu\text{m}$ in spectra at all pointing directions. To investigate detailed feature shapes, I divide these observed spectra by their each continuum spectrum and derived observed/continuum spectra at each direction. At first, I assume a diluted blackbody function as a continuum, for the most simple consideration. Secondly, I estimate continuum spectra on the basis of the DIRBE zodi-model.

4.1.1 Continuum estimation based on a diluted blackbody function

As a continuum spectra, I fitted a diluted blackbody function of single temperature to each spectra. The function is written by the following:

$$C_{\lambda, BB} = \tau B_{\lambda}(T) , \quad (4.1)$$

where $B_{\lambda}(T)$ is the Plank function and τ and T mean an optical depth and a particle temperature typical in the line of sight, respectively. These two parameters were optimized by fitting to each spectra as constants. For the fitting, I used the SG2 data in the $7.7\text{--}8.0 \mu\text{m}$ range and the $12.0\text{--}12.3 \mu\text{m}$ range, which seems not to be contaminated by any spectral features.

Best-fit values of τ and T are shown in Figure 4.1 as functions of the ecliptic latitude. The IPD distributes globally with a peak near the ecliptic plane, which is consistent with the past observations (Hauser et al. 1984). Since the lines of sight at lower ecliptic latitudes include more IPD far from the Sun, best-fit temperatures become lower near the ecliptic plane than those at the

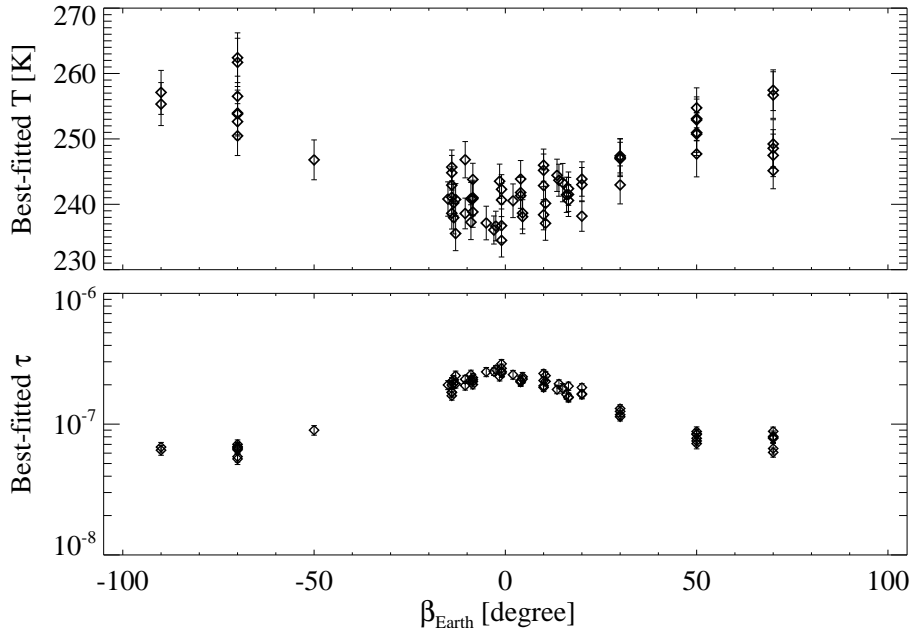


Figure 4.1: Best-fit parameters for continuum fitting by a diluted blackbody function. Top: Best-fit temperature (T), Bottom: Best-fit optical depth (τ).

ecliptic poles.

I divided a spectrum at each direction by the best-fit continuum and obtained an observed/continuum spectrum. It should be noted that this continuum is characterized with a single temperature for IPD particles included in each line of sight. In actual case, however, IPD particles have different temperatures depending on the distance from the Sun, the size, and the composition. It means that this estimation of continua was too simple.

4.1.2 Continuum estimation based on the DIRBE zodi-model

In order to consider the multiple temperature distribution of IPD particles, I referred to the DIRBE zodi-model (Kelsall et al. 1998). In the mid-infrared wavelength region, the intensity of the zodiacal emission is written as

$$Z_{\lambda}(\lambda_{\oplus}, \beta_{\oplus}, t) = \sum_{c=1}^3 \int n_c(\lambda_{\oplus}, \beta_{\oplus}, s, t) E_{c,\lambda} B_{\lambda}(T(\lambda_{\oplus}, \beta_{\oplus}, s, t)) ds, \quad (4.2)$$

where the subscription c denotes the types of the IPD components: smooth cloud ($c = 1$), dust bands ($c = 2$) and circumsolar ring with trailing blob ($c = 3$). n_c is the spatial distribution of the cross section for each component as shown in Figure 1.2. Positions in the Solar System are defined by the geocentric ecliptic coordinates $(\lambda_{\oplus}, \beta_{\oplus})$ and the distance from the Earth, s , and the

observation date, t , which can be converted to the rectangular coordinates around the Sun. $E_{c,\lambda}$ is the emissivity modification factor, which is a function of the wavelength, corresponding to the deviations from the blackbody function $B_\lambda(T)$. T means the temperature at each position. In Kelsall et al. (1998), the spatial distributions of T were determined in conjunction with n_c .

Using the results and setting $E_{c,\lambda}$ to unity, I calculated the continuum spectrum. Absolute intensities, however, included uncertainty as described in Figure 3.13. Therefore, I scaled the calculated continuum so that the continuum intensity matches the observed intensity at $12 \mu\text{m}$ for derivation of the observed/continuum spectrum normalized at $12 \mu\text{m}$. If the scaling ratio is denoted by α , the continuum C_λ is expressed as

$$C_\lambda(\lambda_\oplus, \beta_\oplus, t) = \alpha \times \sum_{c=1}^3 \int n_c(\lambda_\oplus, \beta_\oplus, s, t) B_\lambda(T(\lambda_\oplus, \beta_\oplus, s, t)) ds . \quad (4.3)$$

The values of α was typically in the range from 1.0 to 1.1.

I divided all observed spectra by each continuum and, at last, obtained the observed/continuum spectra of the zodiacal emission at 74 pointing directions. I showed all of the derived observed/continuum spectra in Appendix 1. For the confirmation of the robustness, I also calculated the continua on the basis of the IRC zodi-model (Kondo et al. 2016) and derived the observed/continuum spectra. There were no detectable change because these models have significant differences only in absolute intensities and this difference is canceled by the normalization by α in equation (4.3). Hereafter, I investigate the wavelength-dependence of observed/continuum ratios, i.e., the shape of spectral features. Although the shape has diversity, the excess emission and even some sharp emission peaks can be clearly seen beyond the error range in all of their spectra. Such detailed shapes have been revealed for the first time thanks to the high sensitivity of the IRC and the accurate subtractions of the instrumental artifacts.

4.1.3 Comparison with previous works

I compared an observed/continuum spectrum obtained in this work with that of a previous work. Figure 4.2 shows the comparison with the result of IRTS/MIRS observations (Ootsubo et al. 1998). As the data of this work, I selected the observed/continuum spectrum at the direction close to that IRTS/MIRS observed. Since the IRTS/MIRS data cannot cover the wavelength at the longer edge of the excess emission, it is difficult to estimate the appropriate continuum and this uncertainty results in the incorrect absolute value of the observed/continuum ratio. In contrast, the AKARI data enables us to derive the suitable continuum by scaling the predictions of the DIRBE zodi-model

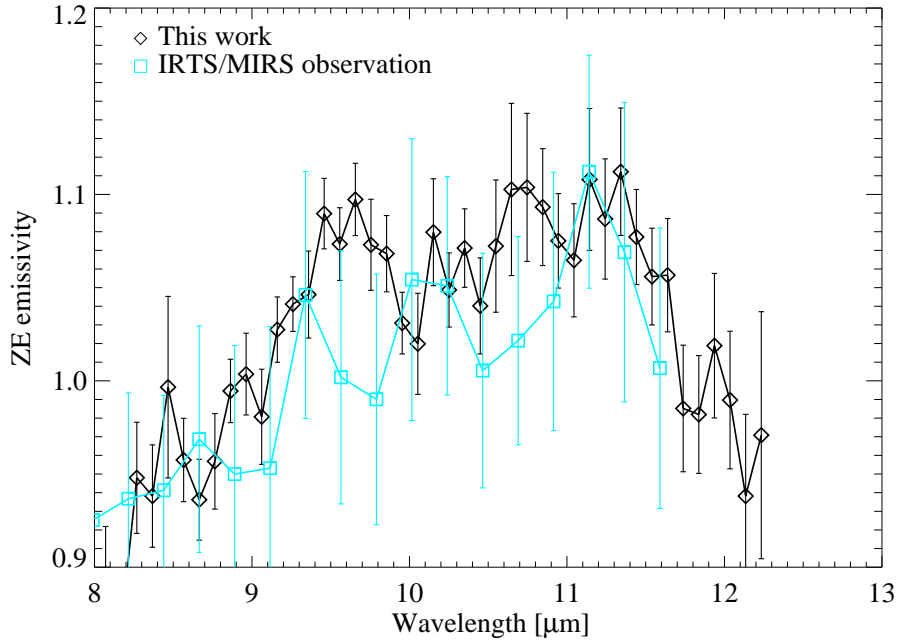


Figure 4.2: Comparison of the observed/continuum spectrum with IRTS/MIRS observations (Ootsubo et al. 1998). Blue squares were obtained from the IRTS/MIRS observations of about $3^\circ \times 3^\circ$ sky region at $(\lambda_\oplus, \beta_\oplus) \sim (125^\circ, 0^\circ)$ at a solar elongation of 97° . On the other hand, I plotted the data obtained in this work at the direction of $(\lambda_\oplus, \beta_\oplus) = (159^\circ.5, 2^\circ)$ with a solar elongation of $90^\circ \pm 1^\circ$ as black diamonds.

at $12 \mu\text{m}$. For the equal comparison, therefore, I scaled the absolute value of the IRTS/MIRS data so that the max value becomes identical to that of the AKARI data.

Ootsubo et al. (1998) presented three emission peaks as well as this work. Although the peak wavelengths and the relative strength of their peaks seem to be different from this work, the error range in Ootsubo et al. (1998) is too large to discuss the differences.

In Appendix 2, I compare the averaged spectra also with the spectra of various other objects: collected dust particles, collected meteorites, asteroids and cometary dust coma.

4.2 Absorption coefficients of candidate minerals

To link the shapes of emission features to grain properties of the IPD included in the line of sight, I introduced a mineralogical point of view. The observed/continuum spectra I derived are written as the following using equation (4.2) and (4.3):

$$\frac{Z_\lambda}{C_\lambda} = \frac{1}{\alpha} \times \frac{\sum_{c=1}^3 \int n_c E_{c,\lambda} B_\lambda(T) ds}{\sum_{c=1}^3 \int n_c B_\lambda(T) ds}. \quad (4.4)$$

It means the observed/continuum ratio corresponds to $E_{c,\lambda}$ averaged in each line of sight and normalized at $12\ \mu\text{m}$ through the scaling factor α . $E_{c,\lambda}$ can be thought to be equivalent to the absorption coefficient, Q_{abs} , for the same dust component and at the same wavelength. Therefore, the shape of the observed/continuum spectra is determined by Q_{abs} spectra of constituent materials of the IPD grains included in the line of sight. In order to identify the grain properties of the IPD, I compare the obtained observed/continuum spectra with absorption coefficients of candidate minerals from the below.

In this thesis, I assumed 4 types of silicates as candidates: amorphous with olivine composition, amorphous with pyroxene composition, forsterite (Mg_2SiO_4 , one of olivine crystals), and ortho-enstatite (MgSiO_3 , one of pyroxene crystals). The solid solutions of the two amorphous minerals are assumed as $\text{Mg}/(\text{Mg}+\text{Fe})=0.5$. I confirmed that ortho- and clino-enstatite has similar wavelength-dependence of Q_{abs} , although the absolute values are slightly different. Previous laboratory measurements of the IPD samples collected in the stratosphere or on the ground have found that these minerals are main constituents (see section 1.2.1 for details). In addition, these types of minerals have vibration modes around $10\ \mu\text{m}$. I calculated the absorption coefficients from their optical constants on the basis of the Mie theory (Bohren & Huffman 1983; Kerker 1969), assuming the spherical grains with the size variation from $0.1\ \mu\text{m}$ to $100\ \mu\text{m}$. Figure 4.3 indicates the results. I also plotted mass absorption coefficients (MACs) of two types of crystal measured in laboratories (Koike et al. 2003; Chihara et al. 2002). The MACs were measured on crystalline dust samples with the size range of $\sim 0.1\text{--}10\ \mu\text{m}$. Those samples are thought to have a shape probability distribution of the continuous distribution of ellipsoids (CDE), which includes ellipsoidal grains with all possible aspect ratios in directions of the crystal axes in equal probabilities.

The zodiacal emission is a superposition of emission from grains of many sizes (at different temperatures) as well as grains at many positions (also at different temperatures). Assuming the size distribution investigated by dust detectors on board space probes (see section 1.1.3), larger grains ($10\text{--}100\ \mu\text{m}$) mainly contribute to the absolute intensity level of the zodiacal emission (Reach et al. 2003). They have absorption coefficients nearly constant around unity and, therefore, make an emission baseline of the blackbody. In addition to the baseline, small grains ($\leq 1\ \mu\text{m}$) can cause excess emission around specific wavelength corresponding to the vibration modes. It indicates that this study on the shape of excess emission features reveals, in particular, the properties of small grains in the IPD.

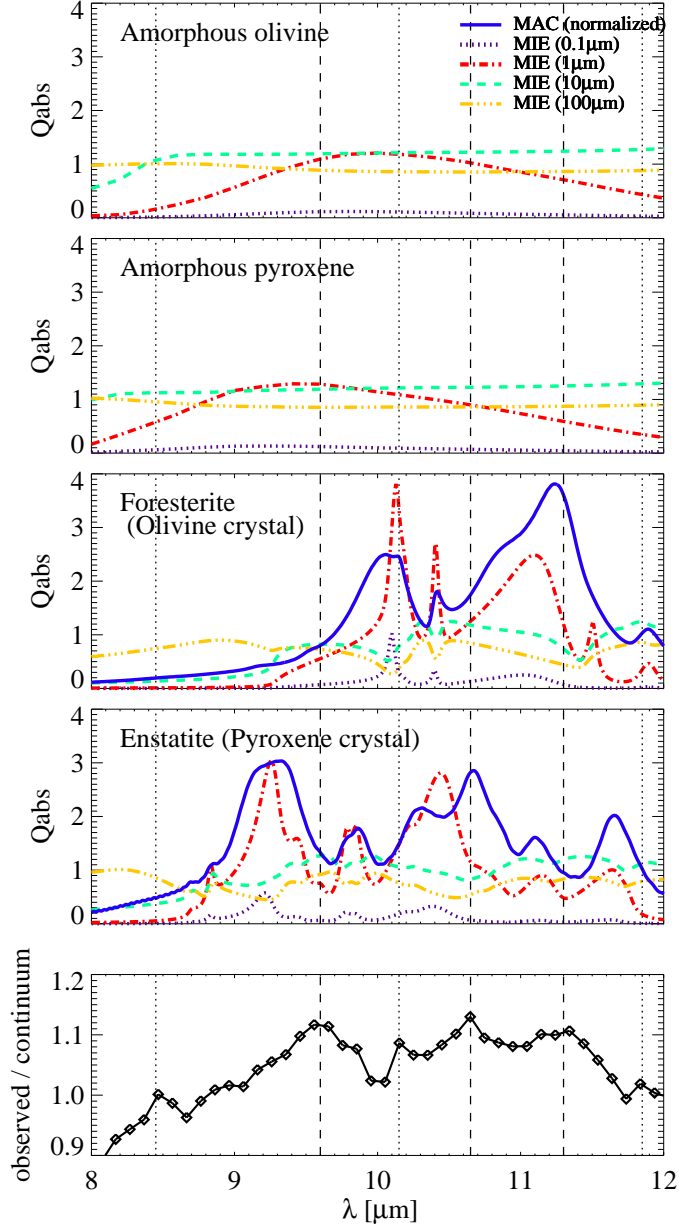


Figure 4.3: Comparison with the absorption coefficients of candidate minerals: amorphous with olivine composition, amorphous with pyroxene composition, forsterite (Mg_2SiO_4 , one of olivine crystals), and ortho-enstatite (MgSiO_3 , one of pyroxene crystals), from the top. The most bottom panel shows the observed/continuum spectrum of the zodiacal emission averaged in all directions, for comparison. I assumed the solid solution of $\text{Mg}/(\text{Mg}+\text{Fe})=0.5$ for two amorphous minerals. These absorption coefficients are calculated from their optical constants or dielectric functions on the basis of the Mie theory assuming the grain size of 0.1, 1, 10, and 100 μm . We referred the optical constants of two amorphous minerals to Dorschner et al. (1995), and the dielectric functions of forsterite and enstatite to Sogawa et al. (2006) and private communications with Dr. H. Chihara at Osaka Sangyo University, respectively. Blue solid lines in the middle two panels indicate mass absorption coefficients (MACs) measured in laboratories (Koike et al. 2003; Chihara et al. 2002). They are normalized to the max value of Q_{abs} calculated by the Mie theory assuming 1 μm -sized grains.

4.3 Interpretation of the averaged observed/continuum spectrum

First of all, I compared the observed/continuum spectrum averaged in all directions with Q_{abs} spectra of candidate minerals. This enables us to understand grain properties typical in all over the sky. These typical properties represent the grain properties of the IPD from the JFCs, because the IPD from the JFCs (i.e., the smooth cloud) is the significantly largest fraction of the total IPD anywhere in the all sky (see section 1.1.2 for details).

In the averaged spectra shown in the bottom panel of Figure 4.3, I found three main peaks around 9.60, 10.65, and 11.30 μm with sub-peaks around 8.45, 10.15, and 11.85 μm . Such sharp peaks can be caused only by small grains ($\leq 1 \mu\text{m}$) of crystalline silicates. We can say that the IPD from the JFCs includes some fractions of small grains of crystalline silicates. In particular, main peaks around 9.60 and 10.65 μm can be caused by enstatite, while sub-peaks around 10.15 and 11.85 μm are mainly contributed by forsterite. Around 11.30 μm , both forsterite and enstatite show peaks. Since peaks originating from enstatite were more significant than that from forsterite, the IPD from the JFCs was found to be typically enstatite-rich.

Sub-peak at 8.45 μm can be thought to originate from materials other than those shown in Figure 4.3. I mention some possibilities for the candidate materials. As one of the unidentified infrared (UIR) emission bands, a peak around 8.6 μm is known (Willner 1984). The source candidates are polycyclic aromatic hydrocarbons (PAHs; Leger & Puget 1984; Allamandola et al. 1985), quenched carbonaceous composite (QCC; Sakata et al. 1984, 1987), and hydrogenated amorphous carbons (HAC; Borghesi et al. 1987), which are carbonaceous and dominated by aromatic bonds. In a mid-infrared spectrum of the dust coma ejected from a short period comet, the peak at 8.6 μm was detected in the combination with a peak at 8.25 μm (Harker et al. 2007), which is also expected as a PAH feature. The sub-peak at 8.45 μm seen in the zodiacal emission spectra may be contributed by such materials, although the wavelength position is slightly different.

I have to note that the wavelength position of the enstatite peak around 9.2 μm needs to be shifted to around 9.6 μm , in order to reproduce the observed/continuum spectrum. Several reasons can cause such wavelength shift of the peak. I enumerate the reasons in the following.

Replacing Mg-ions with Fe ions : Replacing Mg-ions with Fe-ions is a possible reason to shift a peak to a longer wavelength, although the trend is slightly different at different peaks (Koike et al. 2003; Chihara et al. 2002). Using the experimental results of the MACs in Chihara et al. (2002), I

plot the wavelengths of a peak around $9.2 \mu\text{m}$ in various solid solutions of enstatite as the panel (a) in Figure 4.4. The wavelength position becomes longer as $\text{Fe}/(\text{Mg}+\text{Fe})$ ratio increases. Ferrosillite (FeSiO_3) shows the peak at $9.54 \mu\text{m}$, which is close to the observed peak position.

Coating by organic materials : Grains coated by organic materials also can show peaks at shifted wavelength positions (Kimura 2013). This effect can be caused at the peaks in which the real part of the dielectric function shows a negative valley (Bohren & Huffman 1983), like the enstatite peak around $9.2 \mu\text{m}$ (see Figure 4.5). I assumed grains with a carbon-matrix and spherical enstatite-inclusions. I calculated the dielectric function of the mixture following the Maxwell-Garnett law (Bohren & Huffman 1983; Genzel & Martin 1973; Barker 1973; Bohren & Wickramasinghe 1977) and derived a Q_{abs} spectrum from such composite dielectric functions using Mie theory (Bohren & Huffman 1983; Kerker 1969). Changing the fraction of the inclusions, I investigated the shift of the peak wavelengths. The result is shown in the panel (b) of Figure 4.4. Carbon mantle certainly shifts the peak wavelength up to $9.28 \mu\text{m}$, although it is not sufficient to explain the observed peak wavelength.

Increase of porosity : Similarly, the wavelength position of the peak depends on grain porosity. I assumed a porous grain as an enstatite-matrix with spherical vacuum-inclusions. Calculation of the Q_{abs} spectrum was performed in the same way as the case of grains coated by carbon. The peak wavelength is shifted to longer side by increasing the porosity like the panel (c) in Figure 4.4. An extremely porous grain seems to show the peak at $9.33 \mu\text{m}$.

Elongation along the crystal axis : Other possibility is the effect of crystal morphologies. Ortho-enstatite is orthorhombic crystal and each crystal axis (a, b, c) has the individual dielectric function (see Figure 4.5). If we consider an ellipsoidal grain, the Q_{abs} spectrum is determined by the dielectric functions of each crystal axis and the aspect ratio in directions of the crystal axes, assuming the surface mode in the Lorentz model (Bohren & Huffman 1983; Takigawa & Tachibana 2012). Therefore, wavelength positions of some peaks can be shifted depending on the aspect ratio (Takigawa & Tachibana 2012). This effect also can be caused at the peaks in which the real part of the dielectric function shows a negative valley (Bohren & Huffman 1983). An example of enstatite grains elongated along a-axis (the stacking direction of the layer of tetrahedra chains) is shown in the panel (d) of Figure 4.4. I calculated the Q_{abs} spectra of such ellipsoidal grains on the basis of the Lorentz model. Grain lengths along b- and c-axis were fixed to $1 \mu\text{m}$ and the length along a-axis was changed from $0.1 \mu\text{m}$ to $100 \mu\text{m}$. As shown in Figure 4.4, the peak position of a

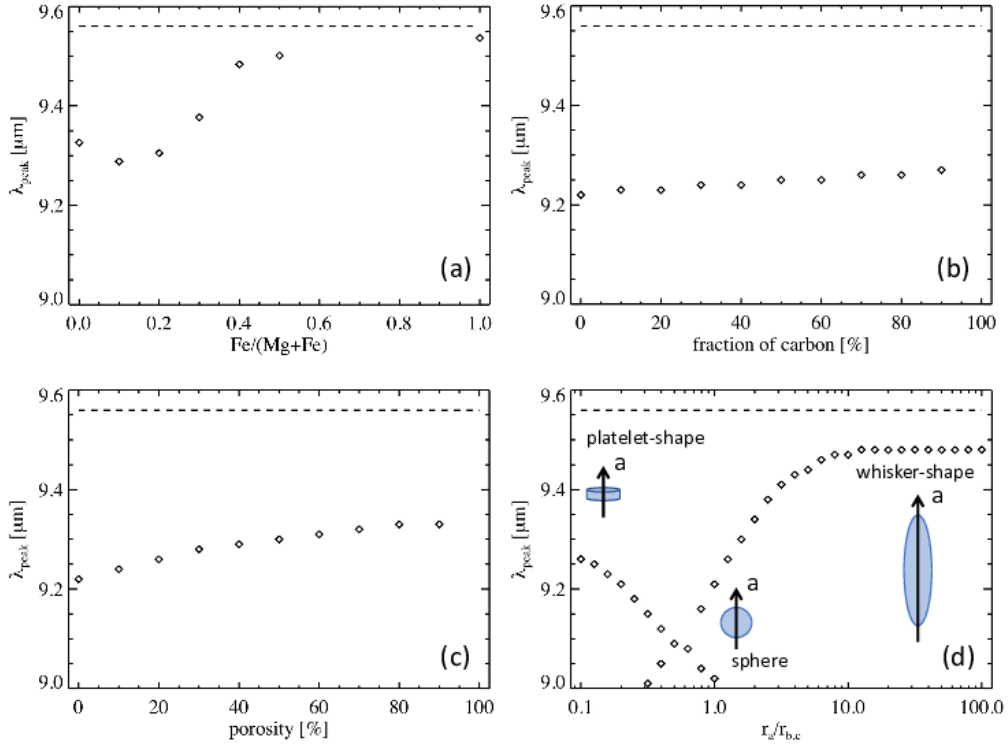


Figure 4.4: The wavelength shift in a peak around $9.2 \mu\text{m}$ due to (a) Replacing Mg-ions with Fe ions, (b) coating by carbon, (c) increase in porosity, and (d) elongation along the crystal a-axis. λ_{peak} means the peak wavelength and dotted lines at $\lambda_{peak} = 9.56 \mu\text{m}$ indicate the peak position in the zodiacal emission spectra. The values in the panel (a) was extracted from MACs of solid solutions, which were measured for samples in the size range of $0.1\text{--}10 \mu\text{m}$. In the calculation for the panel (b) and (c), I assumed the grain size to $1 \mu\text{m}$. For the estimation in the panel (d), grain lengths along b- and c-axis ($r_{b,c}$) were fixed to $1 \mu\text{m}$ and the length along a-axis (r_a) was changed from $0.1 \mu\text{m}$ to $100 \mu\text{m}$.

grain elongated along a-axis was found to be asymptotic to $9.48 \mu\text{m}$.

Every effect is not sufficient to shift the peak wavelength to reproduce the observed peak position alone. It means the wavelength shift may be attributed to the combination of several effects. These effects are conceivable well because they are also seen in the results of laboratory measurements of the collected IPD (see section 1.2.1 for details). A lot of the collected IPD samples were found to be porous and/or carbonaceous (Messenger et al. 2013). Many whisker- or platelet-shaped crystals have also actually found in those samples (Bradley et al. 1983).

In addition, I found the suppression of an enstatite peak at $11.6 \mu\text{m}$ by comparison between zodiacal emission spectra and the Q_{abs} spectra of enstatite. According to Figure 4.5, the optical constants of a- and b-axis are flat at longer than $11.5 \mu\text{m}$, although c-axis have a significant peak in such wavelength range (Demichelis et al. 2012). The suppression implies that the grain length along

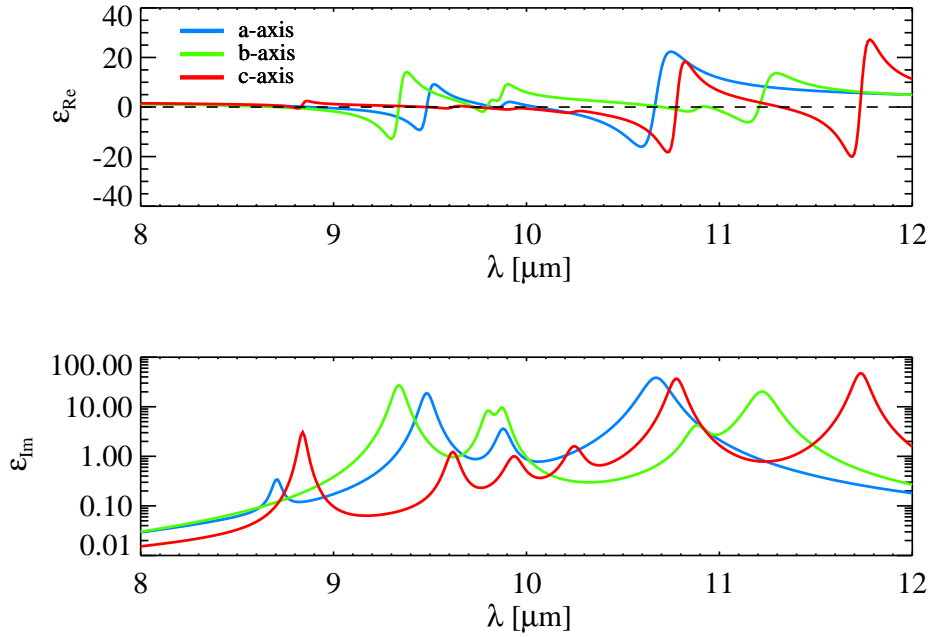


Figure 4.5: Dielectric function of orthorhombic-enstatite. The top panel and the bottom panel show the real part and the imaginary part, respectively. c-axis is parallel to the direction of tetrahedra chains and a-axis corresponds to the stacking direction of the layer of tetrahedra chains.

c-axis (the direction of tetrahedra chains) may be reduced, like platelet-shaped enstatite which is symmetric around the c-axis, or whisker-shaped enstatite which is elongated along a- or b-axis.

4.4 Variations due to the origin difference

As described in section 1.1.2, the IPD originating from different types of parent bodies has different spatial distributions. Although the IPD from the JFCs occupies the largest fraction in all lines of sight, the fraction of the asteroidal IPD and the IPD from the OCCs becomes relatively large in directions toward the asteroidal dust bands and in directions at high ecliptic latitudes, respectively. In lines of sight toward such directions, differences of grain properties may change the feature shapes. In this section, I compare the feature shapes among different pointing directions, for the comparison of grain properties among the IPD originating from different types of parent bodies.

To investigate the influence of the asteroidal IPD on feature shapes, I compared feature shapes among directions with different brightness contributions of the asteroidal dust bands. The contribution level was denoted by A and calculated on the basis of the IPD spatial distribution in the DIRBE zodi-model. The model predicted the spatial distribution of the asteroidal IPD component

forming three dust band structures (see section 1.1.2 for details). For each observed lines of sight, I calculated the continuum intensity at $12 \mu\text{m}$ originating from the component, and defined A as the proportion to the continuum intensity at $12 \mu\text{m}$ originating from all the components. This is described as

$$A = \frac{\int n_2 B_{12\mu\text{m}}(T) ds}{\sum_{c=1}^3 \int n_c B_{12\mu\text{m}}(T) ds} \times 100 \quad [\%], \quad (4.5)$$

where definitions of all variables are same as equation (4.2) and the component represented by $c = 2$ corresponds to the asteroidal dust bands.

On the other hand, the contribution of the IPD from the OCCs could not be calculated quantitatively because of the lack of an accurate model prediction of the spatial distribution including the isotropic component composed of the IPD from the OCCs. Instead, I compared feature shapes among directions with different absolute values of ecliptic latitudes, $|\beta_{\oplus}|$, in order to investigate the influence of the IPD from the OCCs.

Figure 4.6 is the two-dimensional histogram of A and $|\beta_{\oplus}|$ in all observed directions. It is clear that directions with $A < 1 \%$ distribute in a wide range of ecliptic latitudes, while directions with $A \geq 1 \%$ are concentrated at low $|\beta_{\oplus}|$ (i.e., near the ecliptic plane). The dataset at the directions with $|\beta_{\oplus}| < 20^\circ$ was divided into 5 A -bins: $0.0 \leq A < 1.0$, $1.0 \leq A < 1.5$, $1.5 \leq A < 2.0$, $2.0 \leq A < 4.0$, and $4.0 \leq A < 6.0$ in percent. The observed/continuum spectra averaged in each A -bin are presented in Figure 4.7 and I compare the feature shapes among them. Similarly, the dataset at the directions with $A < 1 \%$ was divided into 4 $|\beta_{\oplus}|$ -bins: $0 \leq |\beta_{\oplus}| < 25$, $25 \leq |\beta_{\oplus}| < 40$, $40 \leq |\beta_{\oplus}| < 60$, and $60 \leq |\beta_{\oplus}| < 80$ in degree, excepting the data at $|\beta_{\oplus}| = 90^\circ$ because of the too less data number. Figure 4.8 shows the observed/continuum spectra averaged in each $|\beta_{\oplus}|$ -bin and I investigate the feature shape differences.

For quantitative estimations of feature shapes, I defined 4 parameters: the equivalent width of the whole excess emission (EW_{whole}), the equivalent width ratio in $10.0\text{--}10.5 \mu\text{m}$ and $9.0\text{--}9.5 \mu\text{m}$ ($EW_{10.0\text{--}10.5}/EW_{9.0\text{--}9.5}$), a wavelength shift of a peak excess due to crystalline silicates ($\Delta\lambda_{\text{peak}}$), and the equivalent width ratio of peak excesses due to crystalline silicates ($EW_{\text{fo}}/EW_{\text{en}}$). I describe the definition of each parameter and their resultant dependences on A and β_{\oplus} hereafter.

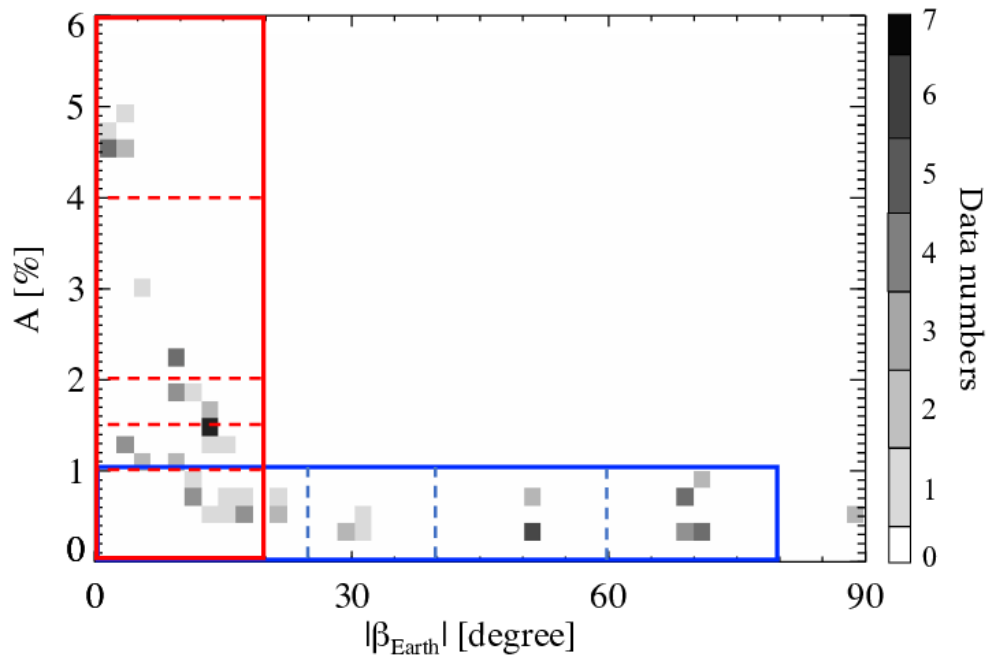


Figure 4.6: The two-dimensional histogram of the brightness contribution from the dust bands (A) and absolute values of ecliptic latitudes ($|\beta_{\oplus}|$) at the pointing directions. I compared the feature shapes among A in the datasets with $|\beta_{\oplus}| < 20^\circ$ surrounded by the red line, and investigated the dependence of the feature shapes on $|\beta_{\oplus}|$ in the datasets with $A < 1\%$ surrounded by the blue line. Dotted lines indicate the border of the bins used for the averaging. I did not use the data at $|\beta_{\oplus}| = 90^\circ$ because of the too less data number.

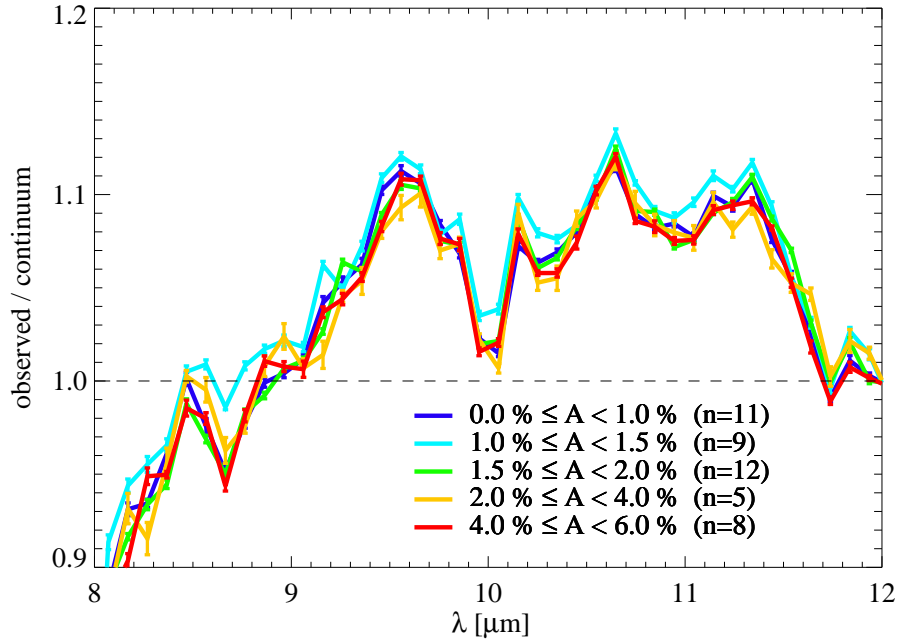


Figure 4.7: The observed/continuum spectra averaged in each A -bin. The error bars indicate the standard errors in the averaging. I showed the data number (n) in each bin at the legend.

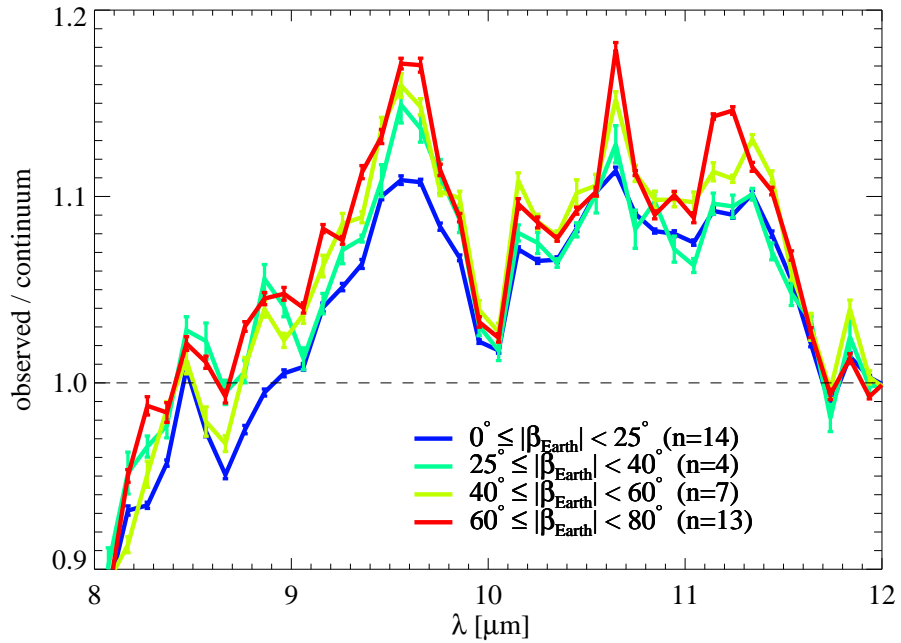


Figure 4.8: The observed/continuum spectra averaged in each $|\beta_{\oplus}|$ -bin. The error bars indicate the standard errors in the averaging. I showed the data number (n) in each bin at the legend.

4.4.1 Equivalent width of the whole excess emission : EW_{whole}

The first parameter for evaluation of feature shapes is the equivalent width of the whole excess emission in 8–12 μm , defined by the equation:

$$EW_{\text{whole}} = \int_{8\mu\text{m}}^{12\mu\text{m}} \frac{Z_{\lambda} - C_{\lambda}}{C_{\lambda}} d\lambda \quad [\mu\text{m}] . \quad (4.6)$$

Z_{λ} and C_{λ} are zodiacal emission spectra given by equation (4.2) and the continuum spectra given by equation (4.3), respectively. This represents the excess strength in the 8–12 μm range. I calculated it for the observed/continuum spectra averaged in each bin and showed the dependence on A and $|\beta_{\oplus}|$ in Figure 4.9.

While EW_{whole} seems to have the trend of a negative correlation with A , it has a clear positive correlation with $|\beta_{\oplus}|$. This indicates that the IPD at higher A and $|\beta_{\oplus}|$ show a weaker and stronger excess emission in the 8–12 μm range, respectively. The derived excess strengths and the $|\beta_{\oplus}|$ -dependence was roughly consistent with the previous study of excess strengths at some β_{\oplus} and solar elongations in Reach et al. (2003).

The variation of EW_{whole} can be interpreted by the difference of the IPD grain size distribution among lines of sight at different directions. Since small grains around 1 μm size strongly emit the excess peaks like Figure 4.3, an increase in the fraction of such small grains strengthens all peaks evenly, resulting in the increase in the whole excess strength. If we assume a single size of grain, the value of EW_{whole} is expected to become like Figure 4.10. The more fraction of small grains clearly results in the more excess strength, although it should be noted that the baseline emission and the excess emission originate from grains with different size in actual case.

The negative A -dependence of EW_{whole} means the fraction of large grains relatively increases at directions toward the dust bands, which shows the asteroidal IPD may have a size distribution biased to larger grains. It can be thought that the dust continuously supplied by the collisional cascades of asteroids includes many large grains in the middle of the cascades, while the cometary IPD is ejected from melting icy mantles mainly as small grains (Shinnaka et al. 2018). Thus, the difference of the supply processes could cause different size distributions.

On the other hand, the positive $|\beta_{\oplus}|$ -dependence of EW_{whole} means that lines of sight at higher $|\beta_{\oplus}|$ include more fraction of small grains. It can be explained by a radial dependence of the grain size distribution. As mentioned in section 1.1.3, the IPD at 1 au from the Sun has more fraction of small grains than the IPD at a few au, by the collisional cascade during the accretion of IPD particles toward the Sun due to PR drag (Grün et al. 1985; Jehn 2000). Since the IPD distributes

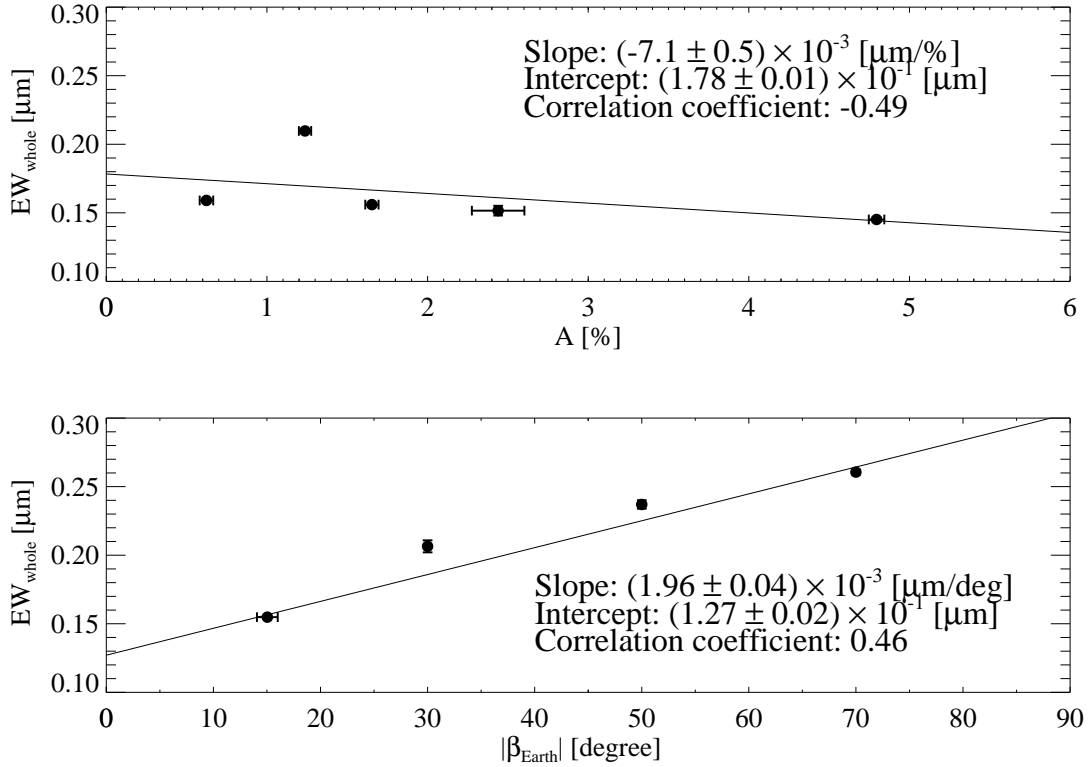


Figure 4.9: The dependence of the equivalent width of the whole excess emission (EW_{whole}) on the brightness contribution from the dust bands (A ; the top panel) and the ecliptic latitude ($|\beta_{\oplus}|$; the bottom panel). Each filled circle is calculated from the observed/continuum spectrum averaged in each bin shown in Figure 4.7 and 4.8. The position in the horizontal axis corresponds to the mean value in the bin. The solid lines are the linear functions that best fit the dependence, and the results of the fits are summarized in Table 4.1. I also show the value of correlation coefficient as a reference.

on the ecliptic plane convergently, the lines of sight toward the ecliptic poles can see through only the IPD existing near 1 au, while the IPD in orbits far from the Sun comes in the lines of sight when we observe a sky region at low $|\beta_{\oplus}|$ with the solar elongation of 90° . Therefore, the fraction of small grains could relatively increase in a line of sight at higher $|\beta_{\oplus}|$. In this case, the $|\beta_{\oplus}|$ -dependence can be interpreted by the dynamical process of the IPD particles after the liberation from the parent bodies, not by the different grain properties between the IPD from the JFCs and the OCCs.

4.4.2 Equivalent width ratio in 10.0–10.5 μm and 9.0–9.5 μm : $EW_{10.0-10.5}/EW_{9.0-9.5}$

For the investigation of grain properties which is hard to be influenced by the dynamical process after the liberation, I focused on parameters of feature shape related to the mineral composition. According to Figure 4.3, amorphous olivine and amorphous pyroxene can cause the smooth convex excess around 10 μm and in 9 μm -band, respectively. As a tentative indicator of

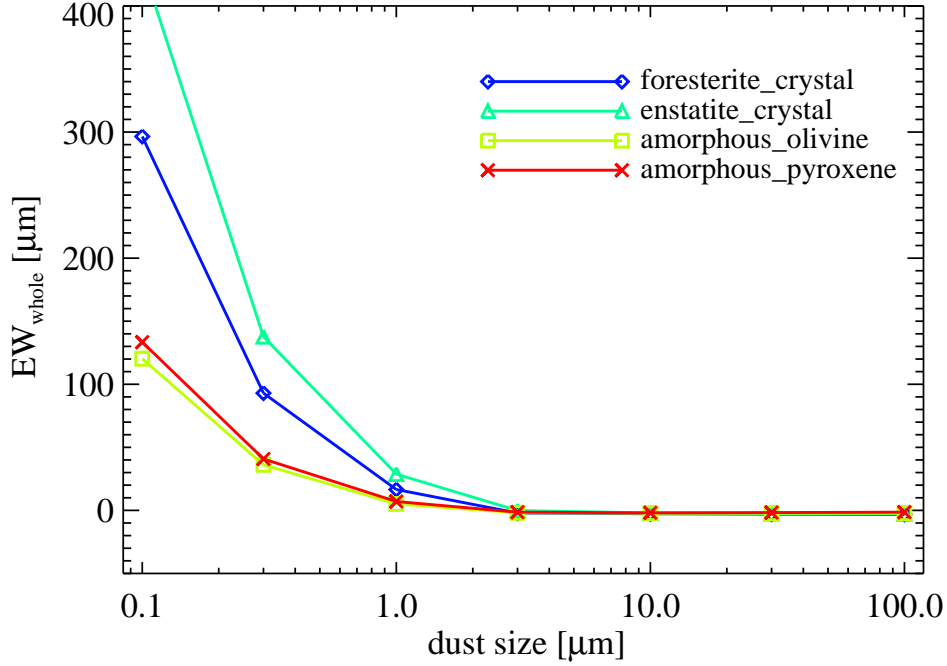


Figure 4.10: Relation between the equivalent width of the whole excess emission (EW_{whole}) and the grain size, assuming a single size.

(olivine)/(olivine+pyroxene) ratio in amorphous grains, therefore, I define the ratio of the equivalent widths in two wavelength regions, 10.0–10.5 μm and 9.0–9.5 μm :

$$EW_{10.0-10.5}/EW_{9.0-9.5} = \int_{10.0\mu\text{m}}^{10.5\mu\text{m}} \frac{Z_\lambda - C_\lambda}{C_\lambda} d\lambda / \int_{9.0\mu\text{m}}^{9.5\mu\text{m}} \frac{Z_\lambda - C_\lambda}{C_\lambda} d\lambda . \quad (4.7)$$

The wavelength regions were selected so that they avoid the contamination by the peak from crystalline silicates as possible. The resultant correlation with A and $|\beta_\oplus|$ was shown in Figure 4.11. The ratio $EW_{10.0-10.5}/EW_{9.0-9.5}$ shows a positive and negative correlation with A and $|\beta_\oplus|$, respectively.

Regarding the A -dependence, the indicator of $EW_{10.0-10.5}/EW_{9.0-9.5}$ may be contributed by other silicate minerals, in addition to olivine and pyroxene, which I originally thought as the origins. If so, the indicator does not reflect the (olivine)/(olivine+pyroxene) ratio in amorphous grains. As mentioned in section 1.2.1, it is known that hydration is a unique property of the asteroidal IPD. One of the common hydrated minerals is phyllosilicate like serpentine and talc, which are produced by the aqueous alteration from forsterite or enstatite (Ganguly & Bose 1995; Bischoff 1998; Tomeoka et al. 1989). They show a smooth excess feature with a peak around 10 μm , similar to that of amorphous olivine (Beck et al. 2014). I suggest a possibility that phyllosilicate feature

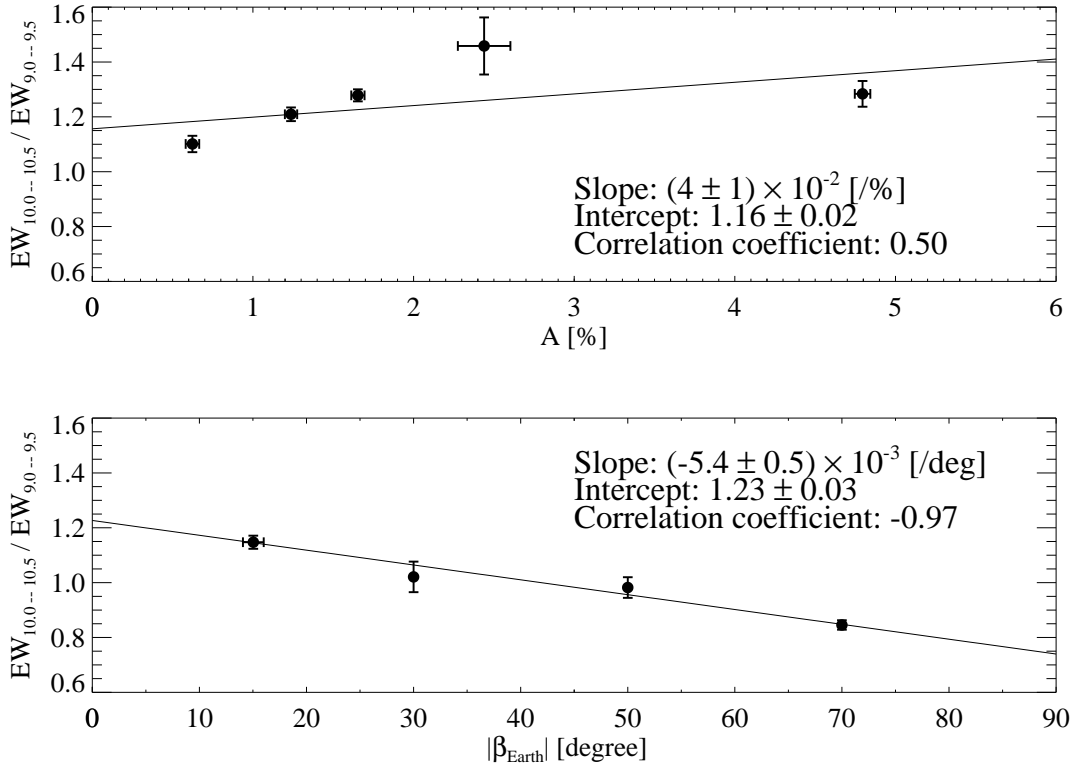


Figure 4.11: The dependence of the equivalent width ratio in 10.0–10.5 μm and 9.0–9.5 μm ($EW_{10.0-10.5}/EW_{9.0-9.5}$) on the brightness contribution from the dust bands (A ; the top panel) and the ecliptic latitude ($|\beta_{\oplus}|$; the bottom panel). Other explanations are same as Figure 4.9.

raises $EW_{10.0-10.5}/EW_{9.0-9.5}$ at directions with high A in Figure 4.11 without an increase in the fraction of amorphous olivine. Since the most significant dust band at $\beta_{\oplus} = \pm 9.3^\circ$ (Kelsall et al. 1998) is thought to be formed by the IPD from the C-type Veritas family (Nesvorný et al. 2003), this scenario is consistent with the result of the previous works which found the hydration in most C-complex asteroids (Usui et al. 2018) or CM chondrites (McSween 1979, 1987), which is a type of carbonaceous meteorites associated with C-type asteroids.

On the other hand, the derived negative correlation between $EW_{10.0-10.5}/EW_{9.0-9.5}$ and $|\beta_{\oplus}|$ indicates straightforwardly that the IPD has the lower olivine/(olivine+pyroxene) ratio at the higher $|\beta_{\oplus}|$. It can be thought that the IPD from the OCCs has lower olivine/(olivine+pyroxene) ratio than the IPD from the JFCs regarding amorphous grains.

4.4.3 Wavelength shift of a peak excess due to crystalline silicates : $\Delta\lambda_{\text{peak}}$

In the AKARI spectra, several sharp peaks due to crystalline silicates can be clearly seen for the first time thanks to the high signal-to-noise ratio. For the next step, I focus on such more details of feature shapes. As quantitative measures of each peak excess due to crystalline silicates, I investigated the wavelength shifts and the equivalent width ratios of peak excesses due to crystalline silicates: forsterite and enstatite.

In order to compare such parameters among peaks from the same vibration modes at different directions, I need at first to identify which peaks originate from the same vibration mode. Therefore, I fixed a reference wavelength (λ_{ref}) for each main peak commonly to all the directions and assumed that the peaks seen within the neighboring two wavelength-bins around the λ_{ref} (corresponding roughly to the region of $\lambda_{\text{ref}} \pm 0.25 \mu\text{m}$) originate from the same vibration mode. The procedures to fix the λ_{ref} are like the following.

1. For observed/continuum spectra at all 74 directions, I searched wavelength-bins with a peak which has a higher observed/continuum ratio than the neighboring bins.
2. For all wavelength-bins from 8 to 12 μm , I counted numbers of the data that have a peak at the bin. The histogram is shown in Figure 4.12.
3. I selected wavelength-bins that have a mode of the histogram over the five successive bins around it, and the center wavelengths of the selected bins were defined as λ_{ref} . Around 9.6 μm , however, neighboring two wavelength-bins had the same data number. I chose the center wavelength of the bin at a shorter wavelength as the λ_{ref} .

As the result, I found seven peaks commonly seen at a lot of directions and the reference wavelengths were fixed to $\lambda_{\text{ref}} = 8.47, 8.96, 9.56, 10.15, 10.65, 11.34, \text{ and } 11.84 \mu\text{m}$.

A position of a peak wavelength for 74 pointing directions is not always identical with the λ_{ref} . From each of the seven regions of $\lambda_{\text{ref}} \pm 2$ wavelength-bins in the observed/continuum spectrum at each direction, we selected the wavelength-bin that shows the most significant peak. The center wavelength of the bin was defined as a peak wavelength at the individual directions and denoted by λ_{peak} . The peak wavelength shift in the region around λ_{ref} is expressed by

$$\Delta\lambda_{\text{peak}} = \lambda_{\text{peak}} - \lambda_{\text{ref}} \quad [\mu\text{m}]. \quad (4.8)$$

Their absolute values do not have strong meanings because λ_{ref} depend on the definition. However, relative variations of $\Delta\lambda_{\text{peak}}$ among sky directions imply the difference of grain properties which

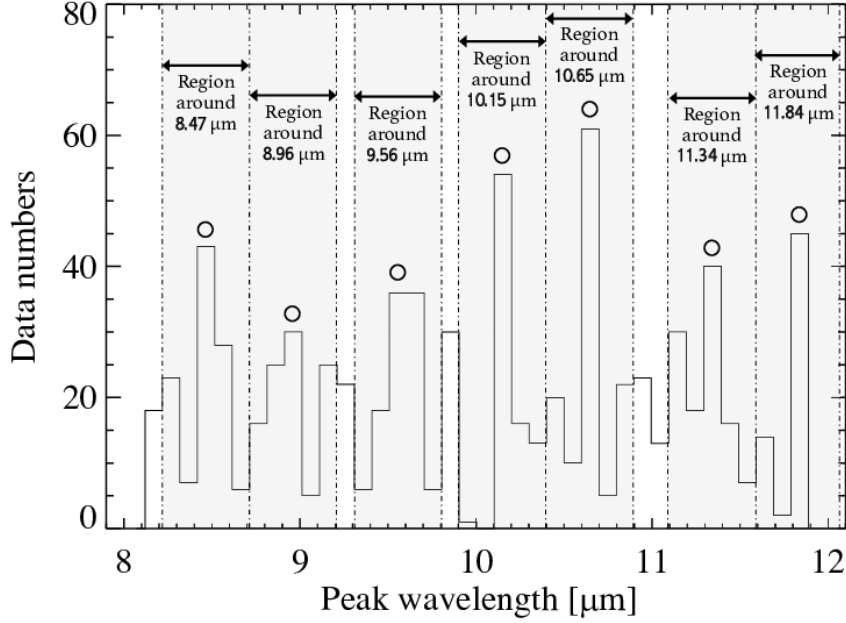


Figure 4.12: The histogram of peak wavelengths. Each wavelength-bin has a width of $\sim 0.1 \mu\text{m}$. Wavelength-bins selected for reference wavelengths were marked with a circle at the top side. I used the data in seven peak regions indicated by arrows.

affect wavelength positions of their emission peaks.

Figure 4.13 shows the resultant correlation of $\Delta\lambda_{\text{peak}}$ in each peak region with A and $|\beta_{\oplus}|$. Although $\Delta\lambda_{\text{peak}}$ does not change in most regions, the wavelength of the peak position around $11.34 \mu\text{m}$ is found to shift toward the shorter side at high $|\beta_{\oplus}|$. It is because two peaks originating from different types of minerals are contaminated in this region. A main peak around $11.25 \mu\text{m}$ is attributed to forsterite and enstatite adds a sub-peak on the skirt at $11.1 \mu\text{m}$. The enhancement of the enstatite sub-peak relative to the forsterite main peak at high $|\beta_{\oplus}|$ can cause such wavelength shift. It corresponds to the decrease of forsterite/(forsterite+enstatite) ratio at high $|\beta_{\oplus}|$. Assuming the contribution of the IPD from the OCCs at high $|\beta_{\oplus}|$, the IPD from the OCCs seems to have lower forsterite/(forsterite+enstatite) ratio than the IPD from the JFCs.

4.4.4 Equivalent width ratio of peak excesses due to crystalline silicates

$$: EW_{\text{fo}}/EW_{\text{en}}$$

The last parameter of the feature shape is the equivalent width ratio of peak excesses due to forsterite and enstatite, $EW_{\text{fo}}/EW_{\text{en}}$. I took into account the peak around 10.15 and $11.84 \mu\text{m}$ for calculating the equivalent width of forsterite peak, while the peak around 9.56 and $10.65 \mu\text{m}$ were considered

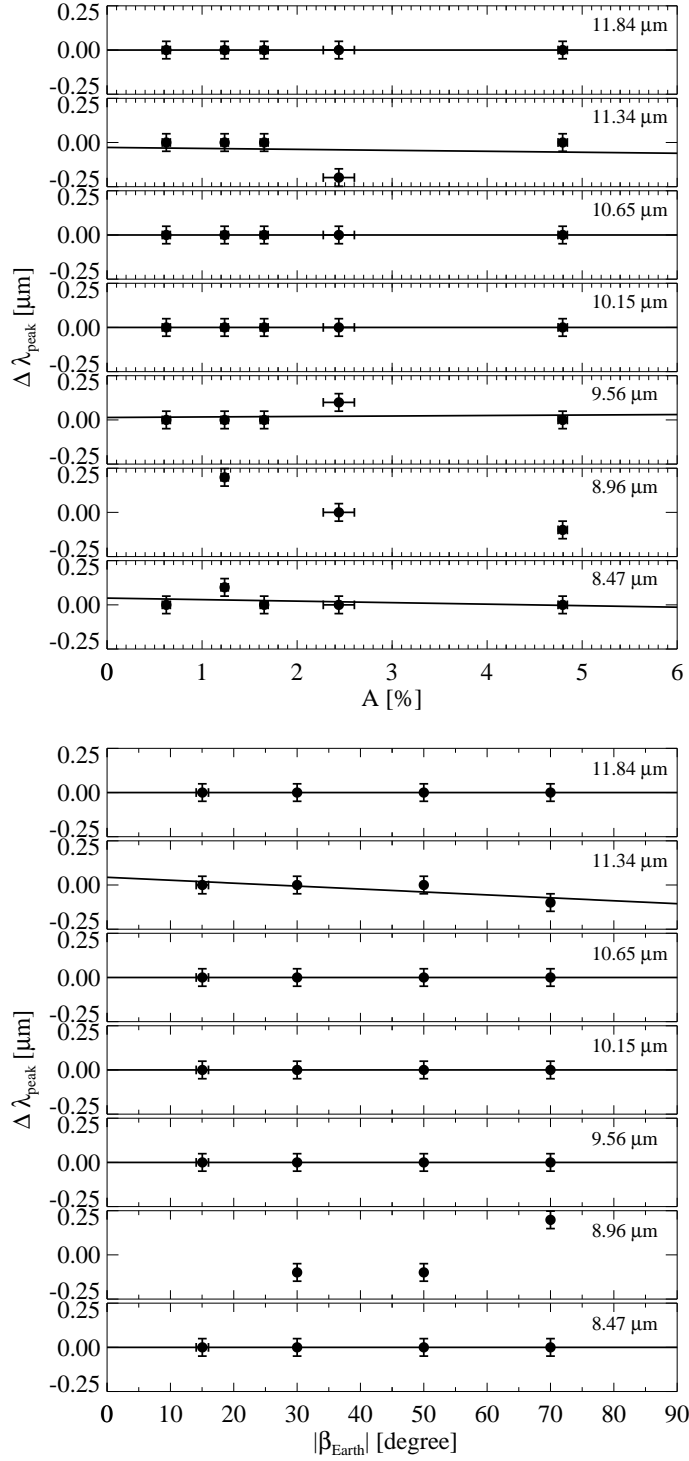


Figure 4.13: The dependence of a wavelength shift of a peak excess due to crystalline silicates ($\Delta \lambda_{\text{peak}}$) on the brightness contribution from the dust bands (A ; the top panels) and the ecliptic latitude ($|\beta_{\oplus}|$; the bottom panels). Each panel corresponds to the result on the peak in region around λ_{ref} which is denoted at the upper right side of the panel. Other explanations are same as Figure 4.9. In the region around 8.96 μm , some averaged observed/continuum spectra do not show a peak structure and we did not fit a linear line.

for enstatite peak. This parameter is calculated by:

$$\frac{EW_{\text{fo}}}{EW_{\text{en}}} = \frac{EW(10.15 \mu\text{m}) + EW(11.84 \mu\text{m})}{EW(9.56 \mu\text{m}) + EW(10.65 \mu\text{m})}, \quad (4.9)$$

where

$$EW(\lambda_{\text{ref}}) = \int_{\lambda_{\text{peak}}(\lambda_{\text{ref}}) - 0.25\mu\text{m}}^{\lambda_{\text{peak}}(\lambda_{\text{ref}}) + 0.25\mu\text{m}} \frac{Z_{\lambda} - C_{\lambda}}{C_{\lambda}} d\lambda \quad [\mu\text{m}]. \quad (4.10)$$

$\lambda_{\text{peak}}(\lambda_{\text{ref}})$ is the peak wavelength in the region around λ_{ref} at the individual bin. It means the wavelength intervals of integrations will change depending on the wavelength shift in each bin.

As represented in Figure 4.14, $EW_{\text{fo}}/EW_{\text{en}}$ seems to show the trend of a negative correlation to A , although the dispersion is significant. It may be due to the contribution of a smooth peak from phyllosilicate, as well as the case of $EW_{10.0-10.5}/EW_{9.0-9.5}$. Both forsterite and enstatite seem to have been replaced to phyllosilicate in the aqueous alteration process (Ganguly & Bose 1995; Bischoff 1998; Tomeoka et al. 1989). As the result, all peak excesses due to forsterite and enstatite are reduced and, instead, the smooth excess due to phyllosilicate replenish the excess strength around 10 μm but not the olivine peak around 11.84 μm , resulting in decrease in $EW_{\text{fo}}/EW_{\text{en}}$ defined as equation (4.9). In this case, $EW_{\text{fo}}/EW_{\text{en}}$ does not correspond to the forsterite/(forsterite+enstatite) ratio and the negative correlation between $EW_{\text{fo}}/EW_{\text{en}}$ and A indicates the hydration in the asteroidal IPD.

It can also be said that $EW_{\text{fo}}/EW_{\text{en}}$ correlates to $|\beta_{\oplus}|$ negatively with an accuracy of 1σ . This trend is consistent with the $|\beta_{\oplus}|$ -dependence of $\Delta\lambda_{\text{peak}}$ in the peak around 11.34 μm , which suggest the decrease of forsterite/(forsterite+enstatite) ratio at high $|\beta_{\oplus}|$. It is supportive evidence of lower forsterite/(forsterite+enstatite) ratio in the IPD from the OCCs compared with the IPD from the JFCs.

4.5 Summary of the grain properties

In section 4.3, I discussed the grain properties of the IPD from the JFCs as the typical properties seen in all directions. From the typical shape of emission features with sharp peaks significant especially at 9.60, 10.65, and 11.30 μm , the IPD from the JFCs was found to include small crystalline grains and be enstatite-rich. In order to reproduce the wavelength position of the enstatite peak shifted from 9.2 μm to 9.6 μm and the suppressed enstatite peak at 11.6 μm , enstatite grains included in the IPD from the JFCs may have extreme crystal morphologies like whisker- or platelet-shapes.

In section 4.4, I have investigated the feature shape dependence on two indicators of pointing

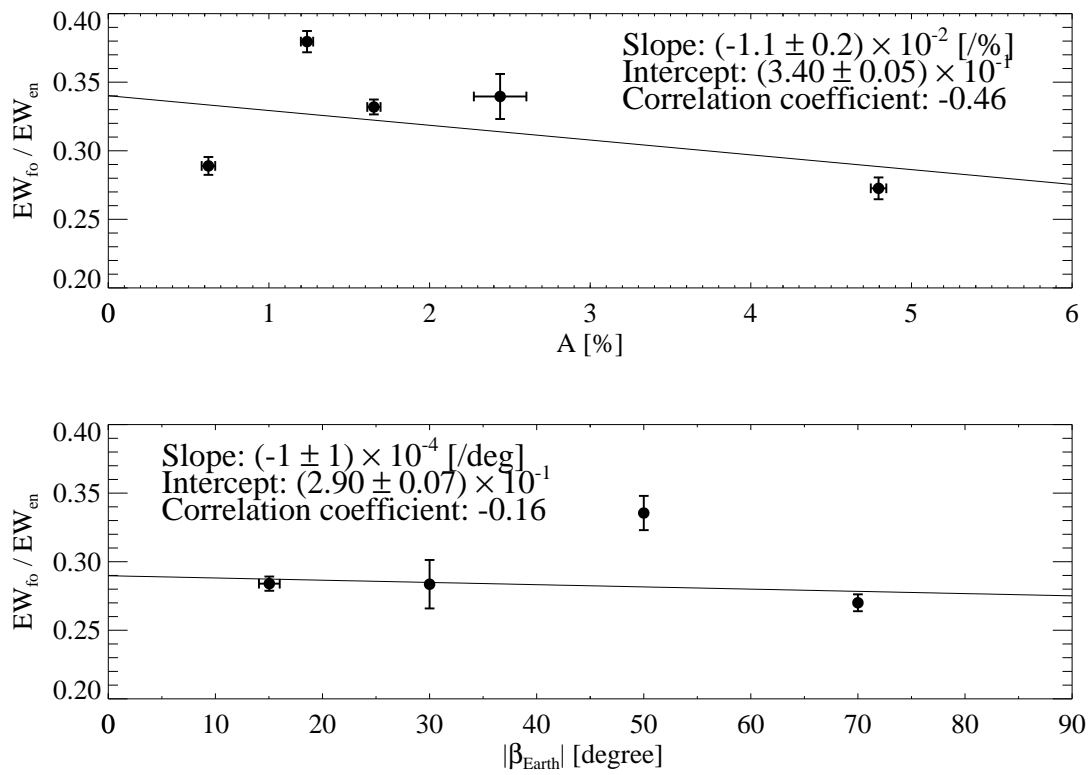


Figure 4.14: The dependence of the equivalent width ratio of peak excesses due to crystalline silicates (EW_{fo}/EW_{en}) on the brightness contribution from the dust bands (A ; the top panel) and the ecliptic latitude ($|\beta_{\oplus}|$; the bottom panel). Other explanations are same as Figure 4.9.

directions: the brightness contribution of the asteroidal dust bands, A , and the ecliptic latitude of the line of sight, β_{\oplus} . To evaluate feature shapes, I adopted 4 parameters: the equivalent width of the whole excess emission (EW_{whole}), the equivalent width ratio in 10.0–10.5 μm and 9.0–9.5 μm ($EW_{10.0-10.5}/EW_{9.0-9.5}$), a wavelength shift of a peak excess due to crystalline silicates ($\Delta\lambda_{\text{peak}}$), and the equivalent width ratio of peak excesses due to crystalline silicates ($EW_{\text{fo}}/EW_{\text{en}}$). I averaged the observed/continuum spectra in A - or $|\beta_{\oplus}|$ - bins and calculated the values of the feature shape parameters for the averaged spectra. I found some correlations between the feature shape and the pointing direction as shown in Figure 4.9, 4.11, 4.13, and 4.14. I summarized the best-fit slopes and the fitting accuracy in Table 4.1.

The positive correlation between EW_{whole} and $|\beta_{\oplus}|$ indicates the increase in the fraction of small grains at the higher ecliptic latitudes, which is consistent with previous works and can be explained by the collisional cascade during the accretion of IPD particles due to the PR drag. On the other hand, the negative correlation between EW_{whole} and A was found. It means that the size distribution of the asteroidal IPD is biased to relatively larger grains owing to grains in the middle of the collisional cascade from asteroids.

The positive and negative correlation with A of $EW_{10.0-10.5}/EW_{9.0-9.5}$ and $EW_{\text{fo}}/EW_{\text{en}}$, respectively, can be qualitatively explained by the evidence of aqueous alteration from forsterite and enstatite to phyllosilicate in the asteroidal IPD, which is consistent with the result of laboratory measurements of CM chondrites and the observations of C-complex asteroids.

The IPD from the OCCs was found to have a lower olivine/(olivine+pyroxene) ratio than that of the IPD from the JFCs regarding both amorphous and crystalline grains, from the negative $|\beta_{\oplus}|$ -dependence of $EW_{10.0-10.5}/EW_{9.0-9.5}$, $\Delta\lambda_{\text{peak}}$ in the peak around 11.34 μm and $EW_{\text{fo}}/EW_{\text{en}}$.

Table 4.1: The slopes of the linear functions of A or $|\beta_{\oplus}|$ that best fit EW_{whole} , $EW_{10.0-10.5}/EW_{9.0-9.5}$, $\Delta\lambda_{\text{peak}}$, and $EW_{\text{fo}}/EW_{\text{en}}$. The reduced- χ^2 of each fit and correlation coefficient r are also shown. These slope values are plotted in Figures 4.9, 4.11, 4.13, and 4.14, respectively.

parameter type	$\lambda_{\text{ref}} [\mu\text{m}]$	A-dependence			$ \beta_{\oplus} $ -dependence		
		Slope ^a	reduced- χ^2	r	Slope ^b	reduced- χ^2	r
EW_{whole}	–	$(-7.1 \pm 0.5) \times 10^{-3}$	287.42	-0.49	$(1.96 \pm 0.04) \times 10^{-3}$	21.68	0.46
$EW_{10.0-10.5}/EW_{9.0-9.5}$	–	$(4 \pm 1) \times 10^{-2}$	6.44	0.50	$(-5.4 \pm 0.5) \times 10^{-3}$	0.56	-0.97
$\Delta\lambda_{\text{peak}}$ ^c	8.47	$(-1 \pm 1) \times 10^{-2}$	0.96	-0.31	$(0 \pm 1) \times 10^{-3}$	0.00	-0.51
	8.96	–	–	–	–	–	–
	9.56	$(0 \pm 1) \times 10^{-2}$	1.06	0.10	$(0 \pm 1) \times 10^{-3}$	0.00	0.51
	10.15	$(0 \pm 1) \times 10^{-2}$	0.00	0.19	$(0 \pm 1) \times 10^{-3}$	0.00	-0.51
	10.65	$(0 \pm 1) \times 10^{-2}$	0.00	0.19	$(0 \pm 1) \times 10^{-3}$	0.00	0.51
$EW_{\text{fo}}/EW_{\text{en}}$	11.34	$(-1 \pm 1) \times 10^{-2}$	4.22	-0.10	$(-2 \pm 1) \times 10^{-3}$	0.54	-0.69
	11.84	$(0 \pm 1) \times 10^{-2}$	0.00	-0.19	$(0 \pm 1) \times 10^{-3}$	0.00	0.51
	–	$(-1.0 \pm 0.2) \times 10^{-2}$	34.19	-0.46	$(-1 \pm 1) \times 10^{-4}$	10.42	-0.16

^a Unit of $[\mu\text{m}/\%]$ for EW_{whole} and $\Delta\lambda_{\text{peak}}$, $[\%]$ for $EW_{10.0-10.5}/EW_{9.0-9.5}$ and $EW_{\text{fo}}/EW_{\text{en}}$. The max amplitude of A is $< 6\%$.

^b Unit of $[\mu\text{m}/\text{deg}]$ for EW_{whole} and $\Delta\lambda_{\text{peak}}$, $[\text{deg}]$ for $EW_{10.0-10.5}/EW_{9.0-9.5}$ and $EW_{\text{fo}}/EW_{\text{en}}$. The possible max amplitude of $|\beta_{\oplus}|$ is 90 degree.

^c Since $\Delta\lambda_{\text{peak}}$ can take only a discrete value, the values of reduced- χ^2 and correlation coefficients do not have strong meaning.

Chapter 5

Implications for the proto-solar system

In the last chapter of my thesis, I will discuss the environment in the proto-solar system, where dust has evolved and been incorporated into asteroids or comets. As I mentioned in section 1.2, the grain properties of the IPD currently observed represent the grain properties of dust in the forming region of the parent planetesimals. In the chapter 4, I derived the typical property of the IPD, which is thought to be that of the IPD from the JFCs. In addition, I found the difference in the mineral composition of the IPD from the JFCs and the OCCs for the first time. Hereafter, I will discuss the environment in the forming region of the JFCs and the OCCs, and the radial dependence of the mineral composition in the proto-solar disk.

5.1 Comet forming region

I introduce the conventional prediction for forming regions of the JFCs or the OCCs. The present orbits of the JFCs are thought to have an aphelion around the Jupiter orbit (i.e., ~ 5 au), while that of the OCCs orbits is much further like tens thousands of au. However, their present orbits are not identical to that just after the comets core have been formed from dust. At the age of a few tens Myr, the cores of gas-giant planets (the Jupiter and the Saturn) and ice-giant planets (the Uranus and the Neptune) in the proto-solar system migrated and gravitationally scattered planetesimals around them.

Thommes et al. (1999) proposed the cores of four giant planets were formed in a considerably more compact configuration around 10 au and interacted with each other through mean motion

resonances. They were surrounded by planetesimals broadly located between 4–40 au in the disk. Gravitational interactions of planetesimals with the Neptune caused the outer three planets to gain angular momentum while the Jupiter lost the angular momentum. The repartition of angular momentum caused the Jupiter and the Saturn to cross their 2:1 mean motion resonance and excited the system (Tsiganis et al. 2005).

This resulted in not only the migration of four giant planets but also the gravitational scattering of planetesimals both inward and outward. Planetesimals that have been flown outward composed a scattered disk distributing to tens thousands of au, and at the outer edge, their inclinations were enhanced to the isotropic distribution due to the interactions with outside of the solar system like a galactic tide (Dones et al. 2004). This is a formation scenario of the Oort Cloud. It means cores of the OCCs were formed in the region of 4–40 au.

Planetesimals with the initial orbits around 15–40 au, however, have the longer time scale to be scattered compared with planetesimals with the inner initial orbits. They could remain at the scattered disk (Duncan & Levison 1997). Because any mean motion resonance did not protect them from close encounters, their orbits could be perturbed and changed to that of the JFCs. Therefore, the JFCs are thought to be formed in the region of 15–40 au, and as the result of such gravitational scattering, have a present aphelion around the Jupiter orbit.

These planet migration scenarios are called “Nice model” and supportive to the reproduction of present orbits of the Uranus and the Neptune switching their order, the eccentricity of the Pluto, the Late Heavy Bombardment indicated by returned samples of the Moon (Gomes et al. 2005) and the formation of the Kuiper Belt (Levison & Morbidelli 2003).

On the basis of the prediction by this model, I assumed that the grain properties of the IPD from the JFCs represent properties of dust grains located in an outer region like > 15 au of the proto-solar disk, while that of the IPD from the OCCs is affected also by properties of dust grains in the inner region like 4–15 au. From the grain properties of the IPD from the JFCs described in section 4.5, the proto-solar disk seems to include crystallized enstatite-rich small grains with extreme crystal morphologies even in the outer region like > 15 au. Since I found the IPD from the OCCs has a lower forsterite/(forsterite+enstatite) ratio and a lower olivine/(olivine+pyroxene) ratio of amorphous silicates compared with the IPD from the JFCs, dust grains in the inner region of the proto-solar disk are expected to have such ratios lower than that in the outer region. It implies the radial dependence of the mineral composition in the proto-solar disk.

5.2 Dust mixing process

In the interstellar medium, the degree of crystallinity in silicate dust is only 1.1% (Kemper et al. 2005). Therefore, silicate crystals seen in the IPD should be formed by re-condensation from the solar nebula gas and/or annealing of the amorphous interstellar (i.e., pre-solar) dust. In the pressure environment at the mid-plane of the proto-solar disk, the equilibrium condensation temperature of enstatite and forsterite is 1300 K and 1400 K, respectively (Gail 2004). Hallenbeck et al. (2000) shows the annealing temperature of silicates is about 950 K.

However, such high temperature is possible only near the Sun (at least less than a few au), if we assume the global radial dependence of disk temperature in a stationary disk model (Gail 2001; Bell et al. 1997; Murata et al. 2009). It indicates that some mechanisms are required for local heating and/or radial mixing of the dust population.

Harker & Desch (2002) suggested the local heating by nebula shocks triggered by gravitational instabilities. They concluded that in-situ annealing of submicron- and micron-sized silicate dust grains can occur in the region of 5–10 au. However, it cannot explain the silicate crystallization in the outer region (> 15 au), in which dust have been incorporated into the JFCs. Another hypothesis for local heating is exothermic chemical reactions of an amorphous silicate core covered with an amorphous carbon layer containing reactive molecules (Tanaka et al. 2010). Although they showed silicate annealing can occur in wider astrophysical conditions than considered before, it still need an initial temperature of a few hundred Kelvins, which is much higher than disk temperature at the JFCs forming region.

On the other hand, several hypotheses for radial mixing have been proposed. I introduce three primary models of them. The first one is turbulence mixing model (Gail 2004). In proto-planetary disk, rotating gas accretes to the central star owing to loss of angular momentum caused by viscous. Dust grains embedded into the carrier gas also drag inwards and approach to the star. In inner region with high temperature (> 1000 K), initially amorphous dust is vaporized to the gas phase or sometimes annealed to the crystals. Turbulent diffusion can cause the gas and dust grains to be mixed inwards and outwards and tends to smear out the radial concentration gradients. In the gas moving outwards and being cooled, dust is re-condensed by nucleation and grain growth or accumulation onto the surface of already existing grains. Gail (2004) has simulated the final radial dependence of dust compositions after these processes, considering the dynamical evolution and chemical reactions in the photo-solar disk. According to their result, some fractions of silicate crystals can exist and be incorporated into planetesimals at more than a few tens of au. However, the relative abundance ratios of forsterite/(forsterite+enstatite) in crystalline dust and olivine/(olivine+pyroxene) in amorphous

dust do not depend on the radial distance. This seems to be inconsistent with our result which indicates a lower forsterite/(forsterite+enstatite) ratio and a lower olivine/(olivine+pyroxene) ratio in the inner region (4–15 au) than that in the outer region (> 15 au). I should note that the simulated result strongly depends on the assumptions. This model assumed the chemical equilibrium condensation from the gas with an initial solar composition Gail (2004). Since the condensation temperature of forsterite is higher than that of enstatite, SiO_2 gas could condense to forsterite at first and then the forsterite could react to enstatite in equilibrium. Therefore, the primary mechanism for the formation of enstatite in equilibrium is by secondary reactions of solid forsterite with gas, not by the direct condensation from the gas (Bradley et al. 1983). According to the results of laboratory measurements, however, whisker-shaped enstatite grains with screw dislocation have been found (Bradley et al. 1983). Such grains can be formed by the direct condensation from SiO_2 gas or liquid. Since molecules are difficult to exist as liquid in space, it is expected that the enstatite grains have been formed directly from the gas phase. It means the assumption in this mixing model may be inconsistent with the result of the laboratory measurement. In order to compare the result in this thesis with the model, therefore, it is required to simulate on other assumptions including the direct condensation from SiO_2 gas to enstatite.

Secondly, X-wind model has been suggested (Shu et al. 1996; Ciesla 2009). The scenario of this model is like the following. Young stars rotate with the magnetosphere represented by closed magnetic field lines connected between the two poles. Their accretion disks interact with the rotating magnetosphere. In the region in which pure Keplerian rotation of the disk fall behind the spin of the star and the field lines, the field lines are bent and bow outward as opened field lines. Along the opened field lines, disk materials are flown outward and above the disk by magneto-centrifugally driven wind (X-wind). Dust materials decouple from the gaseous flow and rain back down onto the surfaces of the outer disk. The grains are then mixed into the mid-plane of the disk by turbulent diffusion. However, we cannot discuss the more detailed consistency between this model and my thesis results, because no simulation has shown the radial distribution of mineral composition at the final stage in these processes.

As the latest hypothesis, Vinković (2009) argued outward transportation of dust by radiation pressure; the radiation from the disk itself helps grains to levitate from the disk, and then, solar photons cause the grains to glide over the disk surface toward outer region. This process is also not modeled enough to evaluate the radial dependence of mineral composition.

In this work, I have implied the qualitative radial dependence of mineral composition in the proto-solar disk on the basis of the observational results for the first time. This may become useful to

identify which radial mixing model is more reliable, if radial dependence of the mineral composition at the final stage of mixing process will be predicted in each model.

5.3 Future works

5.3.1 Quantitative evaluation of the mineral composition

Natural extension of this thesis work is to quantitatively evaluate the mineral composition at each pointing direction, by fitting of a superposition of mineral absorption coefficients to obtained observed/continuum spectra. Relative strength ratios of emission peaks originating from different types of minerals indicate the abundance ratios between the original minerals, i.e., the mineral composition. For this extension, it is essential to find out the appropriate candidate minerals whose Q_{abs} can reproduce the wavelength position and the width of each observed peak. According to my thesis results, the consideration of crystals with anisotropic morphologies is necessary. Single ellipsoidal morphology can cause extremely sharp peaks at the specific wavelengths. Different morphologies result in slightly different wavelength positions for some peaks. In the actual spectra, we will see a superposition of such peaks determined by the morphology distribution of the crystals in the line of sight.

This future extension will be tackled by three steps. First, I will select a representative morphology of each crystalline mineral so that the wavelength position of observed peaks can be reproduced, without considering the width and relative strength of the peaks. Secondary, I will focus on the peak widths and estimate the spread of morphology distribution for each mineral around the representative morphology. Finally, I will restrict the fraction of each mineral so that the relative peak strength can be explained, by fitting of a superposed Q_{abs} with estimated morphology distributions.

5.3.2 Further observations

The future extension described in the last section will enable us to infer the spatial distribution of the IPD mineral composition. In order to distinguish the composition of the IPD from the OCCs from that of the IPD from the JFCs, we need to know the fraction of the isotropic IPD components originating from the OCCs. This is accomplished by the in-situ measurement of zodiacal emission brightness or number counting of the IPD particles using explorers which escape from the ecliptic plane toward the ecliptic pole directions.

In this thesis work, it was suggested that the asteroidal IPD might include hydrated silicate which is an evidence of the aqueous alteration. Since the main contributor for the dust bands is

thought to be the IPD from the C-type asteroid family, a sample return from Ryugu, which is a C-type asteroid, performed by HAYABUSA-2 can be a supplemental information source. After the sample return to the Earth and the investigation of detailed properties of the samples, I can feedback the information about the interpretation of data obtained by remote sensing observations.

In section 5.2, I introduced some models of radial mixing to explain the radial distribution of the grain composition. The observations of exo-planetary systems also give us clues to the models. Although it is difficult to see through the mid-plane of proto-planetary disks from outside, such observations may enable us to reveal whether the transportation of materials on the disk surfaces is triggered by the X-wind or by the radiation pressures.

Chapter 6

Conclusion

The IPD is thought to be recently supplied from the inside of primordial planetesimals like asteroids or comets. The IPD grain properties, which depend on the types of parent bodies, can give us the information about the environment in the proto-solar system. Previous study has investigated them in terms of spectral features seen in the zodiacal emission. However, past observations of the zodiacal emission spectra did not have high signal-to-noise ratio and differences in the grain properties of the IPD from different types of parent bodies were not discussed. In order to detect such differences, I compared the zodiacal emission spectra among various directions of the sky, because the IPD from different types of parent bodies has different spatial distributions. I used mid-infrared spectroscopic data of the zodiacal emission at 74 different directions obtained with the MIR-S channel of AKARI/IRC.

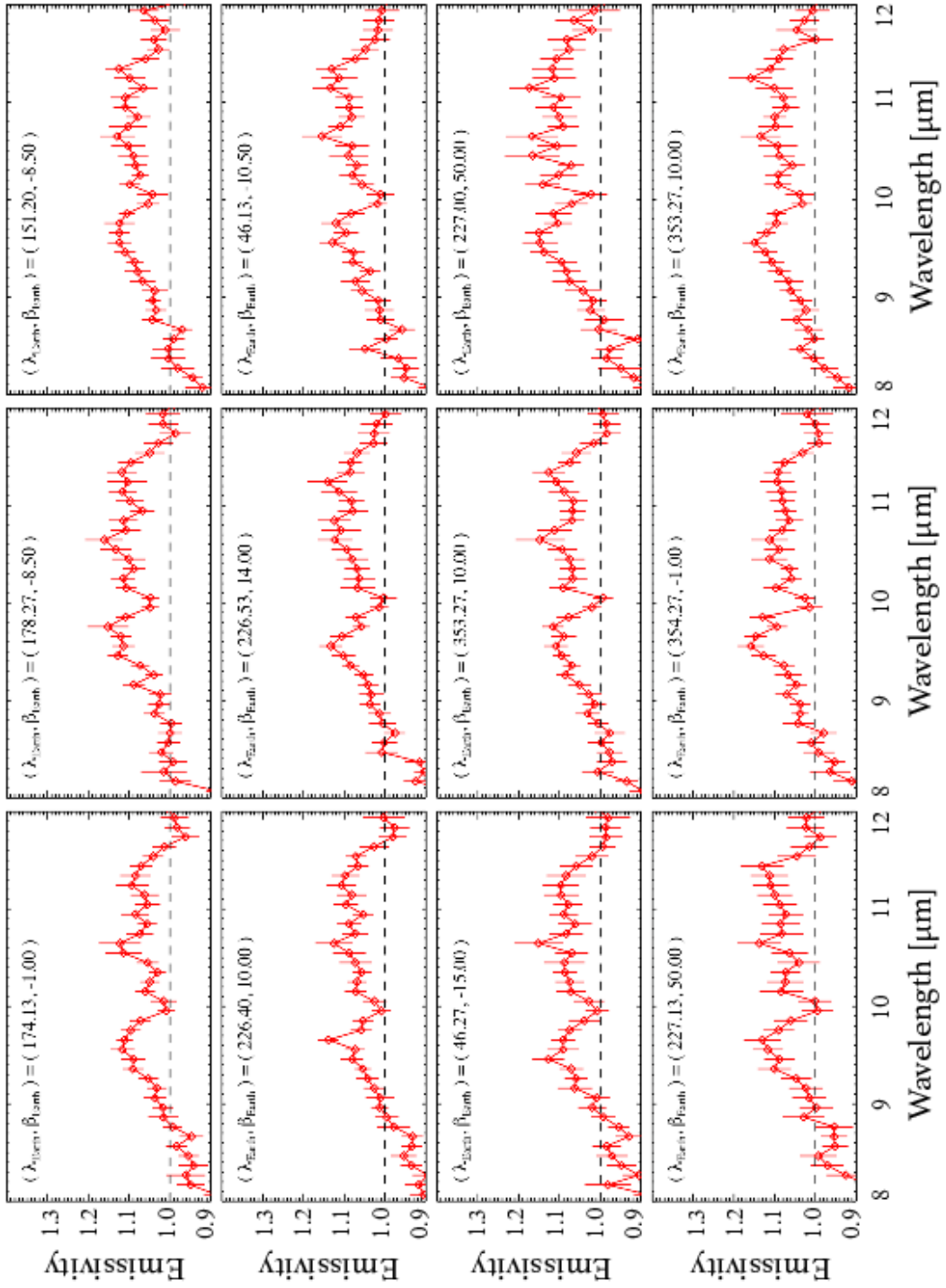
After the successful subtraction of the instrumental artifacts, I obtained zodiacal emission spectra at each direction. They exhibit the excess emission at the 9–12 μm range and even some sharp peaks. As the result of the comparison with the absorption coefficients of the candidate minerals, the IPD was found to typically include small silicate crystals, especially enstatite grains with extreme crystal morphologies. I also found that the shape of spectral features depends on the ecliptic latitudes. As the result of the investigation into the shift of peak wavelengths and the excess strength of each peaks, the IPD at the higher ecliptic latitudes seems to have the lower olivine/(olivine+pyroxene) ratio of both crystalline and amorphous silicates. It indicates that the IPD from the OCCs, which distributes isotropically, has a lower forsterite/(forsterite+enstatite) ratio and a lower olivine/(olivine+pyroxene) ratio of amorphous silicates, compared with the IPD from JFCs, which distributes mainly near the ecliptic plane.

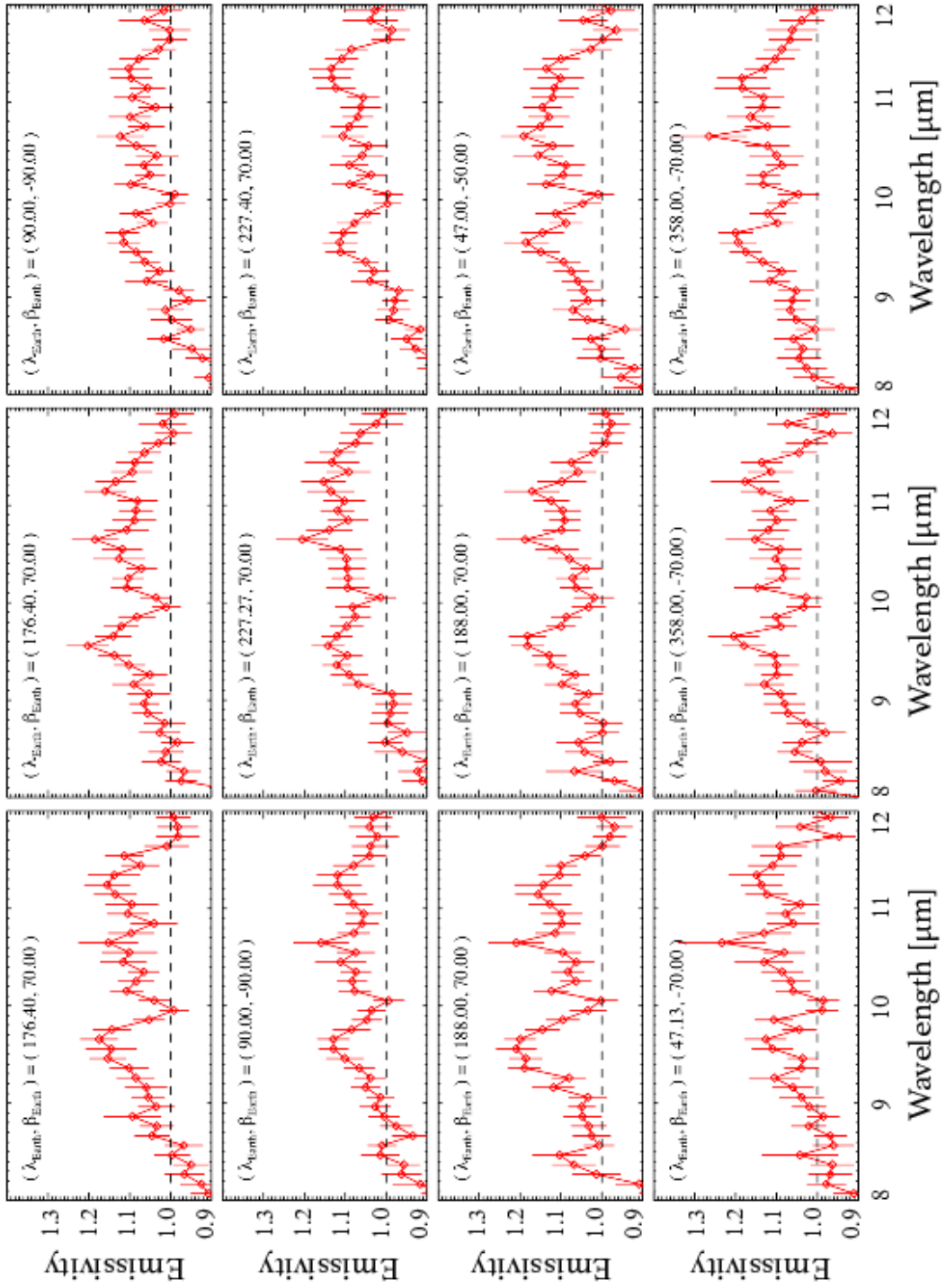
According to the prediction by the Nice model, the JFCs, which is the main origin of the IPD, has

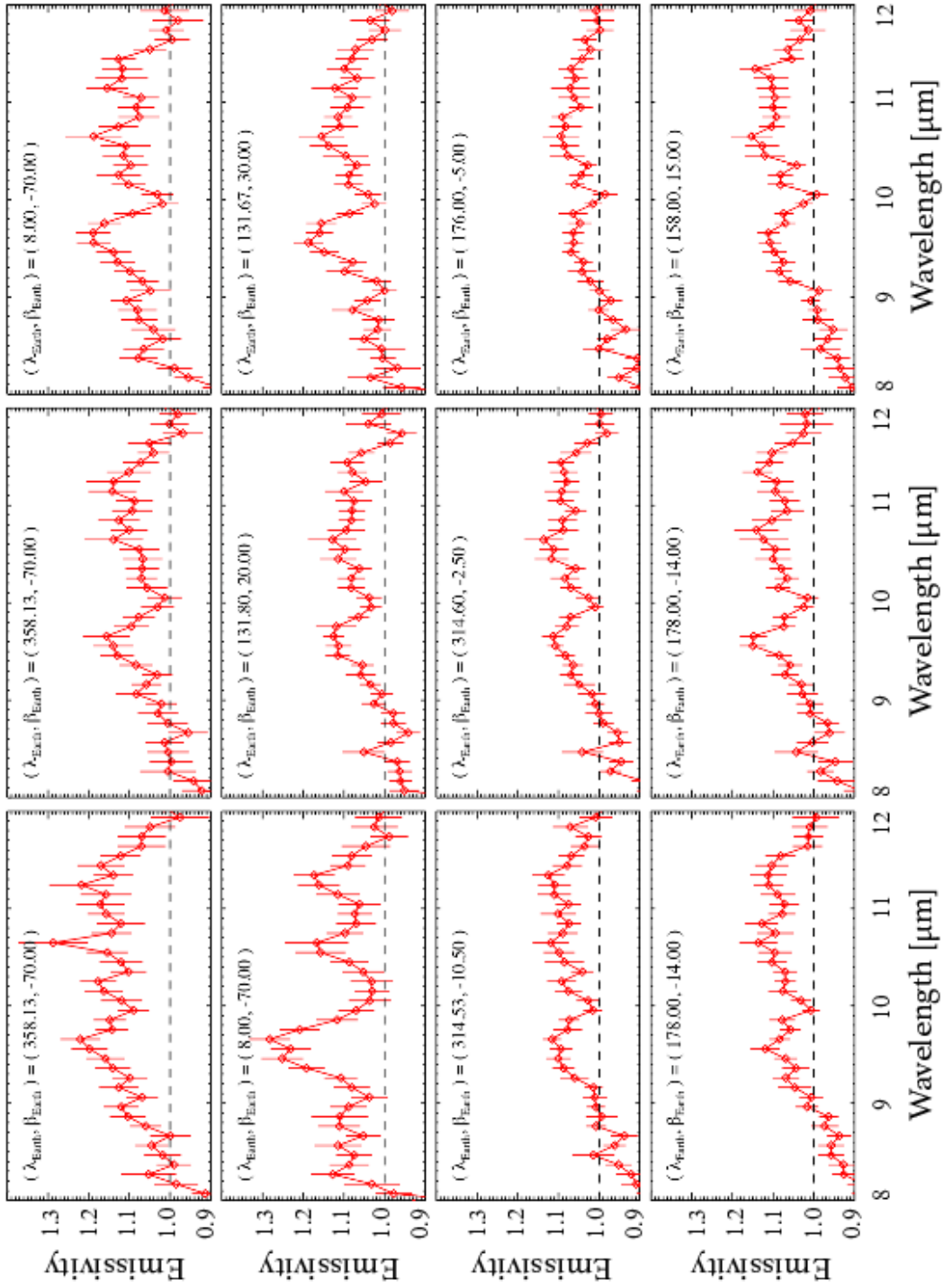
been formed only in the outer region like > 15 au. The existence of silicate crystals in the IPD implies the radial dust mixing process in the proto-solar disk, because such crystals can be formed only in the region close to the Sun. Moreover, my thesis result on the differences of the grain properties between the IPD from the JFCs and the OCCs suggests that the grain properties of the dust in the proto-solar disk depend on the radial distance from the Sun, because the OCCs is thought to be formed also in the inner region like 4–15 au. For further discussions, many types of observations are necessary, including in-situ measurements of the IPD and observations of exo-planetary systems.

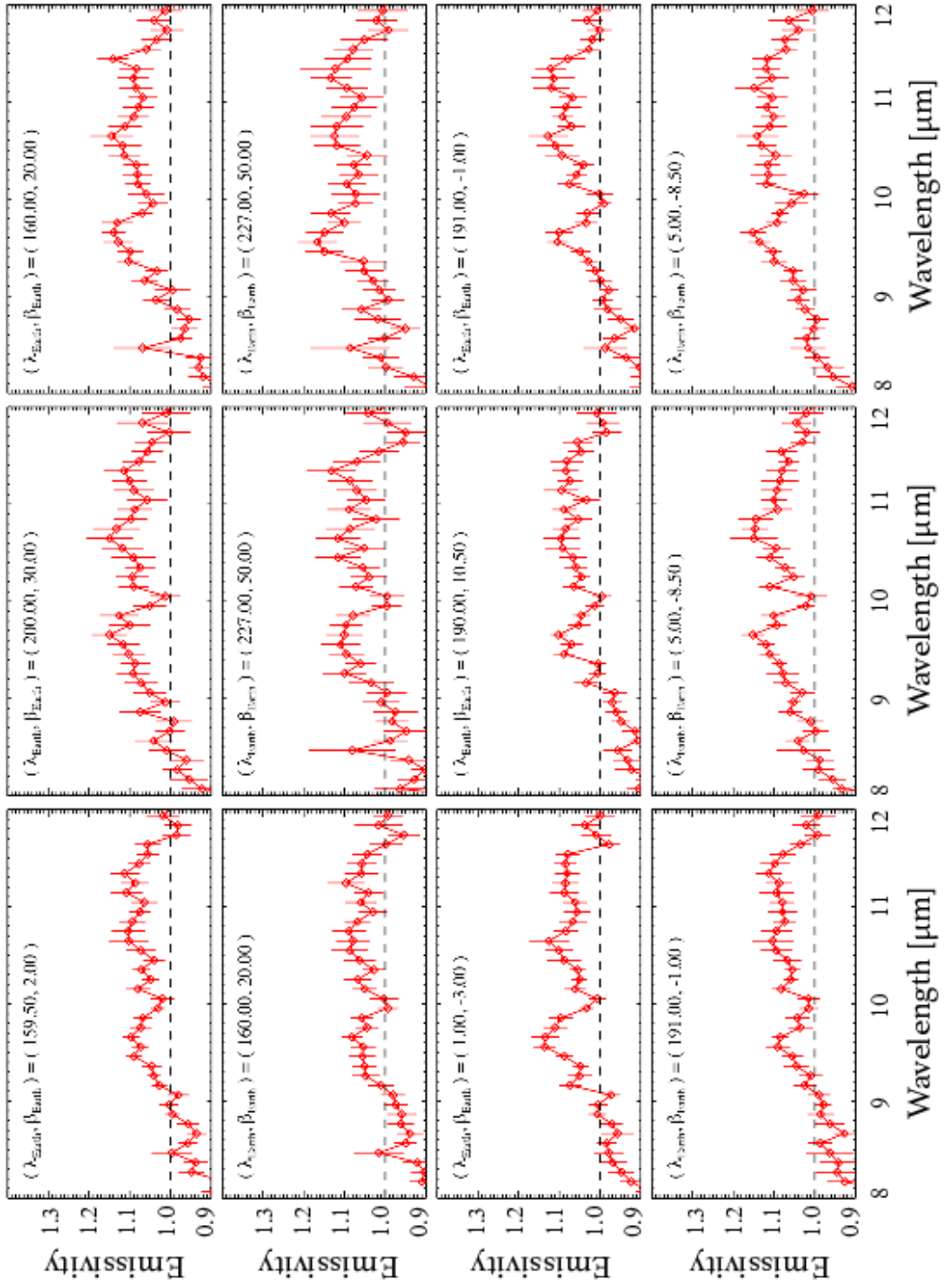
Appendix 1

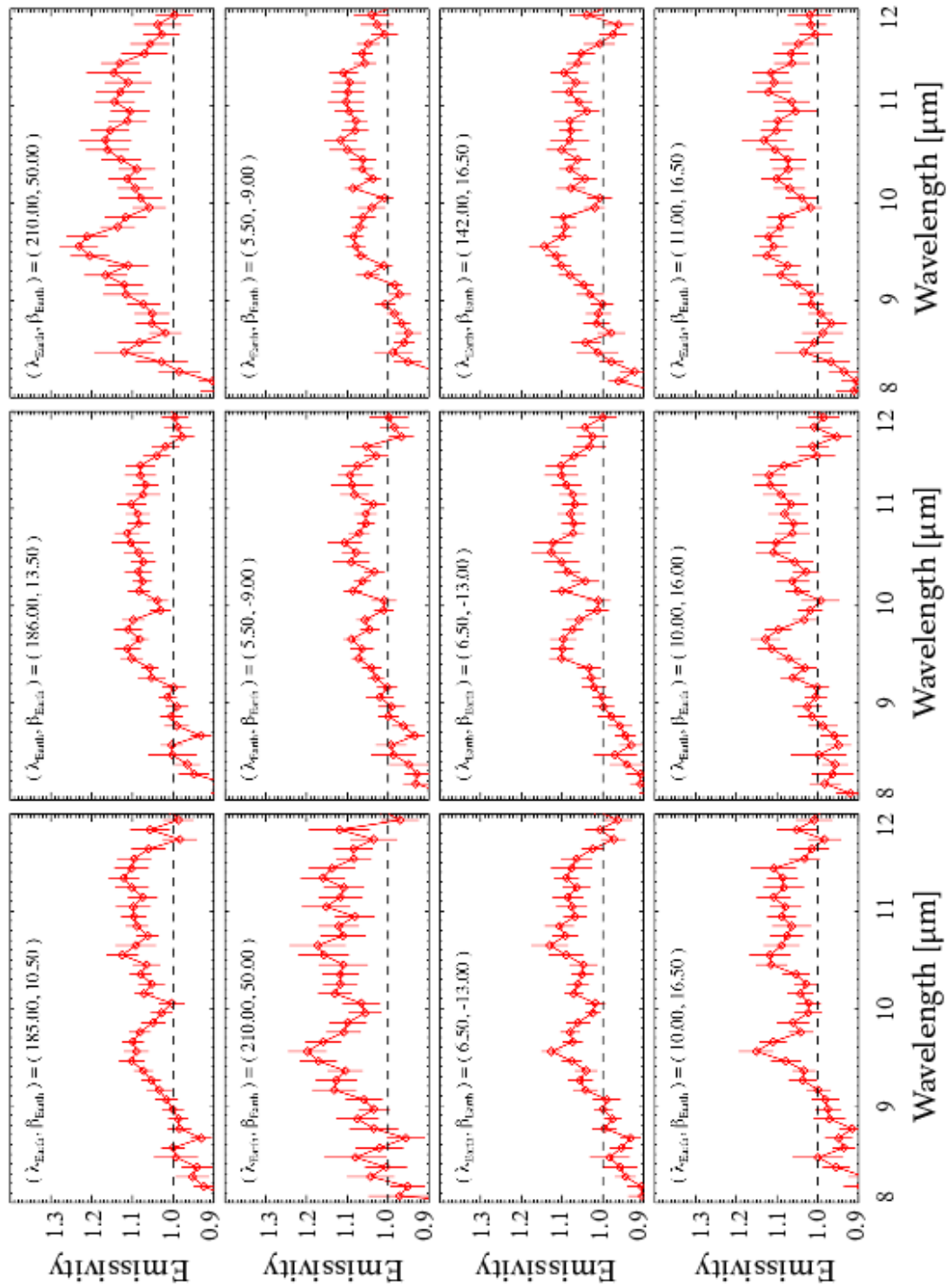
I show all observed/continuum spectra at 74 pointing directions from the next page. I obtained them by following the reduction flow described in section 3.2 and dividing by the continuum as mentioned in section 4.1.

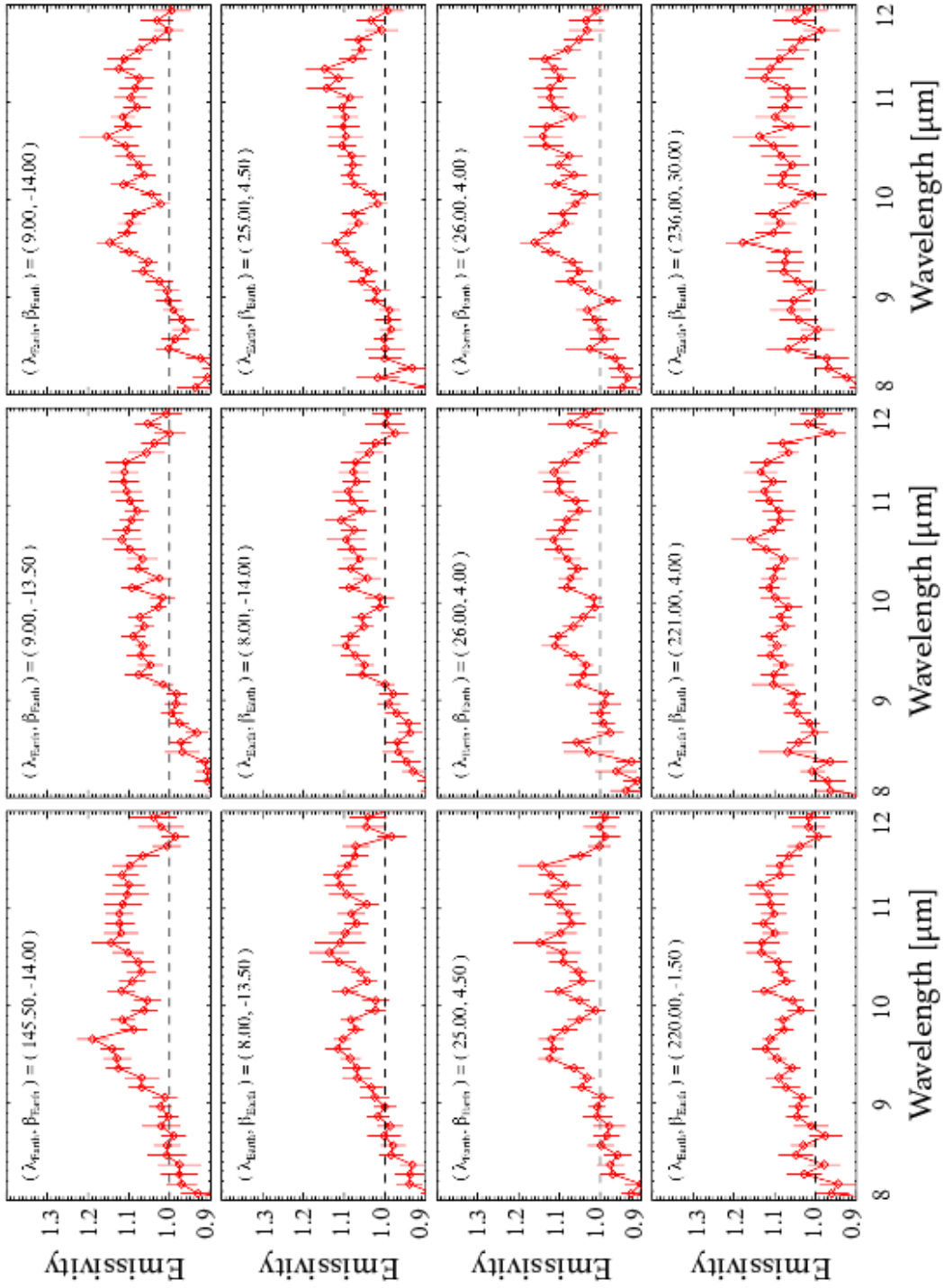


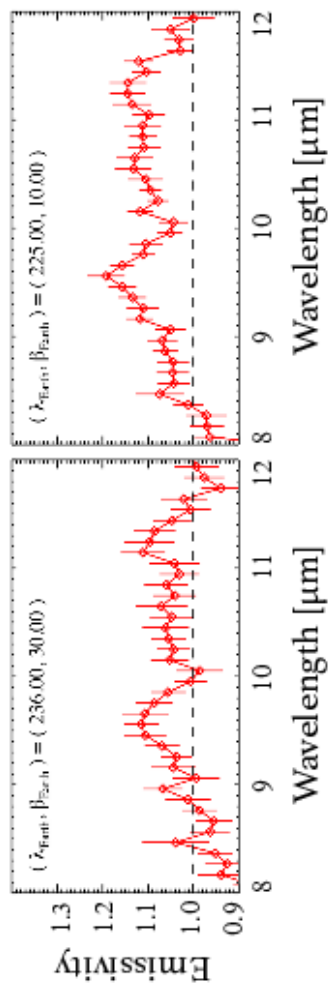












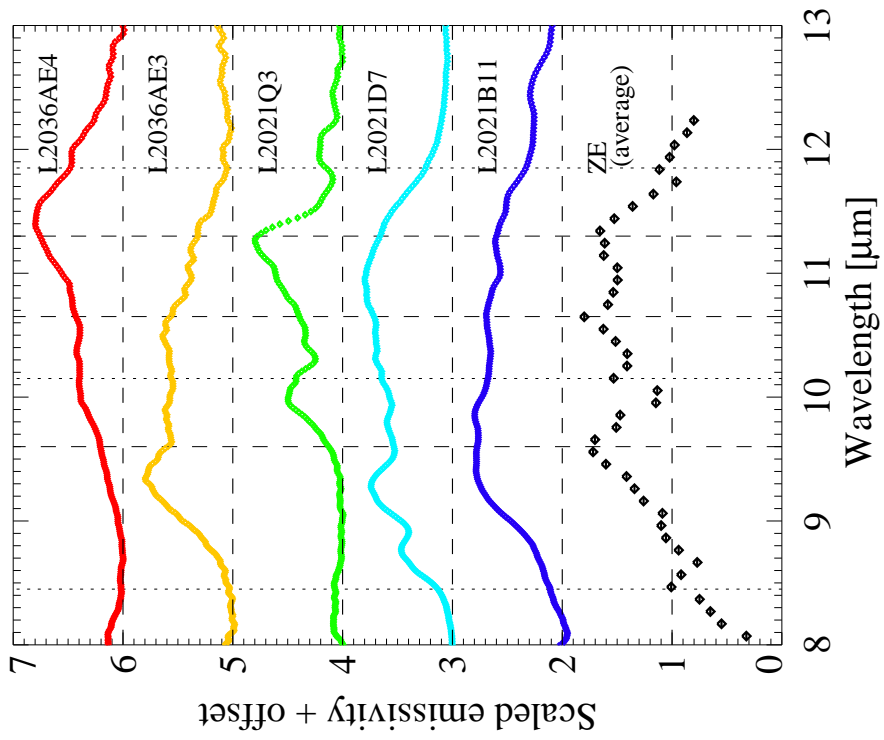
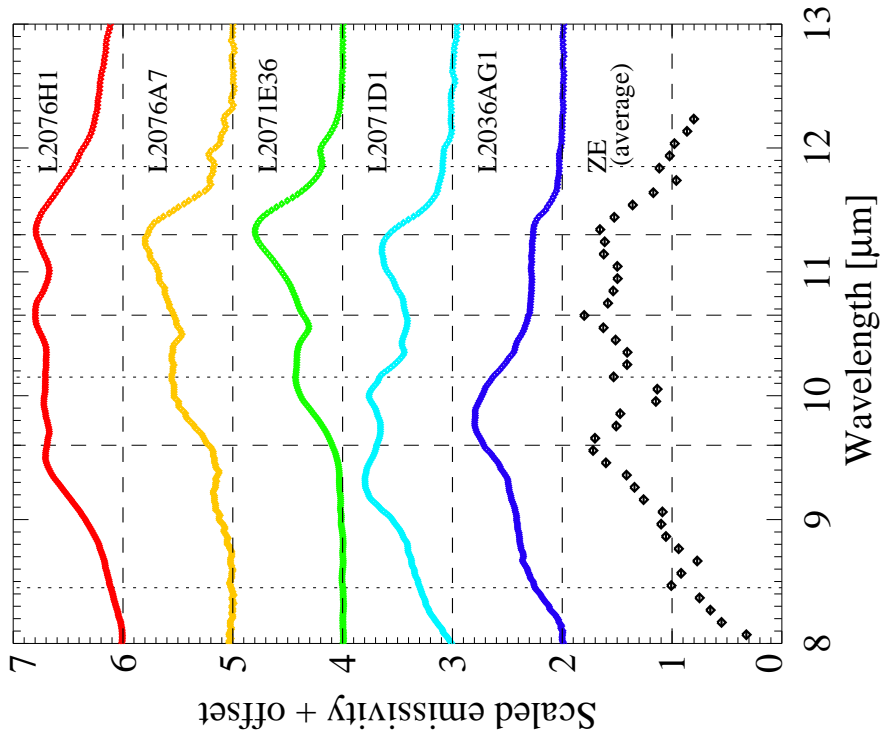
Appendix 2

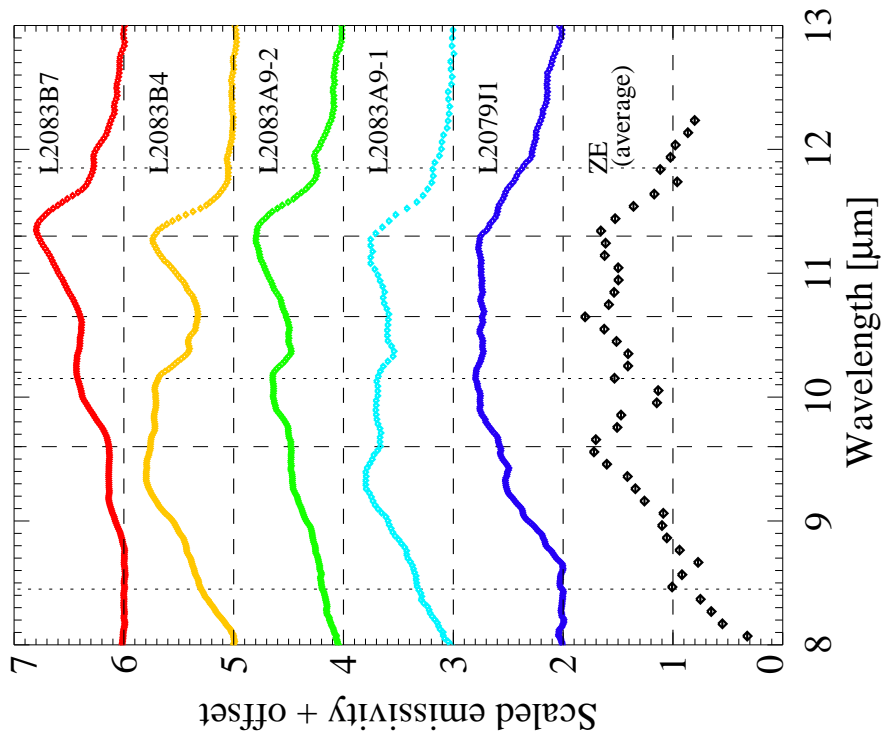
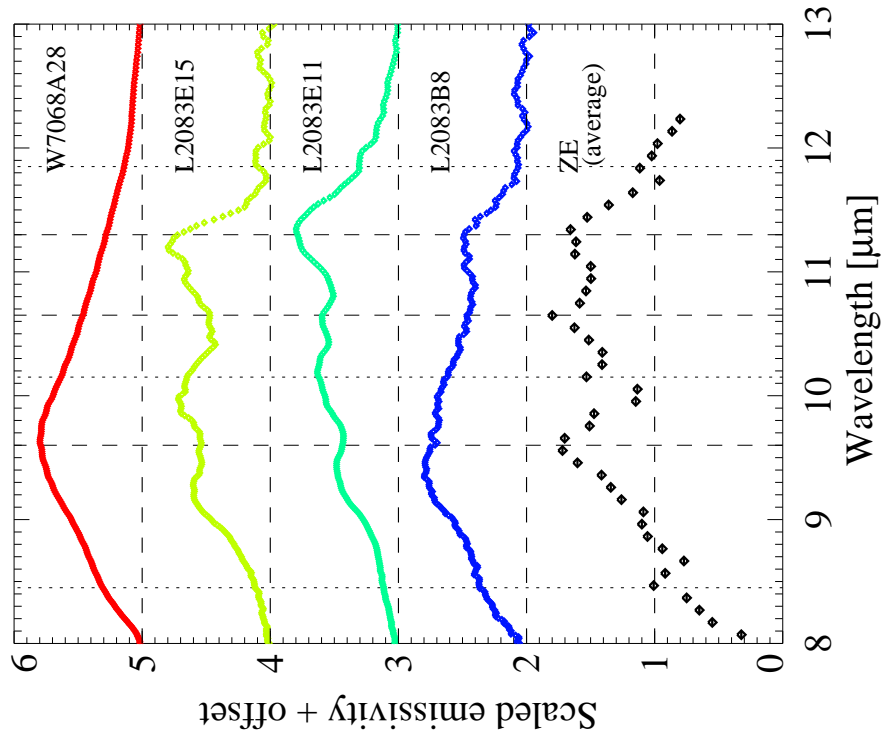
Following figures show the mid-infrared spectra of various types of objects related to the IPD: collected dust particles, collected meteorites, asteroids and cometary dust coma. At the bottom of each panel, I plot the observed/continuum spectrum of the zodiacal emission (ZE) averaged in 74 pointing directions for comparisons. Vertical lines indicate the wavelength positions of the peaks clearly seen in the averaged ZE spectra. Dashed lines are main peaks originating from enstatite, while dotted lines are sub peaks attributed to forsterite (see section 4.2). All of them are offset vertically from each other by unity for clarity, and scaled so that the max values become 0.8 above each baselines.

Spectra of collected dust particles

Dust particles collected near or on the Earth are samples ideal to investigate the detail of the grain properties, although they are biased to the dust which can easily approach to the Earth and altered or destroyed by atmospheric entry heating. I compare the spectra of 19 samples with that of the zodiacal emission. These data were published in Merouane et al. (2014) and I got the text data from P.Vernazza in Aix Marseille University and S.Hasegawa in ISAS/JAXA.

The collected samples have a variety of the feature shape. Although many samples seem to be forsterite-rich, some shows the clear enstatite-peaks or the convex shape originating from amorphous pyroxene, which is also seen in the averaged ZE spectra. I note that the enstatite peak in the 9 μm -band appear around 9.2 μm , which can be explained by the spherical grains, while the peak is shifted to 9.6 μm in the averaged ZE spectra. It may be due to the alteration or destruction of crystals with an extreme morphology during the entry.

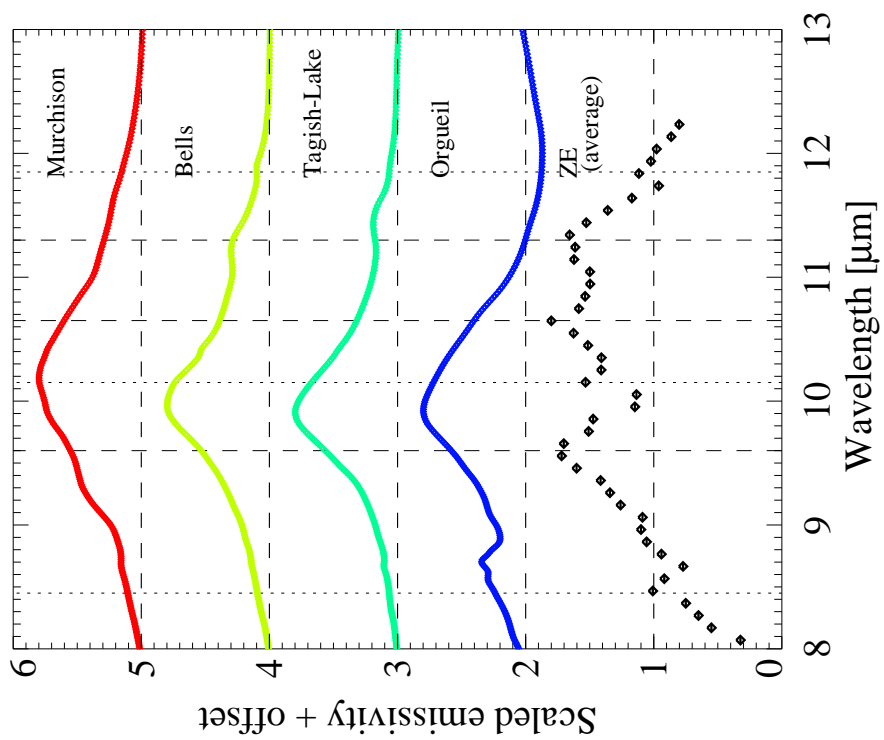
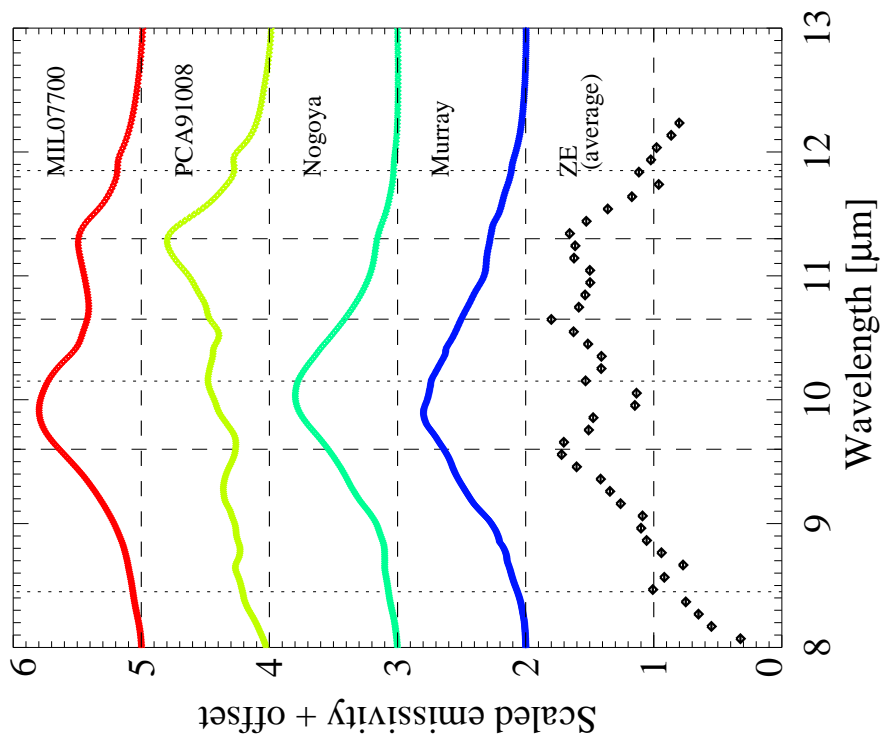


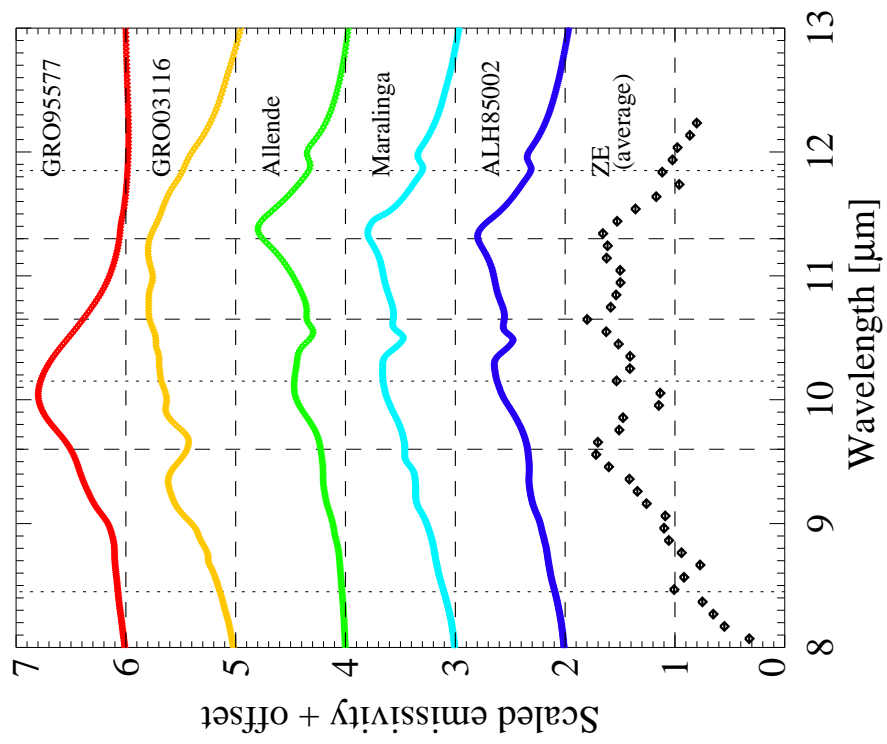


Spectra of collected meteorites

Some of the products in asteroidal collisions strike the Earth as meteorites. They mainly come flying from the asteroid belt near mean-motion resonances with the Jupiter and rarely from the Moon and the Mars (Messenger et al. 2013). In Beck et al. (2014), mid-infrared spectra of carbonaceous chondrite meteorites were measured at Institut de Planétologie et d'Astrophysique de Grenoble. For each meteorite, a pellet was synthesized using 1.0 mg of meteorite dust dispersed in 300 mg of ultrapure KBr. The transmission mid-infrared spectra (2–25 μm) of the pellets were measured. I compare the spectra of the 13 meteorites with that of the zodiacal emission. I got these text data from P.Vernazza in Aix Marseille University and S.Hasegawa in ISAS/JAXA.

As you can see in the following figures, almost all meteorites show the peaks originating from forsterite or amorphous olivine. The situation looks far from the averaged ZE spectra. Since these meteorites are known to have experienced significant aqueous alteration (Beck et al. 2014), such change of the grain properties may affect to the feature shape.

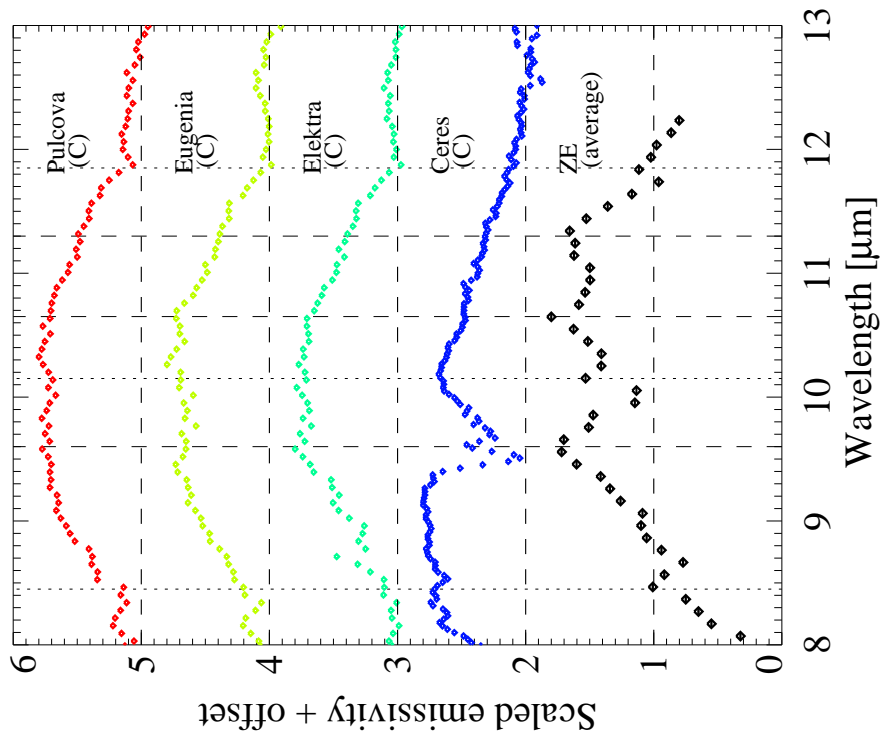
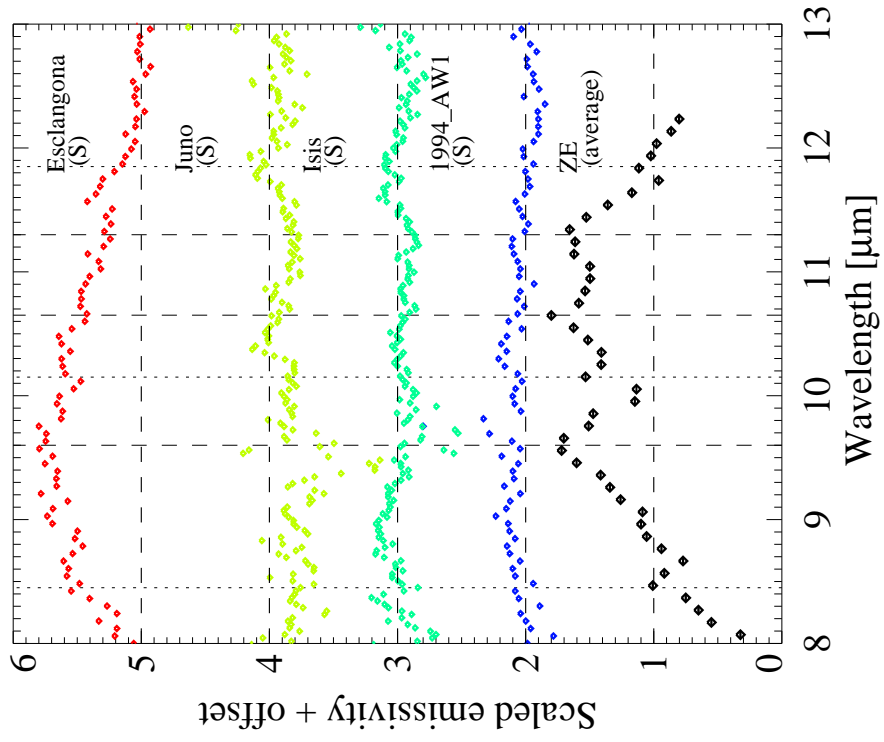


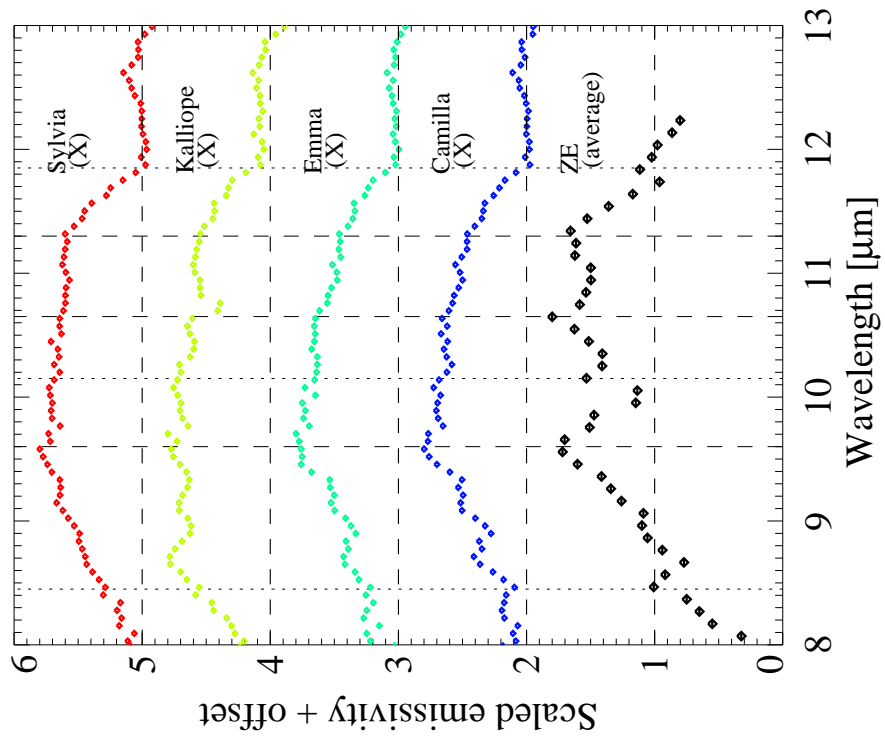
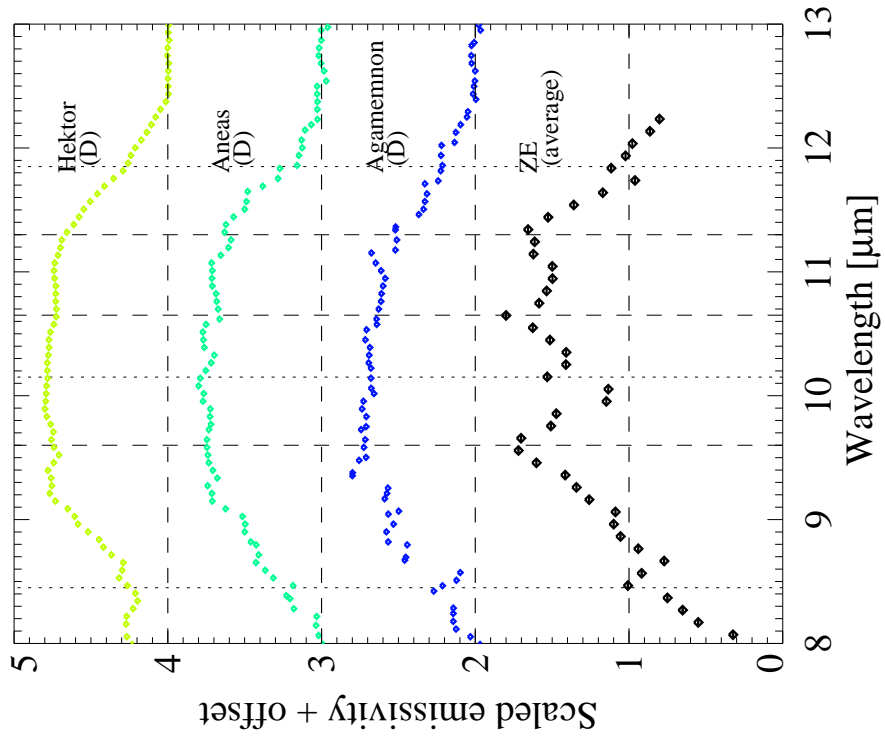


Spectra of asteroids

As described in section 1.1.1, the asteroids is one of the origin of the IPD. Asteroids are categorized to several types depending on the spectral shape in the optical wavelength region. I show the observed/continuum spectra of 4 S-type asteroids, 4 C-type asteroids, 3 D-type asteroids, and 4 X-type asteroids. These data were published in Marchis et al. (2012); Emery et al. (2006); Takahashi et al. (2011). Marchis et al. (2012) collected the mid-IR spectra of asteroids in various spectral types by using the Infrared Spectrograph (IRS) on board the Spitzer Space Telescope (SST). Emery et al. (2006) also used the SST/IRS and focused on the Trojan D-type asteroids. Takahashi et al. (2011) utilized 3.8m United Kingdom Infra-Red Telescope (UKIRT) and the mid-infrared imager/spectrometer Michelle for the ground-based observations of main belt asteroids. In such ground-based observations, the absorption by ozone in the telluric atmosphere contaminate the spectra in the 9.3–10.0 μm range. In all of three references, a continuum was estimated basically by the Standard Thermal Model (Lebofsky & Spencer 1989), and I divided the resultant observed/continuum spectra by the linear baseline fit to the 7.7–8.0 and 12.7–13.0 μm range.

S-type asteroids seem to have no or less excess emission. Other types of asteroids show a smooth convex excess, which is attributed to amorphous silicates. Note that they are the spectra of the asteroids surface and the feature shape strongly depends on the size of materials covering the surface.

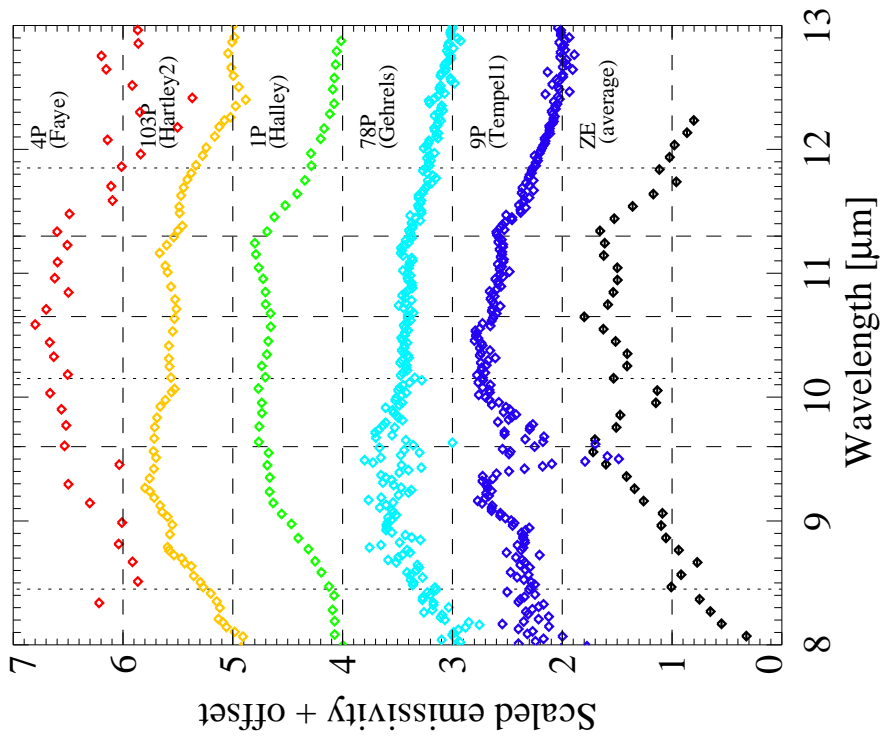
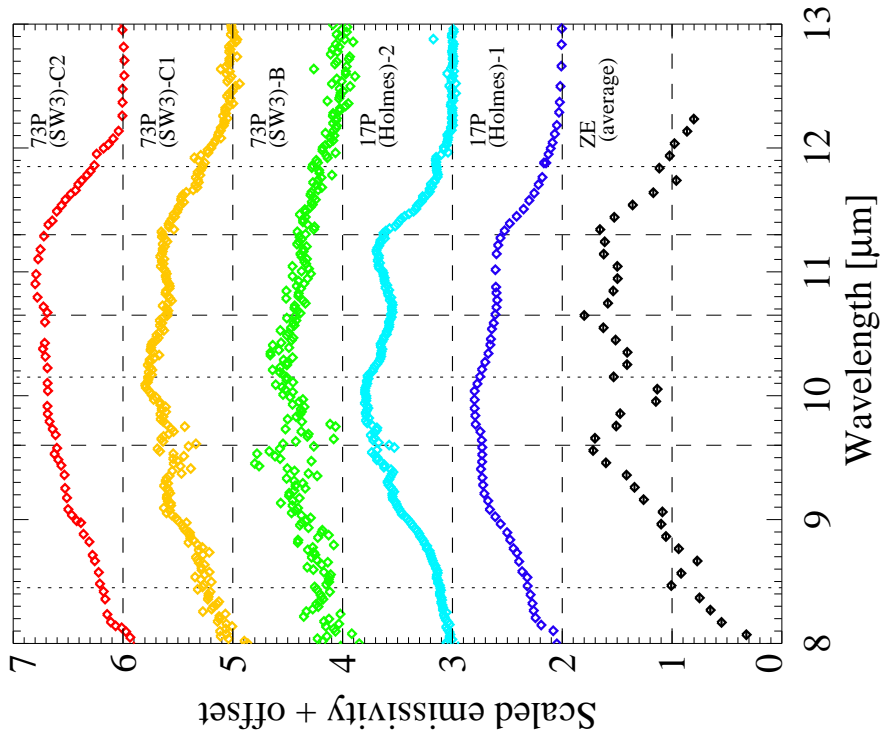


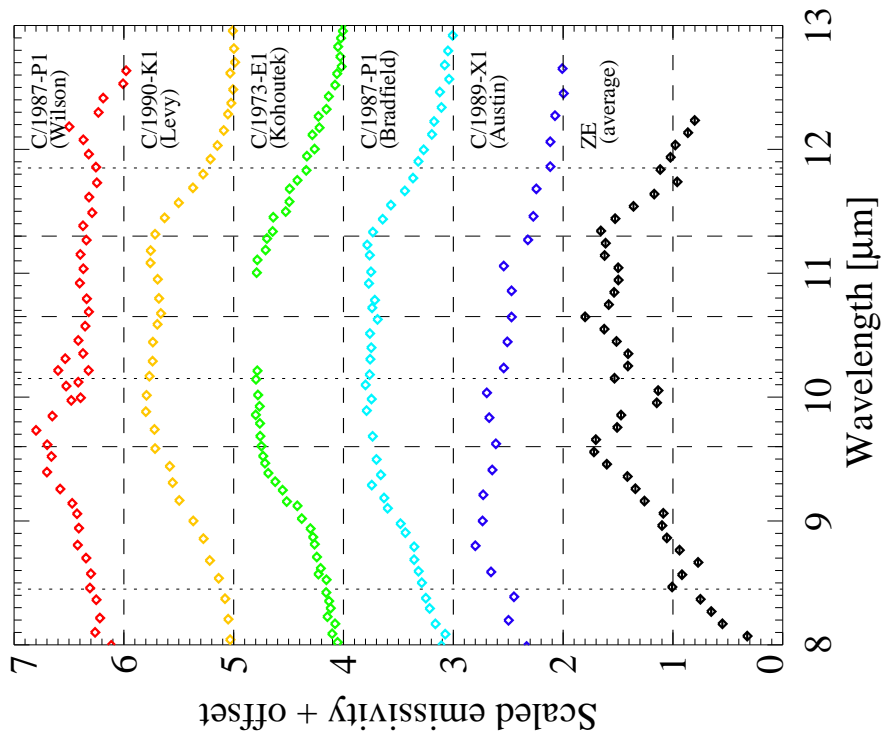
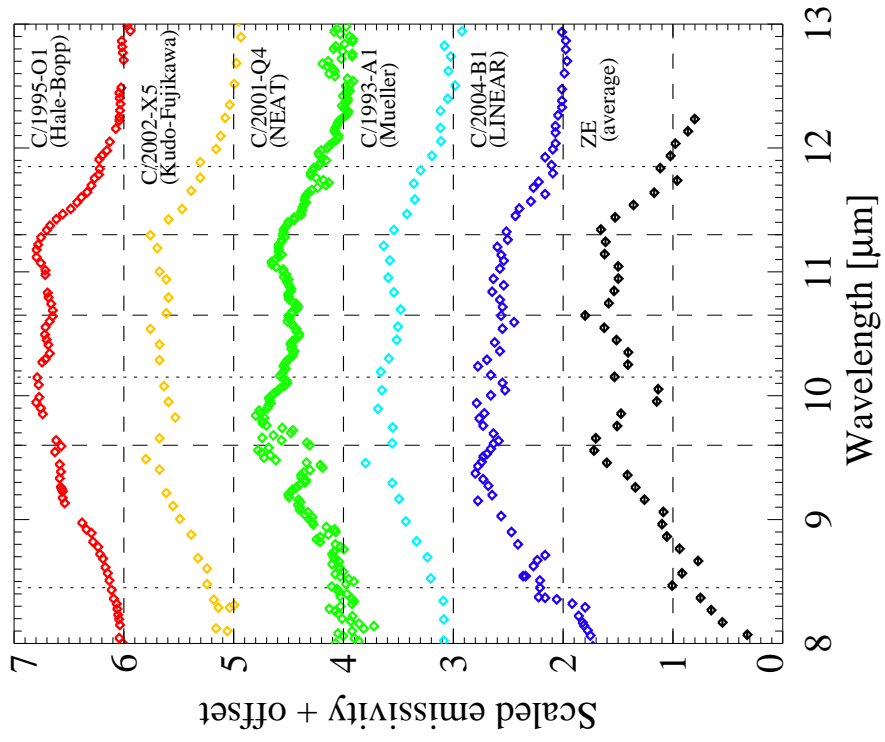


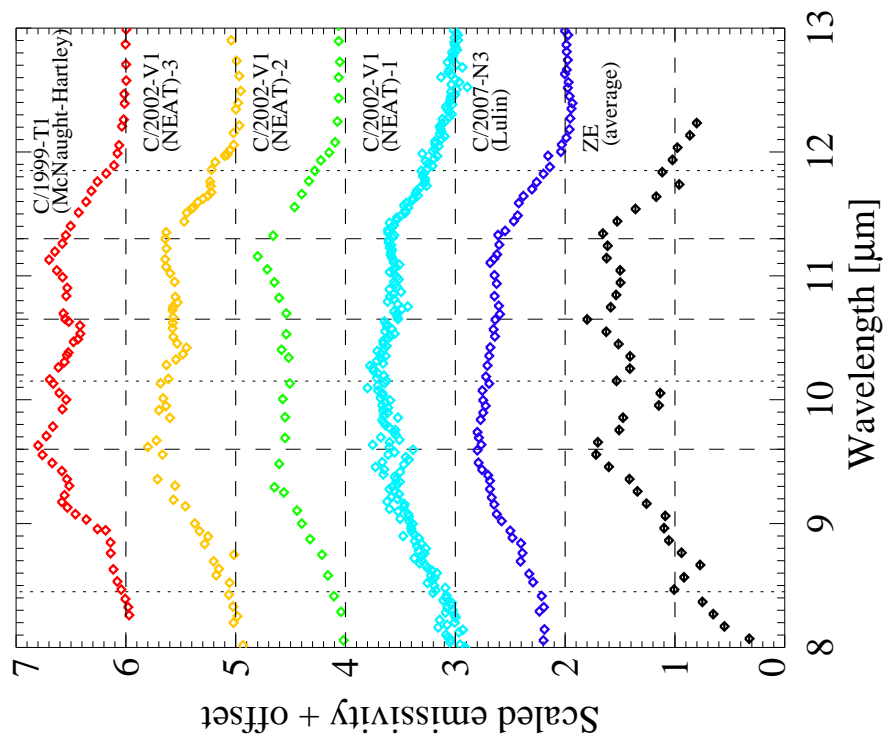
Spectra of cometary dust coma

Comets is thought to be the main origin of the IPD. They are classified roughly into two groups depending on the orbit: the short period comets which are defined by the period shorter than ~ 200 year, and the long period comets which are characterized by the period longer than ~ 200 year. The JFCs and the OCCs are included in the short period comets and the long period comets, respectively. I show the observed/continuum spectra of 10 short period comets (in former two figures) and 15 long period comets (in latter three figures). These data were referred in Vernazza et al. (2015) and I got the text data from P.Vernazza in Aix Marseille University and S.Hasegawa in ISAS/JAXA. I also plotted the data obtained by using 8m Subaru telescope with COMICS (private communications with T.Ootsubo.). In ground-based observations, the absorption by ozone in the telluric atmosphere contaminate the spectra in the 9.3–10.0 μm range.

The shape of the comets spectra has a variety and show some detailed structures. The spectra of the short period comets seem to be relatively peak-less compared with those of the long period comets. The long period comets exhibit several sharp peaks and some of them have the feature shape with three main peaks which is similar to that of the averaged ZE spectra.







Appendix 3

I determined the absolute brightness of the ghost of the small window aperture, which is represented by c in equation (3.3), assuming the non-zero brightness in the regions without the system response originates from the ghost component. In order to identify the origin of this ghost, I investigated the relation between the resultant value of c and the brightness incident into the main field of view or the small window aperture.

Figure 6.1 shows the relation between the resultant value of c and the median value of the brightness at the center of the main field of view, i.e., the integrated brightness of the 0th, the 1st, and the 2nd order light of the zodiacal emission spectrum. If no bright source is seen and the zodiacal emission is the dominant source in the small window aperture, the mid-infrared brightness in the small window aperture is proportional to this median value. In this case, the value of c seems to be proportional to the median brightness in the main field of view as shown by black diamonds in Figure 6.1. On the other hand, the data including the source bright at the mid-infrared (e.g., ultra luminous infrared galaxy; ULIRG) in the small window aperture shows the value of c above the linear relationship seen in the data without bright sources (see red diamonds in Figure 6.1). Even if the source in the small window aperture is bright in the optical or the near-infrared, the value of c follows the linear relationship seen in the data without bright sources, if only the mid-infrared brightness of the source is negligible compared with that of the zodiacal emission like a main-sequence star (see blue diamonds in Figure 6.1).

In addition, I looked into the relation between the excess of the c value above the linear relationship and the mid-infrared brightness of the ULIRG in the small window aperture, regarding the data points with red diamonds. I estimated the mid-infrared brightnesses of the ULIRGs using the spectra database called *NASA/IPAC EXTRAGALACTIC DATABASE*. As shown in Figure 6.2, the excess of the c value was found to have a positive correlation with the mid-infrared brightness of the ULIRG in the small window aperture.

These results are supportive to the positive correlation between the brightness of the ghost

component represented by c and the mid-infrared brightness typical in the small window aperture, but not in the main field of view or others. It indicates that the ghost component I described originates from the small window aperture.

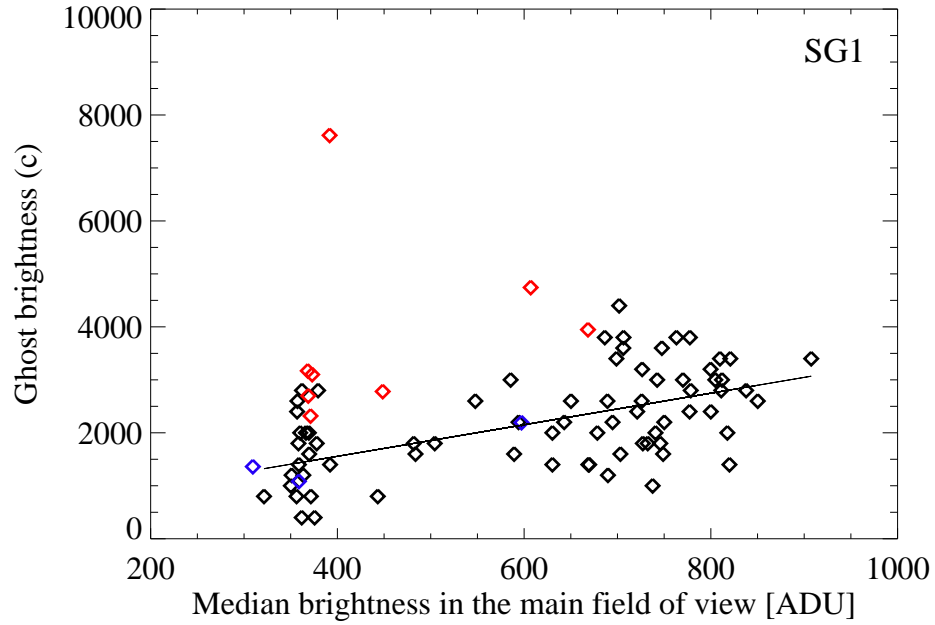


Figure 6.1: Relation between the brightness of the ghost component (c in equation (3.3)) and the median value of the brightness at the center of the main field of view for the SG1. Black diamonds are calculated from the data without any bright source and used for this thesis analysis (listed in Table 2.1). They seem to follow the linear relationship with c shown by a solid line. Blue diamonds shows the results in the data with main-sequence stars in the small window aperture, which is bright in the optical and the near-infrared but not in the mid-infrared. Red diamonds are the results in the data including an ULIRG in the small window aperture.

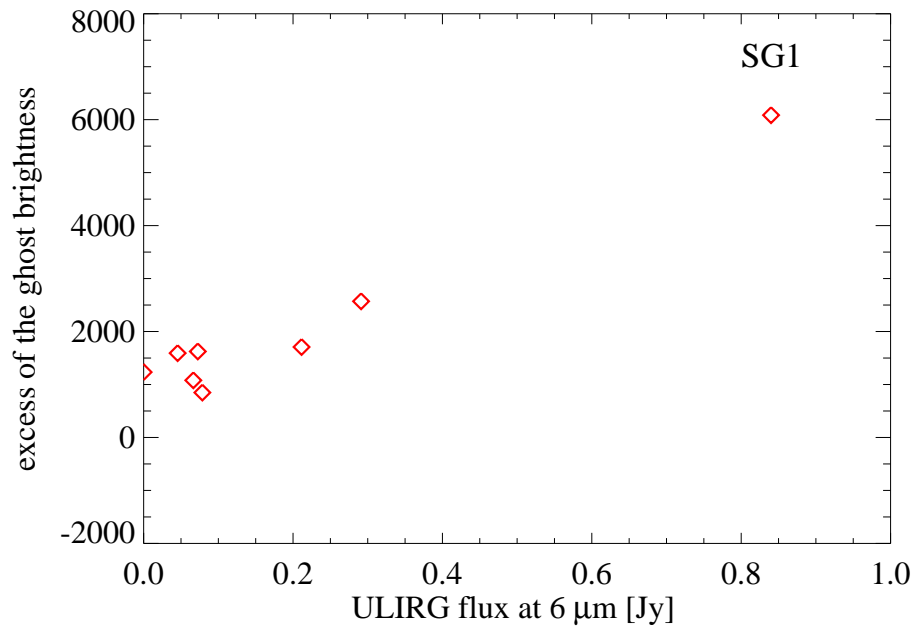


Figure 6.2: Relation between the excess of the c value above the linear relationship and the mid-infrared brightness of the ULIRG in the small window aperture. The mid-infrared brightnesses of the ULIRGs were estimated using the spectra database called *NASA/IPAC EXTRAGALACTIC DATABASE*.

Acknowledgements

First of all, I would like to express my special gratitude to Prof. Hideo Matsuhara for giving me an opportunity to study at ISAS/JAXA and his continuous supports through a lot of discussions. Thanks to his encouragement, I got a chance to challenge the research in various related field. I also acknowledge Dr. Takafumi Ootsubo for many valuable discussions and suggestions on this thesis. His plenty of knowledge on the infrared astronomy, particularly related to the Solar System, and encouraging comments were always helpful for me. I would like to thank the co-authors of my refereed paper. Prof. Itsuki Sakon kindly taught me the previous investigations into the instrumental artifacts. I also appreciate Prof. Fumihiko Usui for his valuable suggestions about not only the implication of my results but also how to write papers on observational astronomy. I learned a lot of mineralogical thinking from Prof. Hiroki Chihara, which were necessary for this thesis.

I acknowledge all the referees of my thesis defense: Prof. Takahiro Iwata, Prof. Yuko Inatomi, and Prof. Hirokazu Kataza, in addition to Prof. Hiroki Chihara and Prof. Hideo Matsuhara again. Their crucial advises and comments will be nourishment in my future research.

I am also grateful to Prof. Shuji Matsuura and the team members of CIBER-2 (The Cosmic Infrared Background Experiment 2). The work for the instrumental development and frequent discussions with the team members were precious experience for me and will be connected to this thesis work.

I do appreciate all the members of the AKARI project because this thesis work is based on the AKARI data, which is unique and essential for the study on the zodiacal emission. I also would like to acknowledge all the members of LIRA (Laboratory of Infrared Astrophysics) group. Thanks to their heart-warming encouragement and daily conversation in lunch time or coffee breaks, I could finish my thesis work.

Finally, I wish to thank my parents for their thoughtful supports and continuous encouragement for this 28 years. In addition, I could be relaxed thanks to my lovely two beagles, Cor and Caroli (the names originating from the binary star, α Canum Venaticorum).

Bibliography

- Allamandola, L. J., Tielens, A. G. G. M., & Barker, J. R. 1985, *ApJ*, 290, L25
- Barker, A. S. 1973, *Physical Review B*, 7, 2507
- Beck, P., Garenne, A., Quirico, E., et al. 2014, *Icarus*, 229, 263
- Bell, K. R., Cassen, P. M., Klahr, H. H., & Henning, T. 1997, *ApJ*, 486, 372
- Bernard-Salas, J., Pottasch, S. R., Wesselius, P. R., & Feibelman, W. A. 2003, *A&A*, 406, 165
- Bischoff, A. 1998, *Meteoritics and Planetary Science*, 33, 1113
- Bohren, C. F., & Huffman, D. R. 1983, *Absorption and scattering of light by small particles*
- Bohren, C. F., & Wickramasinghe, N. C. 1977, *Ap&SS*, 50, 461
- Borghesi, A., Bussoletti, E., & Colangeli, L. 1987, *ApJ*, 314, 422
- Bradley, J. P. 2003, *Treatise on Geochemistry*, 1, 711
- Bradley, J. P., Brownlee, D. E., & Veblen, D. R. 1983, *Nature*, 301, 473
- Bradley, J. P., Keller, L. P., Snow, T. P., et al. 1999, *Science*, 285, 1716
- Burns, J. A., Lamy, P. L., & Soter, S. 1979, *Icarus*, 40, 1
- Chihara, H., Koike, C., Tsuchiyama, A., Tachibana, S., & Sakamoto, D. 2002, *A&A*, 391, 267
- Choudhury, N., & Chaplot, S. L. 2000, *Solid State Communications*, 114, 127
- Ciesla, F. J. 2009, *Meteoritics and Planetary Science*, 44, 1663
- Cohen, M., Walker, R. G., Carter, B., et al. 1999, *AJ*, 117, 1864
- Cohen, M., Wheaton, W. A., & Megeath, S. T. 2003, *AJ*, 126, 1090

- Cohen, M., Witteborn, F. C., Carbon, D. F., et al. 1996, *AJ*, 112, 2274
- Cohen, M., Witteborn, F. C., Walker, R. G., Bregman, J. D., & Wooden, D. H. 1995, *AJ*, 110, 275
- Davies, J. K., Green, S. F., Stewart, B. C., Meadows, A. J., & Aumann, H. H. 1984, *Nature*, 309, 315
- Demichelis, R., Suto, H., Noël, Y., et al. 2012, *MNRAS*, 420, 147
- Divine, N. 1993, *Journal of Geophysical Research*, 98, 17029
- Dones, L., Brassier, R., Kaib, N., & Rickman, H. 2015, *Space Sci. Rev.*, 197, 191
- Dones, L., Weissman, P. R., Levison, H. F., & Duncan, M. J. 2004, in *Astronomical Society of the Pacific Conference Series*, Vol. 323, *Star Formation in the Interstellar Medium: In Honor of David Hollenbach*, ed. D. Johnstone, F. C. Adams, D. N. C. Lin, D. A. Neufeld, & E. C. Ostriker, 371
- Dorschner, J., Begemann, B., Henning, T., Jaeger, C., & Mutschke, H. 1995, *A&A*, 300, 503
- Duncan, M. J., & Levison, H. F. 1997, *Science*, 276, 1670
- Emery, J. P., Cruikshank, D. P., & Van Cleve, J. 2006, *Icarus*, 182, 496
- Gail, H. P. 2001, *A&A*, 378, 192
- Gail, H. P. 2004, *A&A*, 413, 571
- Ganguly, J., & Bose, K. 1995, in *Lunar and Planetary Inst. Technical Report*, Vol. 26, *Lunar and Planetary Science Conference*
- Gasparik, T. 1990, *Journal of Geophysical Research*, 95, 15,751
- Genzel, L., & Martin, T. P. 1973, *Surface Science*, 34, 33
- Germani, M. S., Bradley, J. P., & Brownlee, D. E. 1990, *Earth and Planetary Science Letters*, 101, 162
- Gomes, R., Levison, H. F., Tsiganis, K., & Morbidelli, A. 2005, *Nature*, 435, 466
- Grün, E., Zook, H. A., Fechtig, H., & Giese, R. H. 1985, *Icarus*, 62, 244
- Gustafson, B. A. S. 1994, *Annual Review of Earth and Planetary Sciences*, 22, 553
- Hallenbeck, S. L., Nuth, Joseph A., I., & Nelson, R. N. 2000, *ApJ*, 535, 247

- Hanner, M. S. 1983, in *Cometary Exploration*, Volume 2, Vol. 2, 1–22
- Harker, D. E., & Desch, S. J. 2002, *ApJ*, 565, L109
- Harker, D. E., Woodward, C. E., Wooden, D. H., Fisher, R. S., & Trujillo, C. A. 2007, *Icarus*, 190, 432
- Hauser, M. G., Gillett, F. C., Low, F. J., et al. 1984, *ApJ*, 278, L15
- Ishiguro, M., Watanabe, J., Usui, F., et al. 2002, *ApJ*, 572, L117
- Jackson, A. A., & Zook, H. A. 1989, *Nature*, 337, 629
- Jehn, R. 2000, *Planetary and Space Science*, 48, 1429
- Kawada, M., Baba, H., Barthel, P. D., et al. 2007, *Publications of the Astronomical Society of Japan*, 59, S389
- Keller, L. P., & Messenger, S. 2005, in *Astronomical Society of the Pacific Conference Series*, Vol. 341, *Chondrites and the Protoplanetary Disk*, ed. A. N. Krot, E. R. D. Scott, & B. Reipurth, 657
- Kelsall, T., Weiland, J. L., Franz, B. A., et al. 1998, *ApJ*, 508, 44
- Kemper, F., Vriend, W. J., & Tielens, A. G. G. M. 2005, *ApJ*, 633, 534
- Kerker, M. 1969, *The scattering of light and other electromagnetic radiation*.
- Kimura, H. 2013, *ApJ*, 775, L18
- Klacka, J. 1992, *Earth Moon and Planets*, 59, 211
- Koike, C., Chihara, H., Tsuchiyama, A., et al. 2003, *A&A*, 399, 1101
- Kondo, T., Ishihara, D., Kaneda, H., et al. 2016, *AJ*, 151, 71
- Lebofsky, L. A., & Spencer, J. R. 1989, in *Asteroids II*, ed. R. P. Binzel, T. Gehrels, & M. S. Matthews, 128–147
- Leger, A., & Puget, J. L. 1984, *A&A*, 500, 279
- Leinert, C., Ábrahám, P., Acosta-Pulido, J., Lemke, D., & Siebenmorgen, R. 2002, *A&A*, 393, 1073
- Levison, H. F., & Morbidelli, A. 2003, *Nature*, 426, 419
- Liou, J. C., Dermott, S. F., & Xu, Y. L. 1995, *Planetary and Space Science*, 43, 717

- Lodders, K. 2003, *ApJ*, 591, 1220
- Love, S. G., & Brownlee, D. E. 1993, *Science*, 262, 550
- Low, F. J., Beintema, D. A., Gautier, T. N., et al. 1984, *ApJ*, 278, L19
- Marchis, F., Enriquez, J. E., Emery, J. P., et al. 2012, *Icarus*, 221, 1130
- Marzari, F., & Vanzani, V. 1994, *A&A*, 283, 275
- McSween, H. Y. 1979, *Reviews of Geophysics and Space Physics*, 17, 1059
- . 1987, *Geochimica et Cosmochimica Acta*, 51, 2469
- Merouane, S., Djouadi, Z., & Le Sergeant d'Hendecourt, L. 2014, *ApJ*, 780, 174
- Messenger, S., Keller, L. P., & Nguyen, A. N. 2013, in *Proceedings of The Life Cycle of Dust in the Universe: Observations*, 40
- Morrison, D. A., & Clanton, U. S. 1979, *Lunar and Planetary Science Conference Proceedings*, 2, 1649
- Mosteller, F., & Tukey, J. W. 1977, *Data analysis and regression. A second course in statistics*
- Mukai, T., & Giese, R. H. 1984, *A&A*, 131, 355
- Mukai, T., Ishimoto, H., Kozasa, T., Blum, J., & Greenberg, J. M. 1992, *A&A*, 262, 315
- Murakami, H., Baba, H., Barthel, P., et al. 2007, *Publications of the Astronomical Society of Japan*, 59, S369
- Murata, K., Chihara, H., Koike, C., et al. 2009, *ApJ*, 697, 836
- Naumann, A. W. 1966, *Clays and Clay Minerals*, 14, 367
- Nesvorný, D., Bottke, W. F., Levison, H. F., & Dones, L. 2003, *ApJ*, 591, 486
- Nesvorný, D., Jenniskens, P., Levison, H. F., et al. 2010, *ApJ*, 713, 816
- Noguchi, T., Nakamura, T., Kimura, M., et al. 2011, *Science*, 333, 1121
- Ohyama, Y., Onaka, T., Matsuhara, H., et al. 2007, *Publications of the Astronomical Society of Japan*, 59, S411
- Onaka, T., Matsuhara, H., Wada, T., et al. 2007, *Publications of the Astronomical Society of Japan*, 59, S401

- Ootsubo, T., Onaka, T., Yamamura, I., et al. 1998, *Earth, Planets, and Space*, 50, 507
- Ootsubo, T., Doi, Y., Takita, S., et al. 2016, *Publications of the Astronomical Society of Japan*, 68, 35
- Poppe, A. R. 2016, *Icarus*, 264, 369
- Reach, W. T., Morris, P., Boulanger, F., & Okumura, K. 2003, *Icarus*, 164, 384
- Reach, W. T., Abergel, A., Boulanger, F., et al. 1996, *A&A*, 315, L381
- Renard, J. B., Levasseur-Regourd, A. C., & Dumont, R. 1995, *A&A*, 304, 602
- Sakata, A., Wada, S., Onaka, T., & Tokunaga, A. T. 1987, *ApJ*, 320, L63
- Sakata, A., Wada, S., Tanabe, T., & Onaka, T. 1984, *ApJ*, 287, L51
- Sakon, I., Onaka, T., Wada, T., et al. 2007, *Publications of the Astronomical Society of Japan*, 59, S483
- Schramm, L. S., Brownlee, D. E., & Wheelock, M. M. 1989, *Meteoritics*, 24, 99
- Shinnaka, Y., Ootsubo, T., Kawakita, H., et al. 2018, *AJ*, 156, 242
- Shu, F. H., Shang, H., & Lee, T. 1996, *Science*, 271, 1545
- Sogawa, H., Koike, C., Chihara, H., et al. 2006, *A&A*, 451, 357
- Strazzulla, G., Dotto, E., Binzel, R., et al. 2005, *Icarus*, 174, 31
- Sykes, M. V., & Greenberg, R. 1986, *Icarus*, 65, 51
- Takahashi, J., Itoh, Y., & Takahashi, S. 2011, *Publications of the Astronomical Society of Japan*, 63, 499
- Takigawa, A., & Tachibana, S. 2012, *ApJ*, 750, 149
- Tanaka, K. K., Yamamoto, T., & Kimura, H. 2010, *ApJ*, 717, 586
- Thommes, E. W., Duncan, M. J., & Levison, H. F. 1999, *Nature*, 402, 635
- Tomeoka, K., McSween, Harry Y., J., & Buseck, P. R. 1989, *Antarctic Meteorite Research*, 2, 221
- Tsiganis, K., Gomes, R., Morbidelli, A., & Levison, H. F. 2005, *Nature*, 435, 459
- Tukey, J. W. 1977, *Exploratory data analysis*

- Usui, F., Hasegawa, S., Ootsubo, T., & Onaka, T. 2018, *Publications of the Astronomical Society of Japan*, 146
- Vernazza, P., Binzel, R. P., Rossi, A., Fulchignoni, M., & Birlan, M. 2009, *Nature*, 458, 993
- Vernazza, P., Marsset, M., Beck, P., et al. 2015, *ApJ*, 806, 204
- Vinković, D. 2009, *Nature*, 459, 227
- Willner, S. P. 1984, in *Astrophysics and Space Science Library*, Vol. 108, *Galactic and Extragalactic Infrared Spectroscopy*, ed. M. F. Kessler & J. P. Phillips, 37–57
- Wyatt, M. C., Dermott, S. F., Telesco, C. M., et al. 1999, *ApJ*, 527, 918